Automatic Defect Detection and Depth Estimation using Pulsed Thermography

Mémoire

Peyman Hedayati Vahid

Maîtrise en Génie Électrique
Maître ès sciences (M.Sc.)

Québec, Canada

© Peyman Hedayati Vahid, 2014

Résumé

L'évaluation non-destructive (END) est une branche de la science qui s'intéresse à l'uniformité, la qualité et la conformité des matériaux et les composants qu'ils servent à construire. Les techniques de END visent à repérer et à mesurer les caractéristiques principales des matériaux sans en affecter ou à en détruire la structure ou la fonctionnalité. L'END permet d'observer les propriétés internes des pièces et de détecter les défauts sous leur surface. Cette approche est devenue graduellement une technologie importante pour garantir la sécurité et la fiabilité de plusieurs composantes de système en design, en fabrication et en développement de produits.

La thermographie infrarouge est une approche d'END sans contact rapide qui utilise des caméras thermiques. Elle permet de détecter l'énergie thermique émise par les objets et à en afficher la distribution en température de la surface du spécimen sous observation.

Dans ce projet, notre objectif est d'exploiter la thermographie infrarouge pour détecter les défauts sous la surface des objets. Plus spécialement, nous nous intéressons à la localisation des défauts et à l'estimation de leur profondeur sous la surface. Le manuscrit présente une investigation de différentes méthodes de localisation de défauts et de mesure de leur profondeur des défauts sous la surface pour différentes catégories de matériaux.

Abstract

Non-Destructive Testing (NDT) is an aspect of science concerning on uniformity, quality and serviceability of materials and their components. NDT techniques attempt to inspect and measure significant features of materials without changing or destroying their structure or functionality. NDT makes it possible to observe the internal properties of parts and detect the undersurface defects. NDT has progressively become an important technology to assure safety and reliability of many system components in the design, manufacturing and development areas.

Infrared thermography is essentially a fast non-contact NDT inspection method that uses thermographic cameras. This technique detects the infrared energy emitted from objects and displays the corresponding temperature distributions on the specimen.

In this project, we aim to use infrared thermography for detecting subsurface defects. Localizing the defects and estimating their depths are the important problems to be addressed in our research project. The manuscript investigates different methods related to these challenges.

Table of contents

Résumé iii

Abstract v

Table of contents vii

List of tables ix

List of figures xi

Acknowledgments xv

Introduction 1

1 Introduction of infrared 3
1.1 Infrared systems fundamentals . . . 6
1.1.1 Thermal emission . . . 6
1.1.2 Choice of infrared band . . . 7
1.1.3 Detectors . . . 8
1.2 Thermal imaging system concepts . . . 8
1.3 Measuring systems . . . 9
1.3.1 Non-contact thermometers . . . 9
1.3.2 Radiometers . . . 10

2 Literature review of defect detection and depth estimation approaches 13
2.1 Related works on defect detection . . . 13
2.1.1 Nondedicated algorithms . . . 13
Otsu's method . . . 13
Valley-emphasis method . . . 15
Neighborhood valley-emphasis method . . . 17
Active contour method . . . 17
2.1.2 Dedicated algorithms . . . 19
Hamadani method . . . 19
Heriansyah method . . . 19
2.2 Related work on depth estimation . . . 22
Peak Temperature Contrast Method . . . 23
Peak Temperature Contrast Slope Method . . . 25
Pulsed Phase Thermography Method . . . 27

Logarithmic Peak Second Derivative Method . . . 29
Least Squares Fitting Method . . . 29

3 Description of the implemented approach for defect detection and depth estimation 31
3.1 Image processing and data analysis . . . 31
3.1.1 Fixed Pattern Noise (FPN) . . . 31
3.1.2 Bad pixels . . . 32
3.1.3 Temperature Calibration . . . 32
3.1.4 Vignetting . . . 32
3.1.5 Noise Filtering . . . 33
3.1.6 Thermographic signal reconstruction . . . 33
3.1.7 Principal component thermography . . . 35
3.1.8 Pulse Phase Thermography . . . 38
3.2 Defect detection . . . 39
3.3 Depth estimation . . . 40

4 Experimental results and discussion 45
4.1 Pulsed thermography setup . . . 45
4.2 Data analysis . . . 46
4.2.1 Thermographic signal reconstruction . . . 49
4.2.2 Principal component thermography . . . 49
4.2.3 Pulse phase thermography . . . 49
4.2.4 Combination of TSR with PPT and PCT techniques . . . 52
4.3 Defect detection . . . 53
4.4 Depth estimation . . . 56
4.4.1 Pulsed phase thermography-based depth estimation . . . 58
Steel . . . 58
Aluminum . . . 59
4.4.2 Absolute peak slope time method results . . . 61
Steel . . . 62
Aluminum . . . 63

Conclusion 67

A Appendix A : Plate Specifications 69
A.1 ACIER002 . . . 69
A.2 ACIER1983 . . . 70
A.3 ALU016 . . . 70
A.4 ALU1983 . . . 71
A.5 ALU208 . . . 71
A.6 PLEXI006 . . . 72

B Appendix B : Phoenix camera quick start manual 73

Bibliography 81

List of tables

1.1 Division of infrared radiation [5]. 6
1.2 Power available in each MWIR and LWIR imaging bands [2]. 8

4.1 Defects depth and blind frequencies of defects for ACIER002. 59
4.2 Defects depth and blind frequencies of defects for ALU208 specimen. 60

List of figures

1.1 History of infrared detectors and systems. Three generation systems can be considered for main military and civilian applications : 1^{st} Generation, Scanning systems ; 2^{nd} Generation, Starting systems-electronically scanned ; and 3^{rd} Generation, Multicolor functionality and other on-chip functions [29]. 4
1.2 Applications of infrared detectors [31]. 5
1.3 Uncooled thermal camera business (units) [29]. 5
1.4 Electromagnetic spectrum [31]. 6
1.5 Planck's law for spectral emittance [2]. 7
1.6 Classifications of non-contact thermometers [5]. 10
1.7 Classifications of infrared radiometers [5]. 11

2.1 Optimal threshold selection in gray-level histogram : (a) bimodal ; (b) unimodal [23]. 15
2.2 Problem with Otsu's method in thresholding small defects : (a) original image ; (b) Valley-emphasis threshold result ; (c) Otsu's threshold result ; (d) histogram and threshold values [23]. 16
2.3 Valley-emphasis and Otsu threshold results for a part image : (a) part image ; (b) valley-emphasis tri-level threshold result ; (c) Otsu tri-level threshold result ; (d) histogram and threshold values [23]. 16
2.4 Segmentation results of a standard image : (a) original image, (b) histogram and threshold values, (c) Otsu segmentation result with threshold 106, (d) valley-emphasis segmentation result with threshold 113, (e) neighborhood valley-emphasis segmentation result with threshold 52 [7]. 18
2.5 Detection of different objects from a noisy image, with various shapes and with an interior contour [4]. 19
2.6 (a) Thermal image and (b) its histogram, thresholded using Hamadani's method with (c) $k_1 = 1$, $k_2 = 1$, $T = 189$, (d) $k_1 = 1$, $k_2 = 2$, $T = 200$, (e) $k_1 = 1$, $k_2 = 1.5$, $T = 194$, and (f) $k_1 = 1$, $k_2 = 7$, $T = 253$[12]. 20
2.7 IBO and IDO operations and their combinations (which is simply their summation) [12]. 21
2.8 Minimum frequency thresholding principle [12]. 22
2.9 Sketch map of the pulsed thermographic principle. 23
2.10 Surface temperature decay curves in defect area (T) and sound area (T_r) [34]. . 24
2.11 Temperature contrast ΔV as a function of ω_r [34]. 25
2.12 Slope of temperature contrast $\frac{d(\Delta V)}{d\omega_r}$ as a function of ω_r [34]. 26
2.13 Dimensionless peak-slope time ω_s and peak slope $\frac{d(\Delta V_s)}{d\omega_r}$ as functions of thickness ratio y [34]. 27

2.14 (a) Thermogram sequence and temperature profile for a pixel, and (b) phasegram sequence after application of the FFT [17]. 28
2.15 Blind frequency relationship with defect depth [17]. 28
2.16 Temperature curve and its first and second derivatives as functions of time on a logarithmic scale [33]. 30

3.1 Bad pixels in a thermal image. 32
3.2 The temperature calibration curve using blackbody. 33
3.3 Aluminum specimen ; (a) raw thermogram after heat pulse (top) and temperature curve for a defect (bottom) ; (b) the thermogram using both Gaussian and median filtering (top) and temperature curve for the same defect (bottom). . . 34
3.4 Logarithmic temperature-time plot of a steel specimen. 35
3.5 Comparison of a thermal sequence's components [27]. 36
3.6 Response at peak contrast [27]. 37
3.7 Comparison of the distribution of peak contrast with the first four EOF's [27]. . 37
3.8 (a) Amplitude A ; (b) phase ϕ of the transform (top) and their frequency spectra (bottom) for a non-defective pixel (i, j) [3]. 38
3.9 (a) The temperature curve, (b) The f curve of aluminum sample [36]. 42
3.10 The experimental and simulated f' curves of aluminum sample [36]. 42

4.1 The experimental setup ; (1) Sample of tested material, (2) the energy source (two flash lamps), (3) the infrared camera and, (4) the control system. 46
4.2 Thermograms sequence after saturated time (sound area and defect area) for specimen ALU016 with 1 mm defect depth. 47
4.3 Comparative results of image denoising methods for aluminum (ALU016), plexiglas (PLEXI006) and steel (ACIER002) specimens. Hamadani's method is used to segment the thermograms. 48
4.4 Curve temperature profile of defect and sound areas for (a) PLEXI006, (b) ACIER002, (c)-(d) TSR with 3-degree polynomial, (e)-(f) TSR with 5-degree polynomial. 50
4.5 The thermograms corresponding to the first four EOF of PCT for ALU016 and ACIER002. 51
4.6 The first three frequencies of the phase thermograms on the specimen ALU1983 : (a) frequency = 0.27 Hz, (b) frequency = 0.55 Hz, (c) frequency = 0.83 Hz. . . 52
4.7 Detecting different size of defects. 52
4.8 Detection results of Otsu [24], Valley-emphasis [23], and Neighborhood valley-emphasis [7] for ACIER002 specimen. 53
4.9 Detection results of Hamadani [10], Active contour [4], and Heriansyah [12] for ACIER002 specimen. 54
4.10 Performance comparison of defect detection methods for ACIER002 specimen. . 55
4.11 Histogram of thermal image of figure 4.10. 55
4.12 Results obtained by the proposed approach in comparison with the ones obtained by [7; 10]. 57
4.13 Detecting different size of defects. 58
4.14 Phase profile for ACIER002 with sampling rate 70 Hz and total number of 500 images in 7.14 seconds. 59
4.15 Phase contrast profile for ACIER002 with sampling rate 70 Hz and total number of 500 images in 7.14 seconds. 60

4.16 Phasegrams for the blind frequencies corresponding to the 4 different depths of the defects. . . . 60
4.17 Depth vs frequency linear fit for steel plate with sampling rate 70 Hz. . . . 61
4.18 Phase profile for ALU208 with sampling rate 58 Hz and total number of 600 images in 10.29 seconds. . . . 61
4.19 Phase contrast profile for ALU208 with sampling rate 58 Hz and total number of 600 images in 10.29 seconds. . . . 62
4.20 ALU208 with sampling rate 58 Hz (a) Defects' depths and location, and (b) Depth vs frequency linear fit. . . . 62
4.21 Temperature curves of steel plate (ACIER002) with sampling rate 45 Hz and total number of 500 images in 11.11 seconds. . . . 63
4.22 The f curves of steel plate. . . . 63
4.23 The f' curves of steel plate. . . . 64
4.24 Absolute peak slope time versus square depth of ACIER002. . . . 64
4.25 The f curves of aluminum plate. . . . 64
4.26 The f' curves of aluminum plate. . . . 65
4.27 The absolute peak slope time against square of the depth of the specimen ALU208. 65

B.1 Editor rtools.reg . . . 74
B.2 Phoenix main window . . . 74
B.3 RDac main window . . . 75
B.4 RDac NUC window . . . 76
B.5 Rdac Properties window . . . 77
B.6 RDac Acquisition options window . . . 78

Acknowledgments

I would like to express my deepest appreciation to my supervisor, Dr. Denis Laurendeau and my co-supervisor, Dr. Abdel Hakim Bendada which provide me a special opportunity to work with them. I really appreciate all the time, help and effort, which they have invested in me and my project. Especially, I would like to acknowledge their guidance and support throughout these past few years both in academic and non-academic situations.

With all my sincere feelings, I would like to extend my gratefulness to my wife, Zahra, who never stopped believing in me. I dedicate this thesis to her. Many thanks to Clemente Ibarra-Castanedo and Denis Ouellet for their valuable academic advice. Special thanks goes to my friend, Somayeh Hesabi, for her explicit help and support.

I gratefully acknowledge NSERC-Creaform Industrial Research Chair for their support of my research study ; this work would not be feasible without their supports.

Introduction

There is growing interest in fields such as condition monitoring, fault diagnosis, and Non-Destructive Testing (NDT). NDT is a term used to describe the tasks of the examination of materials and components without changing or destroying their structure. It can provide an effective means to detect surface and subsurface defects and also to estimate their size and depth.

NDT is essential to assure safety and reliability of many systems. Typical examples are aircrafts, spacecrafts (shuttle), motor vehicles, pipelines, bridges, trains, power stations, refineries, buildings and oil platforms. NDT is important not only to guarantee the safe operation of system components, but also to assess the remaining life or the need for a replacement.

Using Infrared Thermography (IRT) in NDT allows to observe the temperature differences on thermograms measured by infrared cameras and to detect the subsurface features. The overall goal of the research project we are participating in, is to build the 3D model of structures and map the subsurface defects on this model. Our task in this project is to perform NDT for detecting subsurface defects and estimating their size and depth. Other team members use this infrared information to map it on the 3D model built with geometric data captured by 3D sensors.

In our project, we face two important problems : localizing the defects and estimating their depths using pulsed thermography. In the following we will investigate different methods for addressing these challenges. Chapter 1, presents an introduction on infrared. A literature review on defect detection and depth estimation methods is provided in chapter 2. Chapter 3 presents our proposed approach for defect detection and depth estimation. The experimental results are provided in chapter 4 and finally a conclusion is presented.

Chapter 1

Introduction of infrared

Nondestructive testing (NDT) is used to evaluate a material or system properties without changing or destroying their structure or functionality. While, other technologies such as radio astronomy, voltage and amperage measurement and flow measurement are nondestructive, they are not used to examine or inspect materials. Since 1920s, the art of NDT has developed from a laboratory activity to an essential tool of production. Nowadays, nondestructive tests are widely used to detect variations in structures, the presence of cracks or discontinuities, to measure the thickness of materials and to determine other characteristics of products [22].

The application of nondestructive testing are ensuring product reliability and accuracy, controlling manufacturing process, decreasing the manufacturing costs, maintaining a uniform quality level, avoiding system failures and saving human life. The National Materials Advisory Board (NMAB) Ad Hoc Committee on Nondestructive Evaluation classified NDT technology into six categories : mechanical-optical, penetrating radiation, electromagnetic-electronic, sonic-ultrasonic, chemical-analytical and thermal and infrared. Infrared thermography is a NDT inspection method that uses thermographic cameras. Temperature and thermal behavior of materials are the essential factors in maintenance operations and manufacturing processes [22].

This section briefly addresses the definition of infrared testing and presents a history of infrared, fundamentals of infrared testing and, thermal imaging concepts. More than 200 years ago, Frederick William Herschel was the first person to discover infrared radiation. He accidentally discovered Uranus by infrared rays. At the beginning he used a prism to protect his eyes against the sun. By passing sunlight through a prism and using a thermometer he found that the red band had the maximum elevation of temperature while all radiations were invisible. In addition temperatures elevation depends on wavelength [29]. As Maldague [19] discussed, this is explained by Planck's and Stefan's laws.

Figure 1.1 describes a history of the development of the IR detector technology after World War II ; it gives the approximate dates for the specified materials. During this World War, modern IR techniques were used. Most of the IR technology has been used in the military,

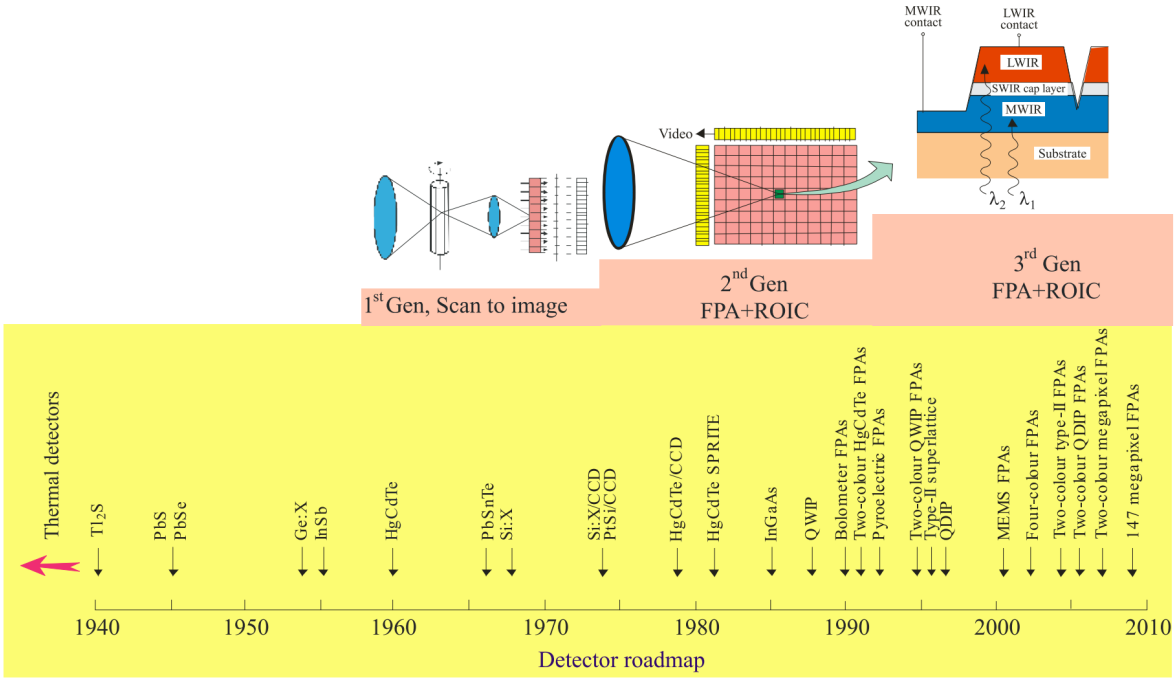

FIGURE 1.1 – History of infrared detectors and systems. Three generation systems can be considered for main military and civilian applications : 1^{st} Generation, Scanning systems ; 2^{nd} Generation, Starting systems-electronically scanned ; and 3^{rd} Generation, Multicolor functionality and other on-chip functions [29].

but peaceful applications have been exploited since the last decade of twentieth century, for example in medicine, industry, earth resources and energy conservation applications [28]. IR scanners are used in medical applications to detect cancers or other trauma, which raise the body surface temperature or in homes or industry to determine the points of maximum heat loss.

Also IR images from satellites are used in earth resources detection as well as in many other fields like global monitoring of climate changes and environmental pollution, long time prognosis of agriculture crop yield, chemical process monitoring, Fourier transform IR spectroscopy, IR astronomy, car driving, IR imaging in medical diagnostics, and others, too [28]. Figure 1.2 shows some application of infrared detectors.

In the beginning of the 1970s, US researchers have developed uncooled infrared detectors for particular military applications. IR cameras were then able to capture IR image of scenes at room temperature. Although developed for military applications, low cost IR cameras are now widely used in many commercial applications [29]. Figure 1.3 illustrates the extensive use of IR cameras in non-military applications. It should be noted that cooled infrared cameras provide superior image quality in comparison to uncooled ones. Cooled cameras are expensive both to produce and to run, so they are most regularly used in scientific research.

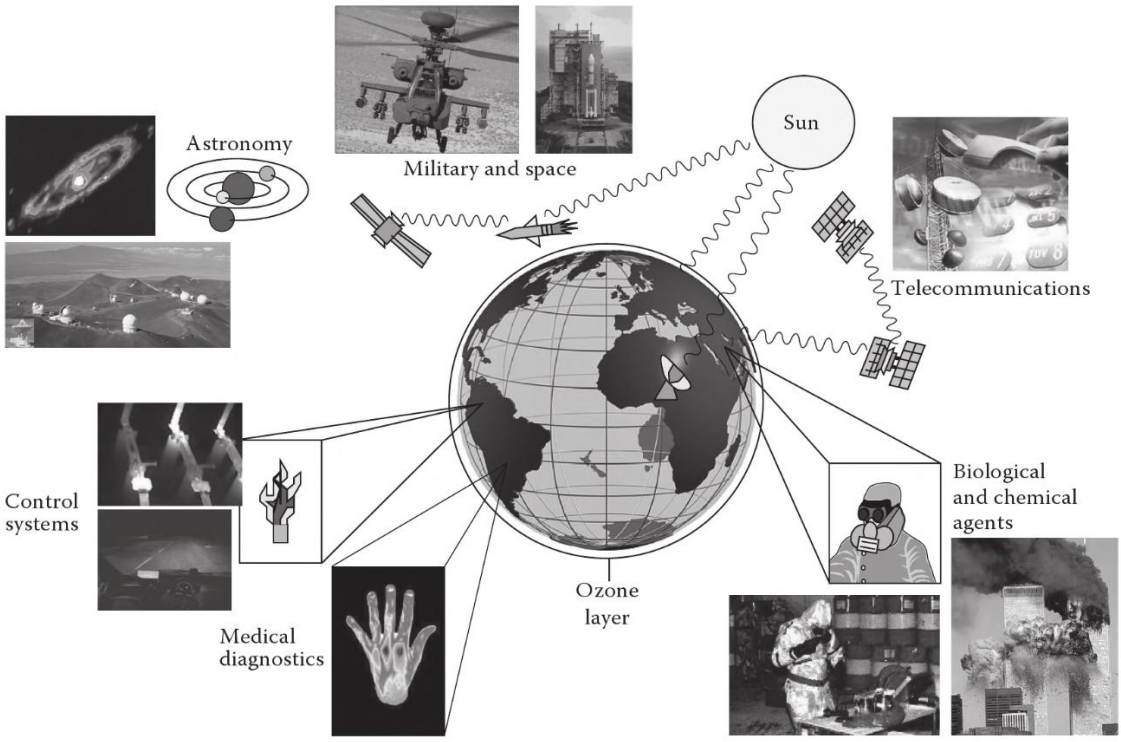

FIGURE 1.2 – Applications of infrared detectors [31].

The infrared range covers all electromagnetic radiation shorter than millimetre waves and longer than the visible. The division shown in figure 1.4 is based on the limits of spectral bands for most IR detectors.

The wavelength range of infrared radiation is given in table 1.1 . The division is based on limits

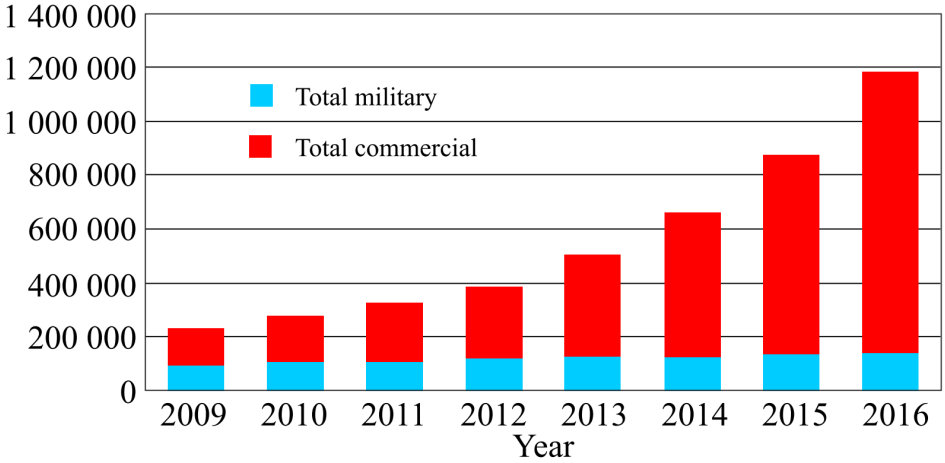

FIGURE 1.3 – Uncooled thermal camera business (units) [29].

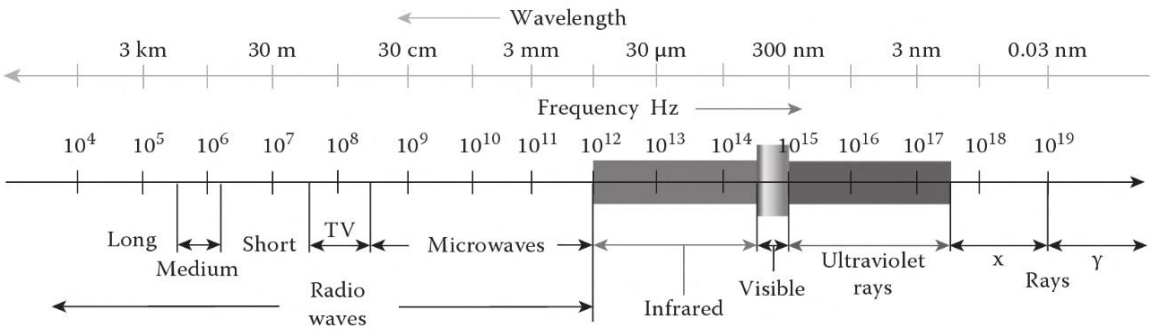

FIGURE 1.4 – Electromagnetic spectrum [31].

of spectral bands of commonly used infrared detectors. The 1 µm wavelength is the sensitivity limit of Si detectors ; the 3 µm wavelength is the sensitivity limit of PbS and InGaAs detectors ; the 6 µm wavelength is the sensitivity limit of InSb, PbSe, PtSi detectors and HgCdTe detectors ; and finally the 15 µm wavelength is the sensitivity limit of HgCdTe detectors [5].

Region (abbreviation)	**Wavelength range** (µm)
Near infrared (NIR)	$0.78 - 1$
Short wavelength IR (SWIR)	$1 - 3$
Medium wavelength IR (MWIR)	$3 - 6$
Long wavelength IR (LWIR)	$6 - 15$
Very long wavelength IR (VLWIR)	$15 - 1000$

TABLE 1.1 – Division of infrared radiation [5].

1.1 Infrared systems fundamentals

1.1.1 Thermal emission

Each material is made of atoms that vibrate more when they receive more energy. The vibration generates electromagnetic waves. So increasing the temperature of an object causes increasing the vibration and thus increasing the spectral radiant energy. All objects emit thermal radiation that is dependent on the temperature and emissivity, $\epsilon(\lambda)$.

Planck radiation law describes the radiation spectrum of a black body. A blackbody is an object that absorbs all incident radiation, regardless of angle of incidence or frequency. According to Plank's law, the emitted radiation has a spectrum that is function of the temperature only. The radiative power (or number of photons emitted) and its wavelength distribution are given

by following equations :

$$W(\lambda, T) = \frac{2\pi hc^2}{\lambda^5}[exp(\frac{hc}{\lambda kT}) - 1]^{-1} \quad W/(\text{cm}^2\ \mu\text{m}), \tag{1.1}$$

$$P(\lambda, T) = \frac{2\pi c}{\lambda^4}[exp(\frac{hc}{\lambda kT}) - 1]^{-1} \quad photons/(s\ \text{cm}^2\ \mu\text{m}), \tag{1.2}$$

where $\lambda(m)$ is the wavelength, $T(K)$ is the temperature, $h(J.s)$ is the Planck's constant, $c(m/s)$ is the velocity of light, and $k(J/K)$ is the Boltzmann's constant.

Figure 1.5 illustrates a plot of these curves for a number of blackbody temperatures. As shown in this figure, at any wavelength, the amount of energy increases with increasing temperature and the wavelength of emission peak decreases [31].

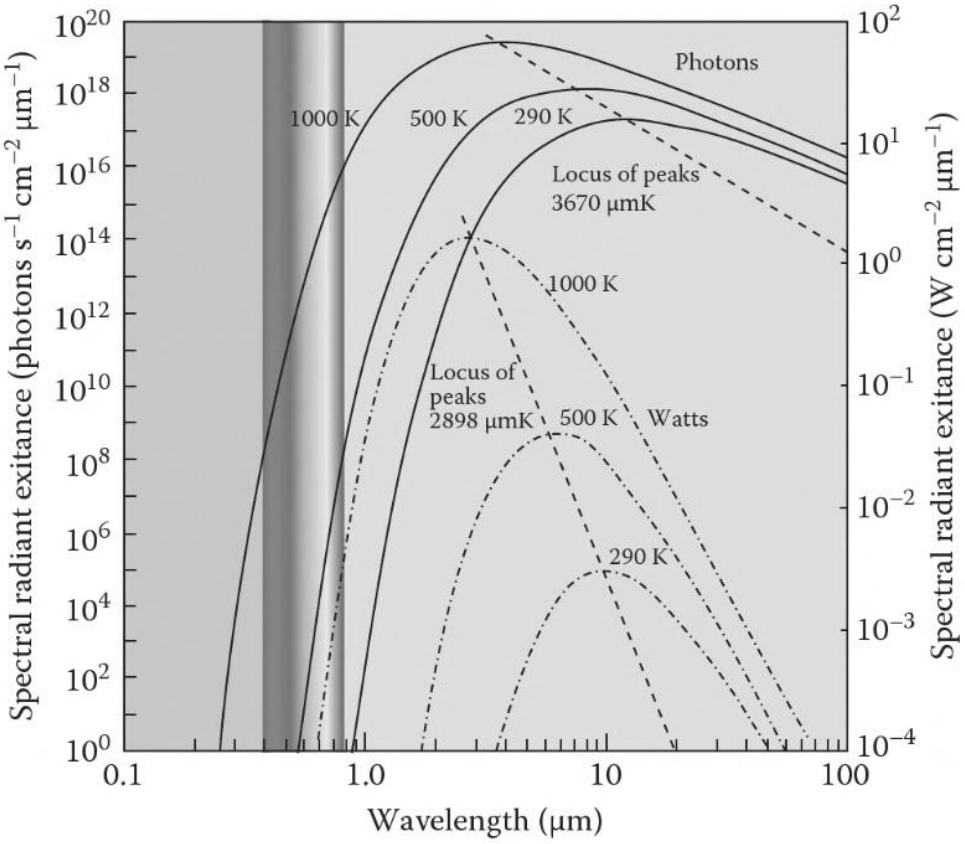

FIGURE 1.5 – Planck's law for spectral emittance [2].

1.1.2 Choice of infrared band

For any object, the total measured radiation is the sum of the transmitted, reflected and emitted radiation. As mentioned before, a blackbody absorbs all incident radiation. Objects that are not blackbodies emit only the fraction $\epsilon(\lambda)$, so the remaining fraction, $1 - \epsilon(\lambda)$, is

transmitted or reflected. This reflected radiation reduces the available contrast of object when the scene is composed of objects and backgrounds of similar temperatures. The reflections of hot or cold objects effect on the appearance of a thermal scene. Table 1.2 illustrates the power of 290 K blackbody emission and ground-level solar radiation in the MWIR and LWIR bands. We observe that reflected sunlight has an important effect on the 3-5µm band while it is negligible in 8-13µm imaging. In IR imaging devices the temperature variations or emissivity differences make a thermal image, so the thermal contrast is an important parameter. In addition, as the LWIR band has the higher sensitivity, it is preferred for high performance thermal imaging for ambient temperature objects, while the MWIR band has the greater contrast and it is more suitable for warmer object [31].

IR region (µm)	**Ground-level solar radiation** (W/m^2)	**Emission from 290 K blackbody** (W/m^2)
$3-5$	24	4.1
$8-13$	1.5	127

TABLE 1.2 – Power available in each MWIR and LWIR imaging bands [2].

1.1.3 Detectors

The two main types of detectors are thermal and photon detectors. The semiconductor IR detectors which are included in photon detector class have had an important impact in the progress of IR detector technology. For photon detectors, the radiation is absorbed by its interaction with electrons. The interaction changes the electronic energy distribution which, in turn, causes the observed electrical output signal. Based on the nature of the interaction, photon detectors are divided into different types ; the most important being intrinsic detectors, extrinsic detectors, photoemissive detectors, and quantum well detectors. The second class is composed of thermal detectors ; the radiation is absorbed and causes the temperature of the material to change. The electrical output signal results from the change of some physical properties. Thermal detectors are generally used at room temperature, have usually a slow response time, low sensitivity. They are cheap and easy to use compared to photon detectors [28].

1.2 Thermal imaging system concepts

A thermogram represents the temperature difference in a scale as an image. A technique that converts thermal radiation of a scene into a visible image is called thermal imaging. In contrast to visible radiation, thermal radiation has some advantages. It is ideal for penetrating smoke and mist and also for detecting hot or cold spots or surface with different emissivities. It is a passive technique that operates at day or night and it is a remote non-contact sensing

technique that operates in real time [2]. Temperature resolution is a parameter used for defining the performance of a thermal imager. The Noise Equivalent Temperature Difference (NETD) is the temperature sensitivity of an imager that is defined by [30] :

$$NETD = \frac{4\ f_\sharp^2\ (\Delta f)^{1/2}}{A^{1/2}\ t_{op}\ M^\star}, \tag{1.3}$$

Where $f_\sharp = f/D$ is the f-number of the detector optics, f is the focal length, D is the diameter of the lens, t_{op} is the transmission of the optics, and $M^\star$ is the figure of merit that is defined as :

$$M^\star = \int_0^\infty (\frac{\partial S}{\partial T})_\lambda\ t_{at\lambda}\ D^\star_\lambda \mathrm{d}\lambda, \tag{1.4}$$

Where $D^\star$ is the detector performance, $(\frac{\partial S}{\partial T})_\lambda$ is the spectral dependence of the emitted radiation, t_{at} and the atmospheric transmission.

"NETD is the difference of temperature of the object required to produce an electric signal equal to the rms noise at the input of the display" [30]. Temperature resolution depends on responsivity and noise of the detector, SNR of the signal processing circuitry, and efficiency of the optical system. The NETD must be low for high sensitivity.

1.3 Measuring systems

Generally, infrared measurement systems can be divided in two groups. The first group comprises non-contact thermometers that are used for non-contact temperature measurement. Radiometers are in the second group and are used for different quantities measurement.

1.3.1 Non-contact thermometers

Infrared thermometers measure temperature indirectly in two steps. The first step consists of measuring the power of the optical radiation that hits the system detector in one or more spectral bands. In the second step, the temperature of the object is determined based on the measured signals. IR thermometers are usually composed of at least five or more blocks. An optical objective is used to limit field of view the thermometer and to increase the amount of radiation emitted. The signal is also amplified, converted into more convenient electronic form and digitized. Finally, a visualization block is used to display the results. The infrared thermometers are divided into group based on different criteria : number of measurement points, number of spectral bands, presence of an additional co-operating source, type of transmission media and width of system spectral bands [5].

Non-contact thermometers use two measurement methods. Passive systems are used to measure the object temperature passively only based on the power of radiation emitted by the object in one or more spectral bands. For the second method, an additional co-operating source is used to emit radiation in direction of the tested object and then the thermometer measure

the reflected radiation. This allows obtaining information about the emissive properties of the object to improve the accuracy of non-contact temperature measurements. In short, an active system consist of a co-operating source which emits radiation towards the tested object, and of a classical passive thermometer to measure both the radiation emitted by the source and object and the radiation reflected and emitted by the object.

All classification of non-contact thermometers are shown in figure 1.6. Based on the number and location of measurement points, they can be divided into pyrometers, line scanners and thermal cameras. According to the width of system spectral band, they can be categorized into total radiation thermometers, band-pass thermometers and narrow-band thermometers. They are also classified into single-, dual- and multiband systems, based on the number of system spectral bands [5].

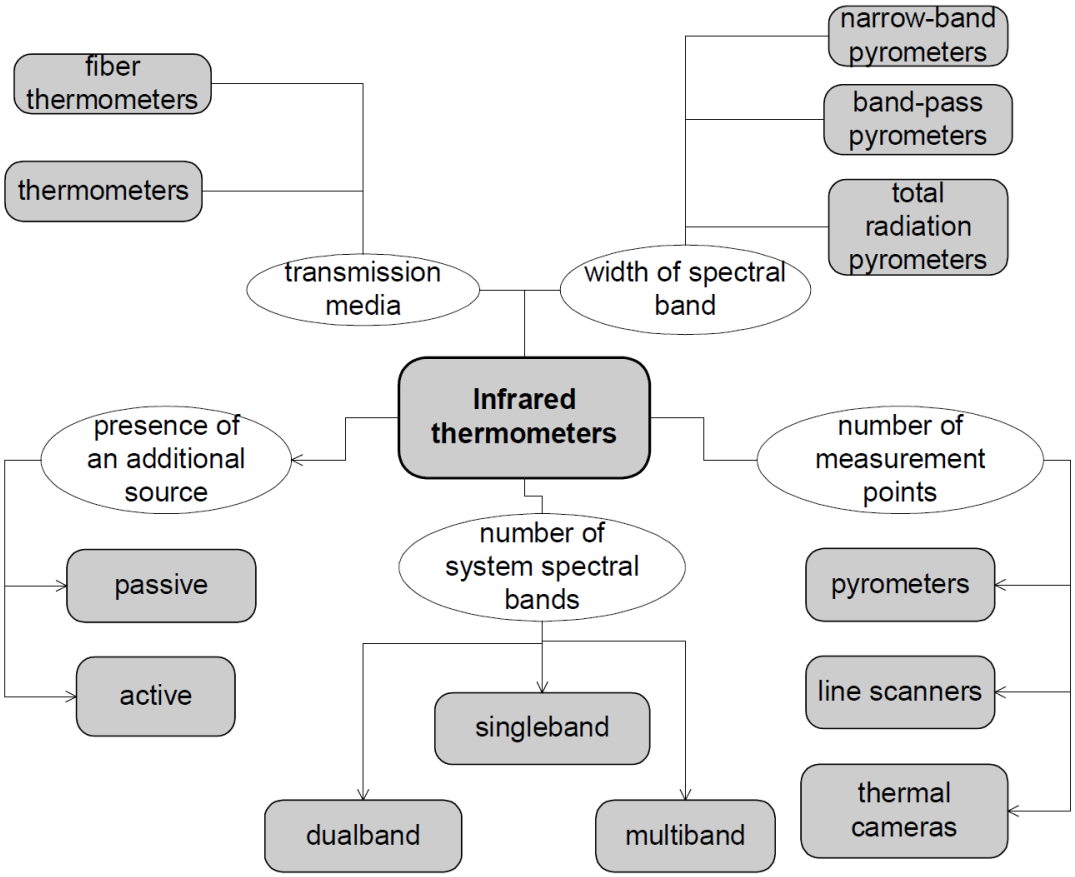

FIGURE 1.6 – Classifications of non-contact thermometers [5].

1.3.2 Radiometers

Since IR thermometers measure the temperature based on the signal generated by the radiant flux coming to the detector, they can be considered as radiometers. However, IR thermometers are used to measure temperature, not radiant flux. According to Chrzanowski [5], IR

radiometers are designed to measure the amplitude of infrared radiation, radiant properties of materials, or infrared detector parameters. IR radiometers are classified based on different criteria : number of measurement points, number of spectral bands, and measured quantity. Figure 1.7 shows all classification of infrared radiometers.

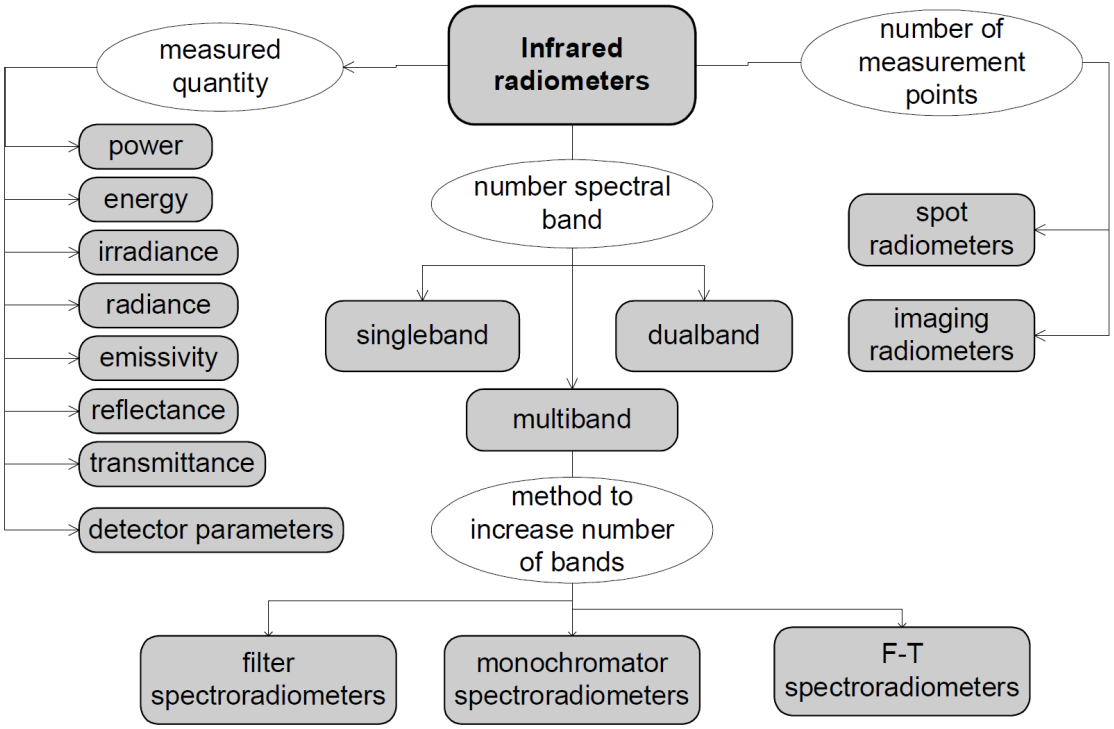

FIGURE 1.7 – Classifications of infrared radiometers [5].

In general, types of quantity of infrared radiation measured by radiometers are i) radiance, irradiance, radiant intensity, radiant energy, radiant power, radiant exposure, ii) radiant properties of materials such as emissivity, reflectance and transmittance and iii) parameters of infrared detectors such as responsivity, and detectivity. IR radiometers also can be described on the basis of the number of spectral bands : single-band radiometers, dual-band radiometers and multiband radiometers [5].

Chapter 2

Literature review of defect detection and depth estimation approaches

Since defect detection and estimating the depth of defect are important in our project, this chapter presents an introduction of important methods uses to detect defects and estimate their depth.

2.1 Related works on defect detection

Several methods have been proposed for object detection. Some approaches use thresholding techniques while the others are based on a criterion. Segmentation of thermal images usually has been done by thresholding methods, due to their simplicity and ease of implementation. In the following, we review some of the most important defect detection methods.

As presented in [12], we can categorize the defect detection methods in two groups : nondedicated and dedicated algorithms. Nondedicated algorithm refers to the approaches which have not specifically been proposed for thermal images while dedicated methods are specifically designed for thermal applications.

2.1.1 Nondedicated algorithms

In this section we explain briefly four nondedicated algorithms.

Otsu's method

A common thresholding technique was proposed by Otsu [24] in which the threshold is selected by maximizing the between-class variances or minimizing the within-class variances. We briefly introduce it in the following.

Let $F = \{f_1, f_2 \dots f_{M\times N}\}$ represent the gray level image of size $M \times N$, where $f_i \in [1, 2, \dots, L-1]$ is the gray value of the i^{th} pixel. By denoting $f(g)$ as the number of pixels with gray level g, the probability of occurrence of gray level g is defined by :

$$p(g) = \frac{f(g)}{M \times N}, \qquad g = 0, 1, ..., L-1 \tag{2.1}$$

The average gray level of the entire image is computed as :

$$\mu_T = \sum_{g=0}^{L-1} g.p(g) \tag{2.2}$$

We want to divide the pixels of the image into two classes $C_0 = \{0, 1, \dots, t\}$ and $C_1 = \{t+1, t+2, \dots, L-1\}$(object and background, or background and object), where t is the threshold value. The probabilities of the two classes are :

$$p_0(t) = \sum_{g=0}^{t} p(g), \tag{2.3}$$

$$p_1(t) = \sum_{g=t+1}^{L-1} p(g). \tag{2.4}$$

So the mean value of each class can be computed as :

$$\mu_0(t) = \sum_{g=0}^{t} \frac{g.p(g)}{p_0(t)}, \tag{2.5}$$

$$\mu_1(t) = \sum_{g=t+1}^{L-1} \frac{g.p(g)}{p_1(t)}, \tag{2.6}$$

It's obvious that $p_0(t)\mu_0(t) + p_1(t)\mu_1(t) = 1$.

The between class variance of C_0 and C_1 is :

$$\sigma_B^2(t) = p_0(t)(\mu_0(t) - \mu_T)^2 + p_1(t)(\mu_1(t) - \mu_T)^2 = p_0(t)\mu_0^2(t) + p_1(t)\mu_1^2(t). \tag{2.7}$$

Hence, the optimal threshold $t^\star$ can be determined as :

$$t^\star = \arg\max_{0<t<L-1} \sigma_B^2(t) = \arg\max_{0<t<L-1} \{p_0(t)\mu_0^2(t) + p_1(t)\mu_1^2(t)\}. \tag{2.8}$$

Otsu's method is a good thresholding method for general real world images. This method is simple and easy to realize and works well when the histogram of the image is close to a bimodal distribution (i.e. has two peaks or modes). Many approaches based on Otsu's methods have been proposed, one of which is described in the following.

Valley-emphasis method

The valley-emphasis method [23] showed that Otsu's method gives an incorrect threshold value when the difference between the object variance and the background variance is large or when the histogram is unimodal or close to unimodal. As shown in figure 2.1, a good threshold value in a bimodal distribution exists at the valley of the two peaks and, for an unimodal distribution, it exists at the bottom rim of a single peak. So, it is clear that the probability of occurrence at the threshold value is small. Otsu's method fails if the histogram is unimodal or close to unimodal (See figure 2.2).

The valley-emphasis method proposes an improvement of Otsu's method, which obtains an appropriate value for the threshold. The threshold is selected in such way that it has a small probability of occurrence (valley in the histogram) which maximizes the between class variance, as in Otsu's method. The formulation for the valley-emphasis method is :

$$t^{\star} = \arg\max_{0<t<L-1}\{(1-p(t))(p_0(t)\mu_0^2(t) + p_1(t)\mu_1^2(t))\}. \tag{2.9}$$

The term $1-p(t)$ is a weight, which ensures that the selected threshold has a low probability of occurrence.

The valley-emphasis method works well on images neading multilevel thresholding as shown in figure 2.3. Figures 2.3 (b, c) shows the results of valley-emphasis and Otsu methods using tri-level thresholding. Figure 2.3 (d) shows the threshold values computed by the two methods.

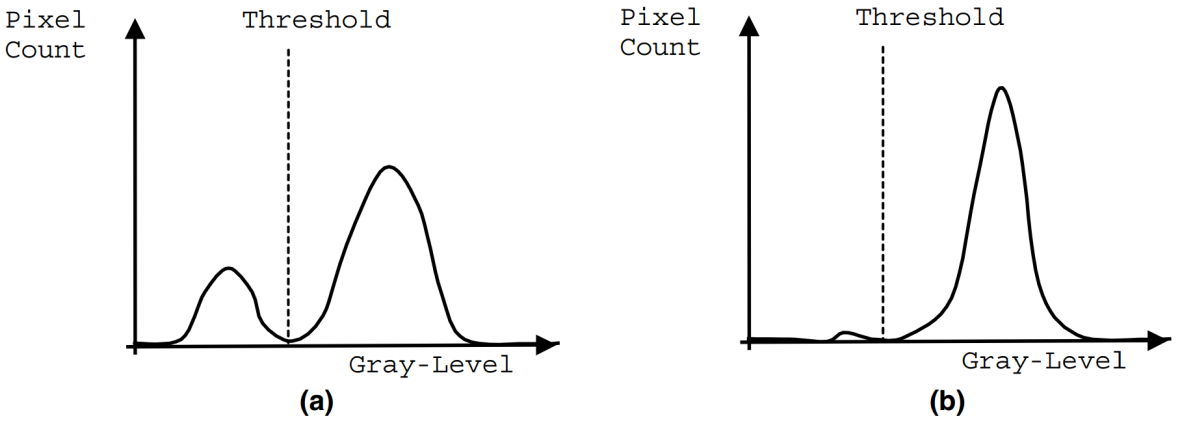

FIGURE 2.1 – Optimal threshold selection in gray-level histogram : (a) bimodal ; (b) unimodal [23].

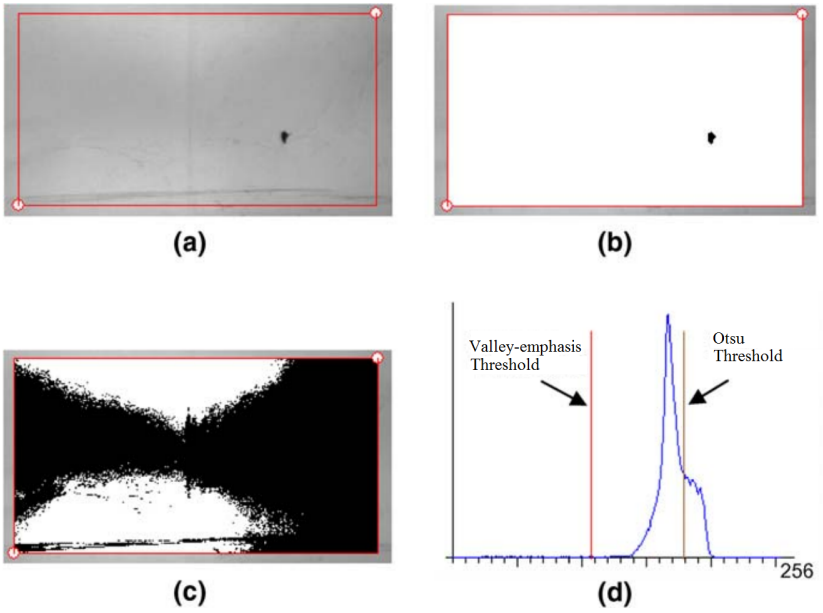

FIGURE 2.2 – Problem with Otsu's method in thresholding small defects : (a) original image ; (b) Valley-emphasis threshold result ; (c) Otsu's threshold result ; (d) histogram and threshold values [23].

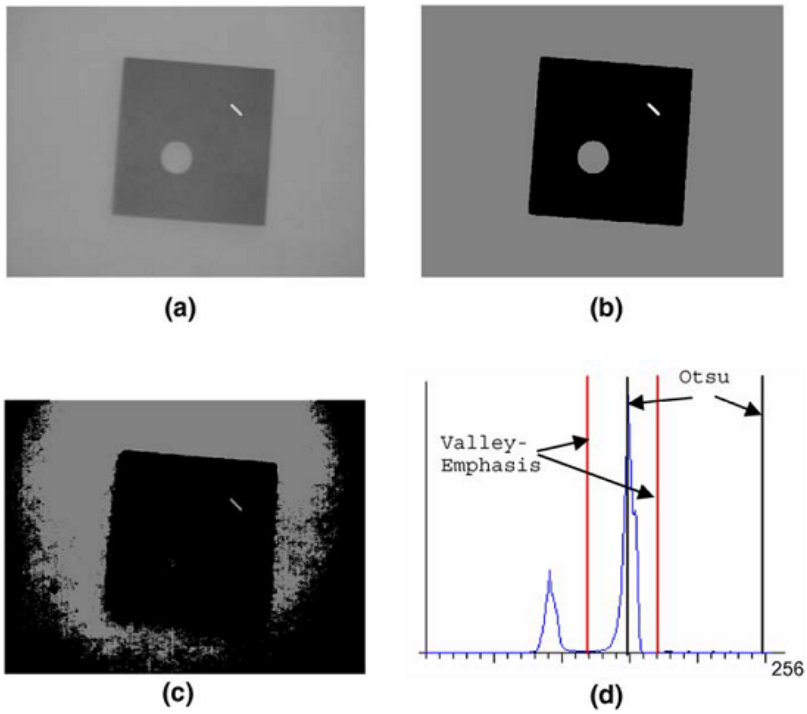

FIGURE 2.3 – Valley-emphasis and Otsu threshold results for a part image : (a) part image ; (b) valley-emphasis tri-level threshold result ; (c) Otsu tri-level threshold result ; (d) histogram and threshold values [23].

Neighborhood valley-emphasis method

The idea of the valley-emphasis method is conceptually simple. However, the authors in [7] showed that the variation of the weight might be smaller when the variance of the object is very different from that of the background. The method fails when the object is very small compared to the whole scene. Therefore they used neighborhood information at the valley point to improve segmentation quality. This method assigns weights equal to $\sigma_B^2(t)$ with the neighborhood information at the threshold point.

For gray level g it defines the neighborhood gray value $\bar{h}(g)$ as the sum of the neighborhood probability in the interval $n = 2m + 1$, while n is the neighborhood length :

$$\bar{h}(g) = \sum_{i=-m}^{m} h(g+i), \tag{2.10}$$

Finally, maximizing the following function allows to select the optimal threshold :

$$t^\star = \arg\max_{0<t<L-1}\{(1-\bar{h}(t))(p_0(t)\mu_0^2(t) + p_1(t)\mu_1^2(t))\}. \tag{2.11}$$

The new weight $1 - \bar{h}(t)$ ensures that the best threshold has a small probability while the sum of its neighborhood probability is small, too. Moreover, when the variances of object and background are very different, the neighborhood valley-emphasis method can segment the image as well. Figure 2.4 (b) shows the segmentation results of an image. This figure illustrates the values of histogram and threshold for Otsu, Valley-emphasis and neighborhood Valley-emphasis methods. This figure demonstrates the performance of neighborhood Valley-emphasis method.

Based on equation 2.10 the neighborhood gray value $\bar{h}(t)$ consists of the sum of the neighborhood probabilities and causes a smoothing effect which allows the neighborhood-valley-emphasis method to better segment the noisy image compared to the Otsu and valley-emphasis methods. This approach can be used for images submitted to multilevel thresholding as well.

Active contour method

Active contour is a method to detect objects in a given image u_0 via techniques of curve evolution. The basic idea is to start with an initial curve C and to deform iteratively the curve to the boundary of the objects under some constraints of u_0.

The major problem is finding the contour C that separates the object ω from the background, such that intensity variation inside C becomes minimum and is outside maximum.

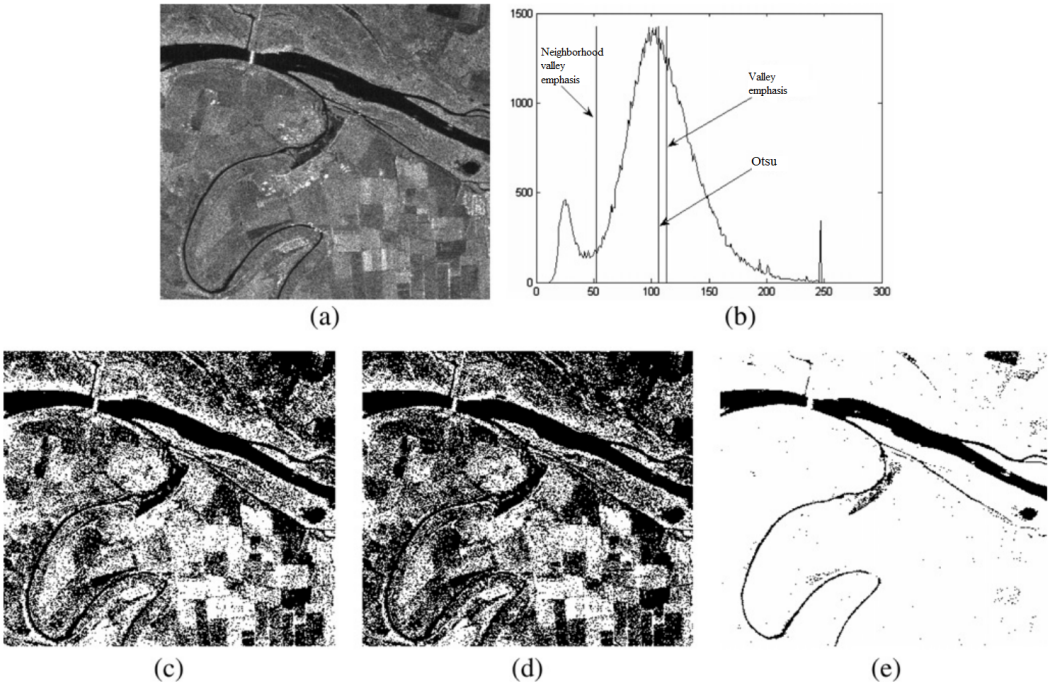

FIGURE 2.4 – Segmentation results of a standard image : (a) original image, (b) histogram and threshold values, (c) Otsu segmentation result with threshold 106, (d) valley-emphasis segmentation result with threshold 113, (e) neighborhood valley-emphasis segmentation result with threshold 52 [7].

Chan and Vese in [4] formulated this problem by minimizing the following energy function :

$$\begin{aligned} F(c_1, c_2, C) = \mu Length(C) \ + \ vArea(inside(C)) \\ +\lambda_1 \int_{inside(C)} (u_0 - c_1)^2 \mathrm{d}x \\ +\lambda_2 \int_{outside(C)} (u_0 - c_2)^2 \mathrm{d}x, \end{aligned} \tag{2.12}$$

where, first and second terms of the above equation are regularization terms for minimizing area and contour length. $\mu \geq 0, v \geq 0, \lambda_1 > 0$ and, $\lambda_2 > 0$ are fixed parameters controlling the effect of each term in minimizing F, c_1 and c_2 are the mean intensities inside and outside C, respectively. The length parameter μ is not the same for all images. To detect objects varying in size μ should be small. μ has to be larger for detecting large objects only.

Figure 2.5 shows that this method works well on a noisy image, with various shapes and an interior contour and can detect and preserve the location of boundaries. Chan and Vese in [4] proposed an active contour which evolves in the original image to associate a piecewise-constant approximation of it. This method doesn't need to smooth the initial image.

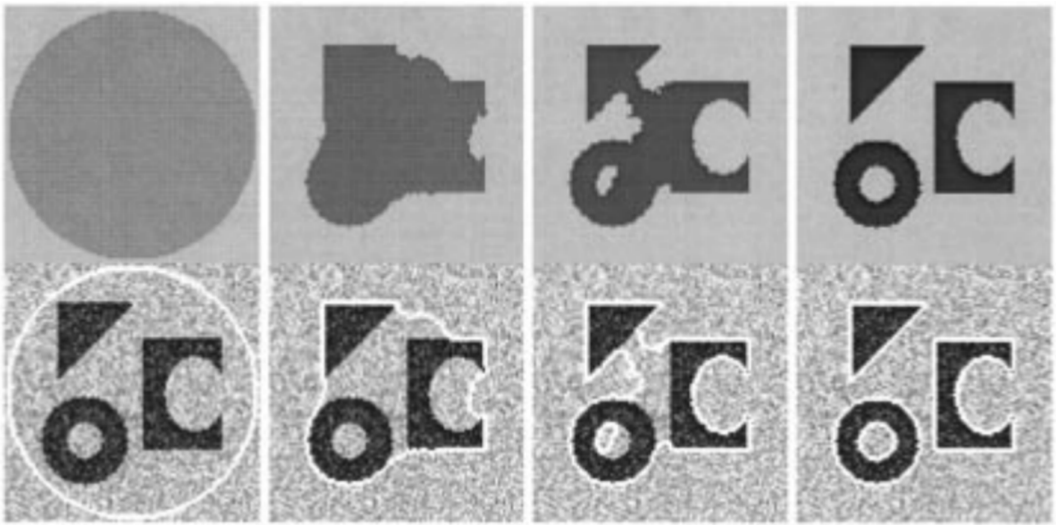

FIGURE 2.5 – Detection of different objects from a noisy image, with various shapes and with an interior contour [4].

2.1.2 Dedicated algorithms

These algorithms extract objects from background that are usually represented by *warm*, *hot* or, *bright* object.

Hamadani method

To extract a warm object in a thermal image, Hamadani [10] proposed to the first order statistical properties of the image, like the mean and standard deviation, (μ, σ). The threshold is computed by :

$$T = k_1\mu + k_2\sigma, \tag{2.13}$$

where $\mu = \frac{1}{M\times N}\sum_{i=1}^{M}\sum_{j=1}^{N} f(i,j)$, $\sigma = \sqrt{\frac{1}{M\times N}\sum_{i=1}^{M}\sum_{j=1}^{N}(f(i,j)-\mu)^2}$, coefficients k_1 and k_2 need to be determined manually so the method is not automatic. Figure 2.6 shows the segmentation result for various k_1 and k_2. As the constants k_1 and k_2 have great effect on the threshold value, they should be adjusted properly ; since for different images they will have different values.

Heriansyah method

Heriansyah and Abu-Bakr [12] proposed a technique to enhance the contrast of the defects based on local neighborhood pixel intensity operation. This local intensity operation (LIO) works in two modes, either by brightening the pixels for detecting hot spots that is called the intensity brightening operation (IBO) or by darkening the pixels for detecting cold spots that is called the intensity darkening operation (IDO). IBO assumes the brightest area is the

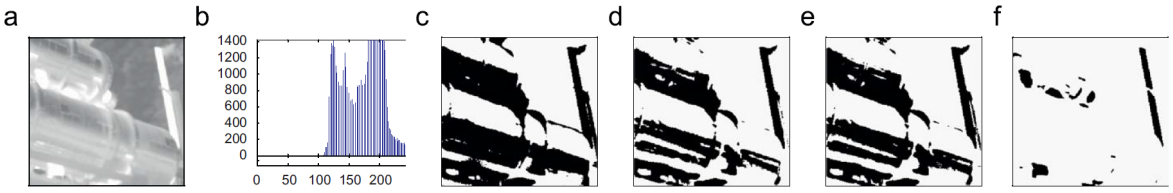

FIGURE 2.6 – (a) Thermal image and (b) its histogram, thresholded using Hamadani's method with (c) $k_1 = 1$, $k_2 = 1$, $T = 189$, (d) $k_1 = 1$, $k_2 = 2$, $T = 200$, (e) $k_1 = 1$, $k_2 = 1.5$, $T = 194$, and (f) $k_1 = 1$, $k_2 = 7$, $T = 253$[12].

defective area since in IDO the defect is located in darkest area and the darkest area is the sound area.

If z_0 is a pixel in a thermal image, the product of pixels with its neighborhood is defined as :

$$Z = \prod_{0}^{8} z_k, \tag{2.14}$$

where $z_1, z_2, \ldots, z_8$ are the neighboring pixels of z_0. So IBO and IDO respectively are :

$$g(i,j) = Z, \tag{2.15}$$

$$g(i,j) = \begin{cases} \frac{1}{Z}, & \text{for } Z \neq 1 \\ 1, & \text{for } Z = 1 \end{cases}, \tag{2.16}$$

where $g(i,j)$ is the pixel at row i and column j in the new image. As shown in figure 2.7, IBO is able to detect hot areas while IDO can detect cold areas. Using both operations can detect hot and cold defects.

This method uses three simple histogram-based thresholding techniques to segment the defects : mean absolute thresholding (MAT), mean relative thresholding (MRT), and minimum frequency thresholding (MFT).

Threshold value in MAT is calculated by obtaining the mean value between the minimum and the maximum gray level values. By denoting the gray level of the image as $i = i_1, i_2, \ldots, i_L$, the threshold value is defined as :

$$T = round[\frac{i_L - i_1}{2}]. \tag{2.17}$$

MRT is a special case of MAT, in which the threshold value is determined by the gradient of the histogram. Let $h(i)$ be the image histogram at gray level i. Then, the gradient is calculated as :

$$r(i) = h(i+1) - h(i), \tag{2.18}$$

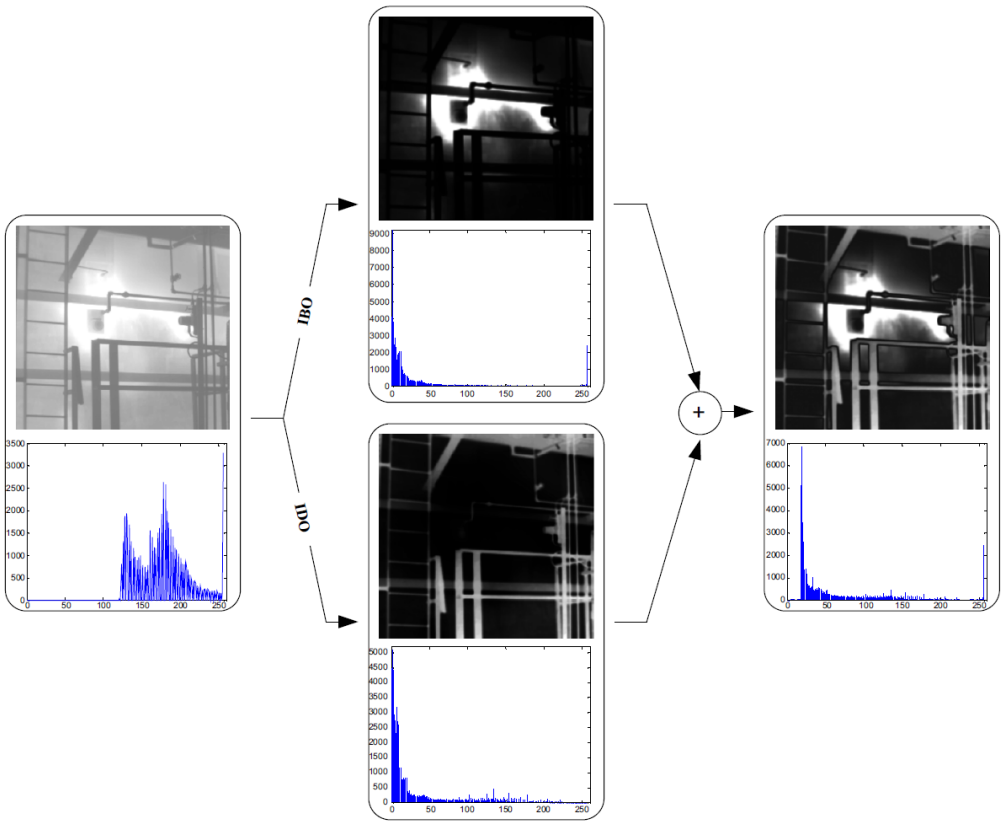

FIGURE 2.7 – IBO and IDO operations and their combinations (which is simply their summation) [12].

$$\text{where, } i_1 = \begin{cases} r(i), & \text{if } (r(i) > r(i-1)) and (r(i) > r(i+1)) and r(i) \geq 0 \\ 0, & \text{otherwise} \end{cases}$$

$$\text{and } i_L = \begin{cases} r(i), & \text{if } (r(i) < r(i-1)) and (r(i) < r(i+1)) \\ 0, & \text{otherwise} \end{cases}.$$

In MFT, the left-most minimum frequency gray-level is selected as the thresholding value. This selection is based on the assumption that if there is a gray level discontinuity in the image histogram at the left-most minimum frequency gray level (see figure 2.8), meaning that these gray level values correspond to the background of the image. So the threshold value is defined as :

$$T = i \mid_{\{\min h_i\}}, \qquad where\ i = 0, ..., L-1 \tag{2.19}$$

As discussed in [12], in some cases the IBO can be repeated 2 or 3 times until the defects are detected clearly. This method can segment both hot and cold defects from thermal images of petrochemical equipment as well. The serious drawback occurs when the temperature variation is less and this method does not work well.

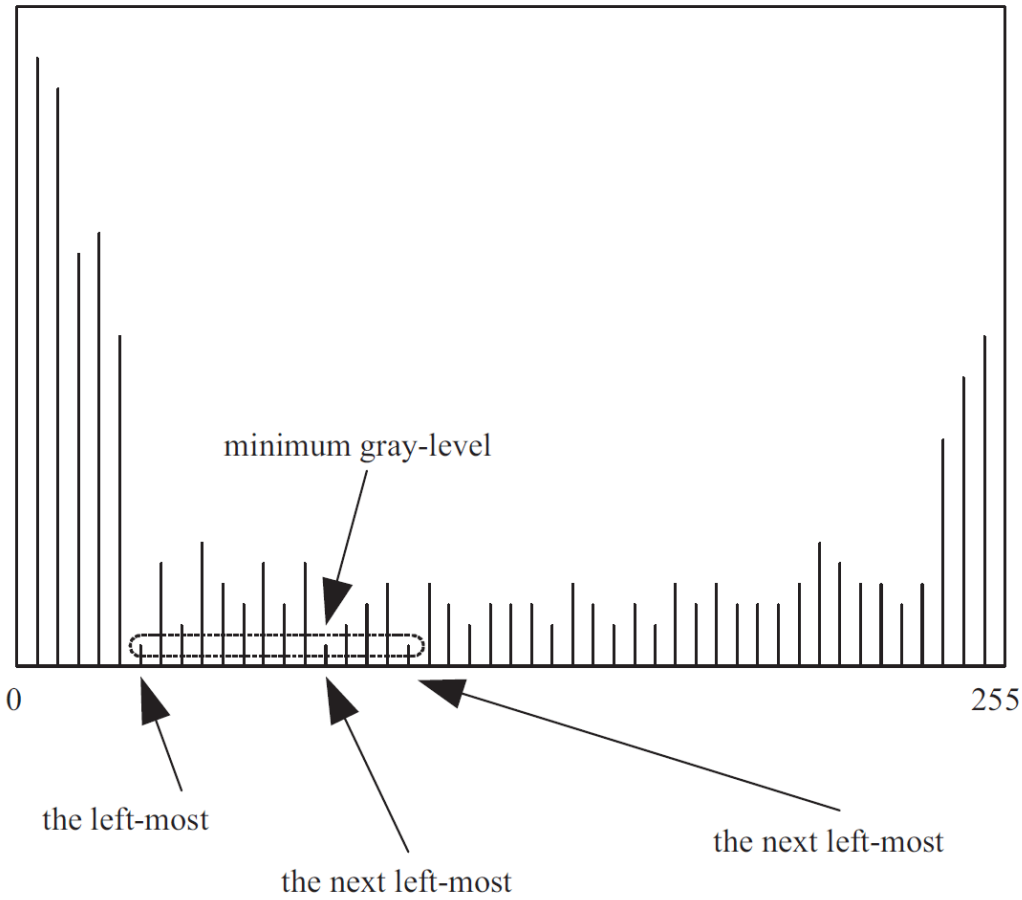

FIGURE 2.8 – Minimum frequency thresholding principle [12].

2.2 Related work on depth estimation

In the last two decades, many techniques in pulsed thermography have been proposed for estimating the depth. Most of them predict defect depth based on a *characteristic time*. For the different methods of defects based on thermal contrast or logarithmic scale, the peak time of the first or second derivative of the temperature curve are usually considered as this characteristic time. Most of these methods need a reference point from the sound area. A schematic diagram of pulsed thermography is shown in figure 2.9. A pulsed thermal energy heats the front surface of the detected sample. The generated heat is transferred from the front surface to the interior of the sample because of heat conduction, and leads to a continuous decrease of the surface temperature. In the defect area which is filled by air, the heat flux faces a higher thermal resistance that reduces the heat transfer rate. Therefore the defect area has a higher temperature than the sound area. On the other hand, the sound area cools down faster than the defect area. The hot area appears earlier if the defect is shallow and later if it is deep. All this time, an IR camera monitors the surface temperature [21; 6]. The surface temperature decay curves in defect area (T) and sound area (T_r) at points 1 and 2, respectively, are shown

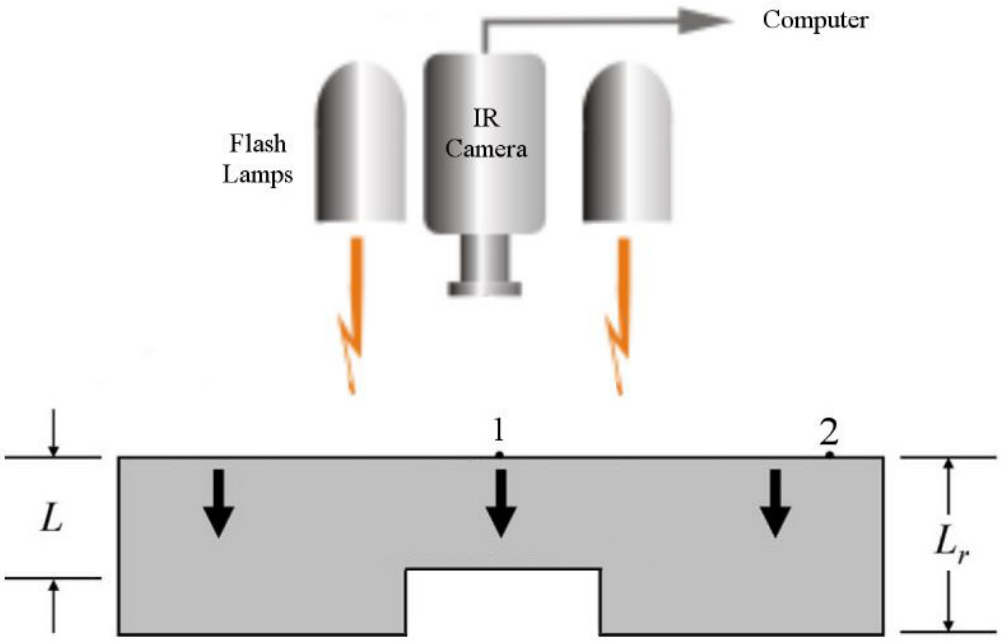

FIGURE 2.9 – Sketch map of the pulsed thermographic principle.

in figure 2.10. The one-dimensional solution of heat conduction was determined by [25]. They defined the decay of the surface temperature T with time t as :

$$T(t) = \frac{Q}{\rho C L}[1 + 2\sum_{n=1}^{\infty} exp(-\frac{n^2\pi^2}{L^2}\alpha t)], \tag{2.20}$$

where $Q(J/m^2)$ is the input energy per unit area, $\rho(kg/m^3)$ is the density, $C(J/(kgK))$ is the specific heat, $\alpha(m^2/s)$ is the thermal diffusivity and, $L(m)$ is the sample thickness. The temperature contrast is defined as :

$$\Delta T = T - T_r. \tag{2.21}$$

In the following we describe a categorization of different thermography methods.

Peak Temperature Contrast Method

Based on the Peak Temperature Contrast Method, the temperature contrast between the defect area and a reference (sound area) is dependent on two parameters ; the difference between the defect depth and the specimen thickness, and the lateral size of the defect. The second parameter is because of the induced three-dimensional heat conduction around the defect.

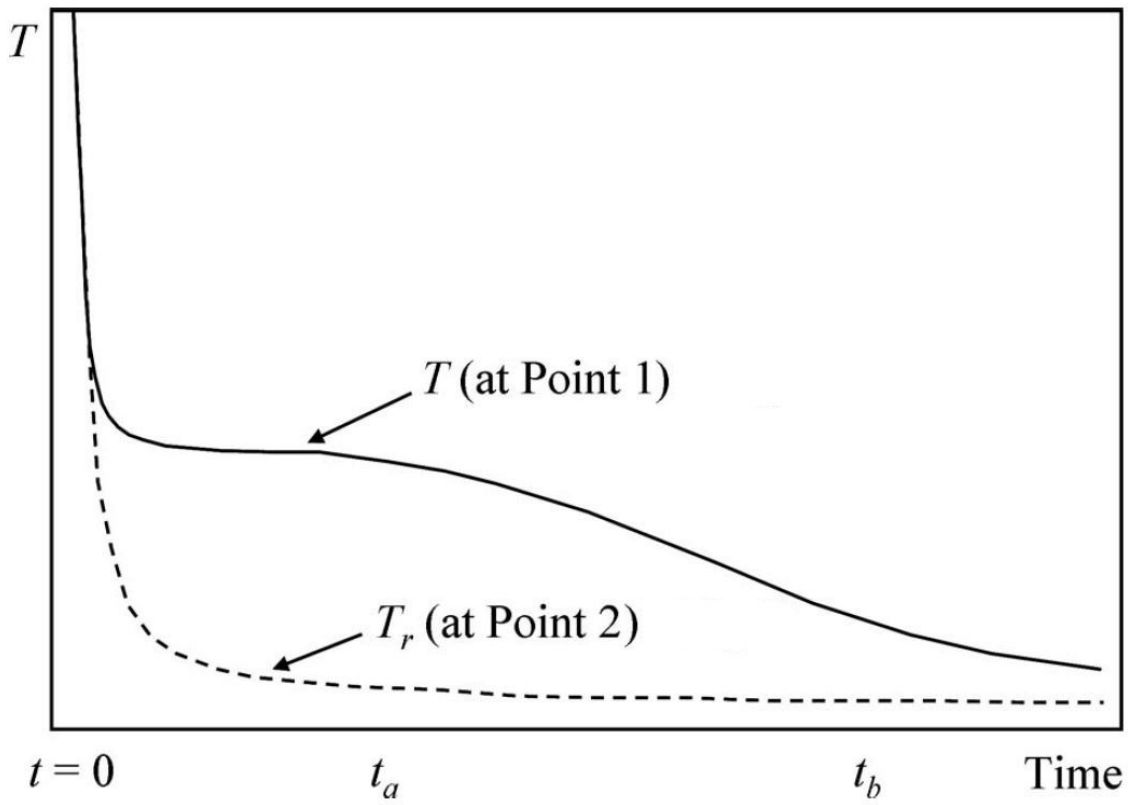

FIGURE 2.10 – Surface temperature decay curves in defect area (T) and sound area (T_r) [34].

However, the heat transfer in the defect area during the transient period can be considered one dimensional when the lateral size of the defect is large and the heat conduction through the air gap is negligible. It is similar for the sound area. Therefore the temperature contrast between these two areas can be obtained from the one dimensional heat conduction solution of equation 2.20 and the temperature contrast of equation 2.21 for thicknesses in defect area (L) and sound area (L_r) can be expressed as :

$$\Delta T = T - T_r = \frac{Q}{\rho C L}[1 + 2\sum_{n=1}^{\infty} e^{-n^2\omega}] - \frac{Q}{\rho C L_r}[1 + 2\sum_{n=1}^{\infty} e^{-n^2\omega_r}], \tag{2.22}$$

where $\omega = (\pi^2 \alpha t)/L^2$ and $\omega_r = (\pi^2 \alpha t)/L_r^2$ are dimensionless times for the two areas. By denoting $y = L/L_r$ as the thickness ratio and $V = T\rho C L_r/Q$ as the normalized temperature, equation 2.22 can be expressed as :

$$\Delta V = y^{-1} - 1 + 2\sum_{n=1}^{\infty}(y^{-1} e^{-n^2\omega_r/y^2} - e^{-n^2\omega_r}). \tag{2.23}$$

As observed in equation 2.23, the temperature difference approaches $\Delta V_\infty = y^{-1} - 1$, which is constant when time increases to infinity. As illustrated in figure 2.11, ΔV is smaller for larger

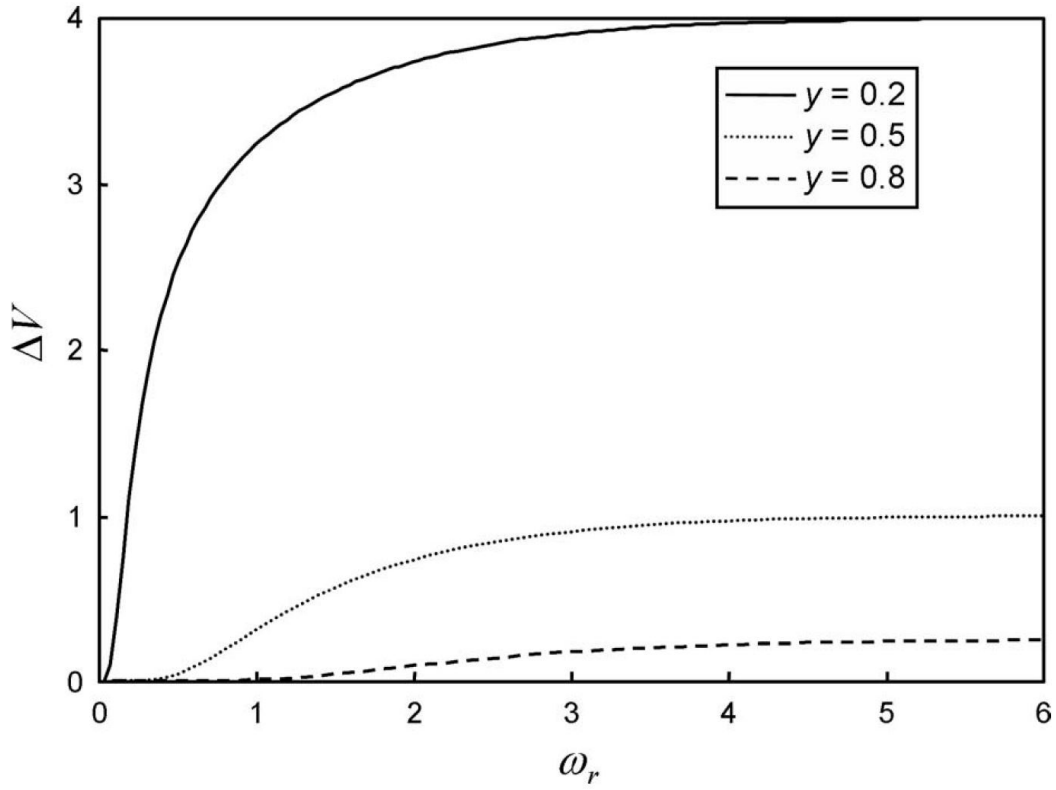

FIGURE 2.11 – Temperature contrast ΔV as a function of ω_r [34].

y values. The temperature differences between defect area and sound area can be compared and analyzed with this equation. Because of the 3D heat conduction effect, the temperature contrast first increases with time and then decreases. A characteristic time corresponds to the peak time of the maximum thermal contrast. It was found that the peak contrast time is approximately proportional to the square of the defect depth, and the proportionality coefficient depends on the defect size ; the smaller the size of defect, the lower the maximum contrast and the shorter the peak contrast time [35; 9; 11; 34].

Peak Temperature Contrast Slope Method

In the Peak Temperature Contrast Slope Method, a characteristic time which is referred to the peak slope time t_s, corresponds to the peak time of the first derivative of the thermal contrast. The temperature-contrast slope has been used for defect depth prediction and, from equation 2.23, can be expressed as :

$$\frac{d(\Delta V)}{d\omega_r} = \sum_{n=1}^{\infty} 2n^2(e^{-n^2\omega_r} - y^{-3}e^{-n^2\omega_r/y^2}), \tag{2.24}$$

where ω_r is the dimensionless time for the sound area thickness. Figure 2.12 shows the slope of the temperature contrast $\frac{d(\Delta V)}{d\omega_r}$ as a function of ω_r for different thickness ratios. It was found

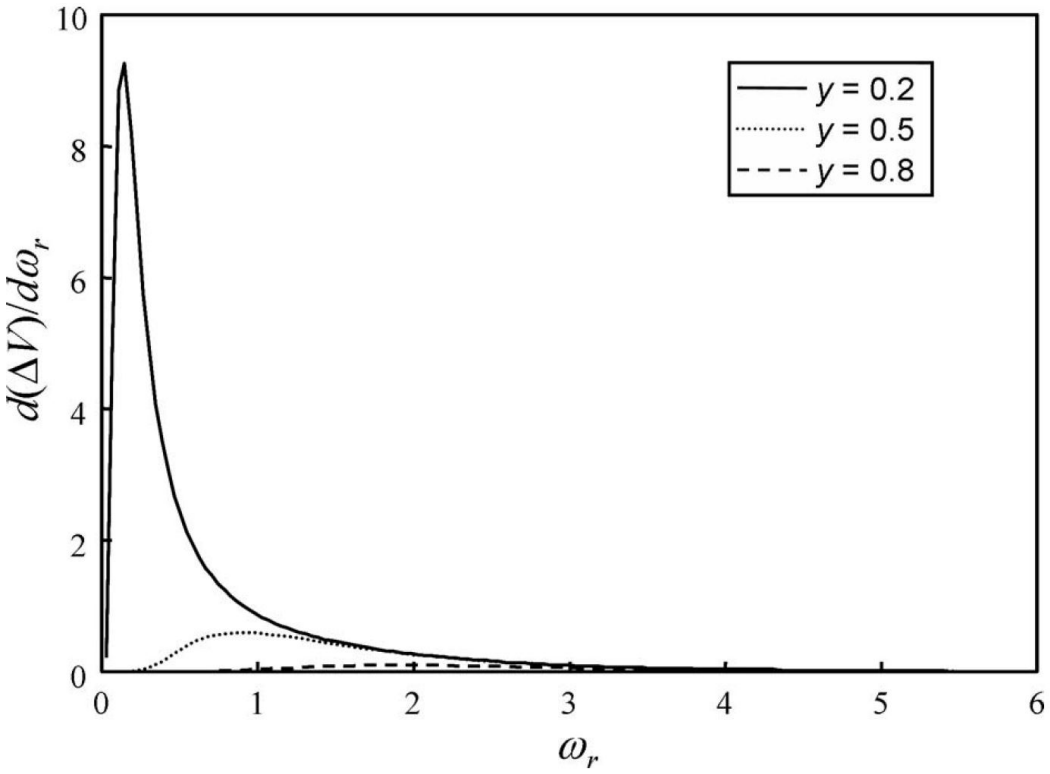

FIGURE 2.12 – Slope of temperature contrast $\frac{d(\Delta V)}{d\omega_r}$ as a function of ω_r [34].

that the peak slope time t_s is also approximately proportional to the square of the defect depth, and the proportionality coefficient does not depend on defect size [8; 6; 1]. Solving equation 2.24 based on t_s determines the relationship between defect depth L and peak slope time from the condition $\frac{d^2(\Delta V)}{d\omega_r^2} = 0$. Figure 2.13 shows the dimensionless peak slope time ω_s and peak slope $\frac{d(\Delta V_s)}{d\omega_r}$ as functions of thickness ratio y. As illustrated in this figure the peak slope time ω_s is constant and independent of y for $y < 0.5$, so the relationship between the peak slope value $\frac{d(\Delta V_s)}{d\omega_r}$ and y can be used to predict the defect depth [34]. The authors in [1] demonstrated the relationship between t_s and the defect depth L as :

$$t_s = \frac{3.64L^2}{\pi^2\alpha}, \tag{2.25}$$

where the constant 3.64 is very close to the theoretical solution, as shown in figure 2.13. A major problem of these methods is to determine a reference point from the sound area. Several approaches have been proposed to obtain this reference automatically. The authors of [1] proposed a method to use the average temperature of the entire surface as the reference temperature.

The aforementioned methods are all based on time domain processing.

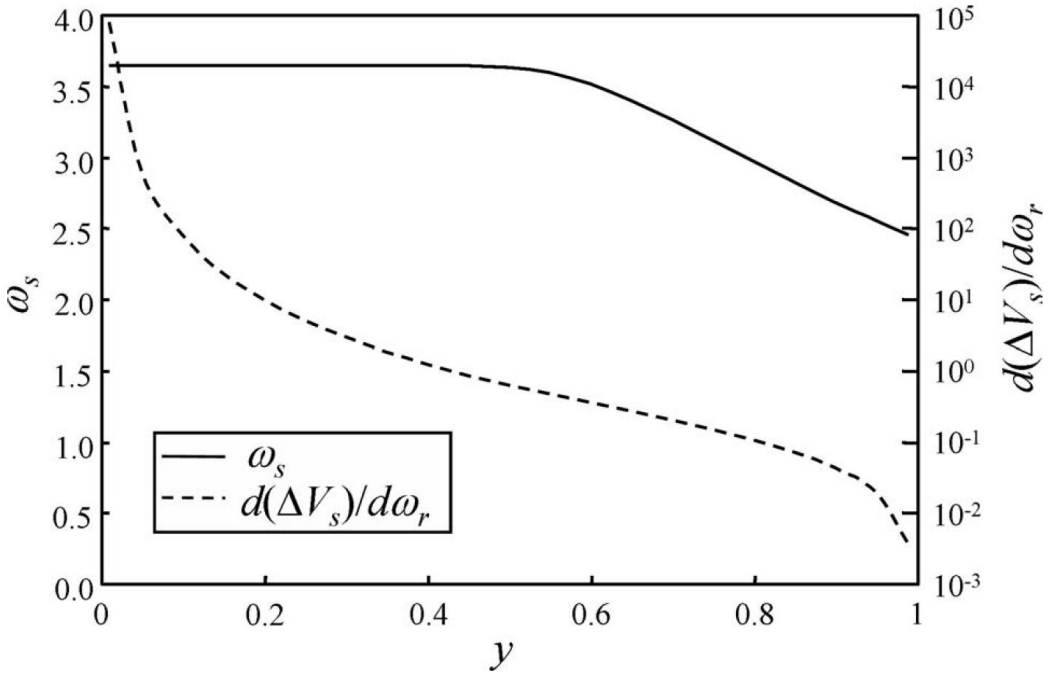

FIGURE 2.13 – Dimensionless peak-slope time ω_s and peak slope $\frac{d(\Delta V_s)}{d\omega_r}$ as functions of thickness ratio y [34].

Pulsed Phase Thermography Method

The Pulsed Phase Thermography Method is proposed to calculate defect depth in the frequency domain. By applying the Discrete Fourier Transform (DFT), the temperature data can be defined as :

$$F_n = \sum_{k=0}^{N} T(k)\ e^{\frac{2\pi jkn}{N}} = Re_n\ +\ Im_n, \tag{2.26}$$

where j is an imaginary number, n designates the frequency increment, and N is the frame number in the sequence. Figure 2.14 shows the thermogram sequence and the phasegram sequence of temperature data for a pixel. By denoting the phase delay Φ as $\Phi = tan^{-1}(Im_n/Re_n)$, the absolute phase contrast $\Delta\Phi$ can be defined as :

$$\Delta\Phi = \Phi_d - \Phi_S, \tag{2.27}$$

where Φ_d is the phase of a defective pixel, and Φ_S is the mean phase value of a selected sound area. Phase contrast data is used to estimate the blind frequency which is the limiting frequency at which a defect at a particular depth shows enough phase contrast to be detected on the frequency spectra. The blind frequency has a certain relation with defect depth [20; 17; 3].

According to [19], deeper defects are visible at low frequencies while shallow defects are detected at higher frequencies. Figure 2.15 illustrates the relationship between the blind frequency

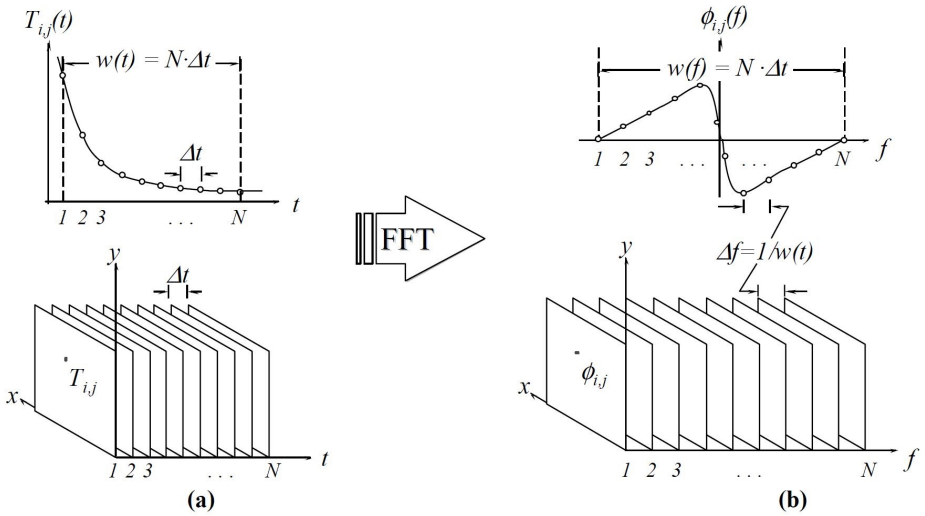

FIGURE 2.14 – (a) Thermogram sequence and temperature profile for a pixel, and (b) phasegram sequence after application of the FFT [17].

with defect depth. As shown in this figure, for each defect, the blind frequency can be determined when the limiting phase contrast is $\Delta\Phi = 0$. As discussed in [19], the equation for thermal diffusion length μ is given as $\mu = (\frac{\alpha}{\pi f})^{1/2}$ and, based on the phase delay definition ($\Phi = \frac{z}{\mu}$), the depth z changes inversely with the square root of the blind frequency :

$$z \propto f_b^{-1/2}. \tag{2.28}$$

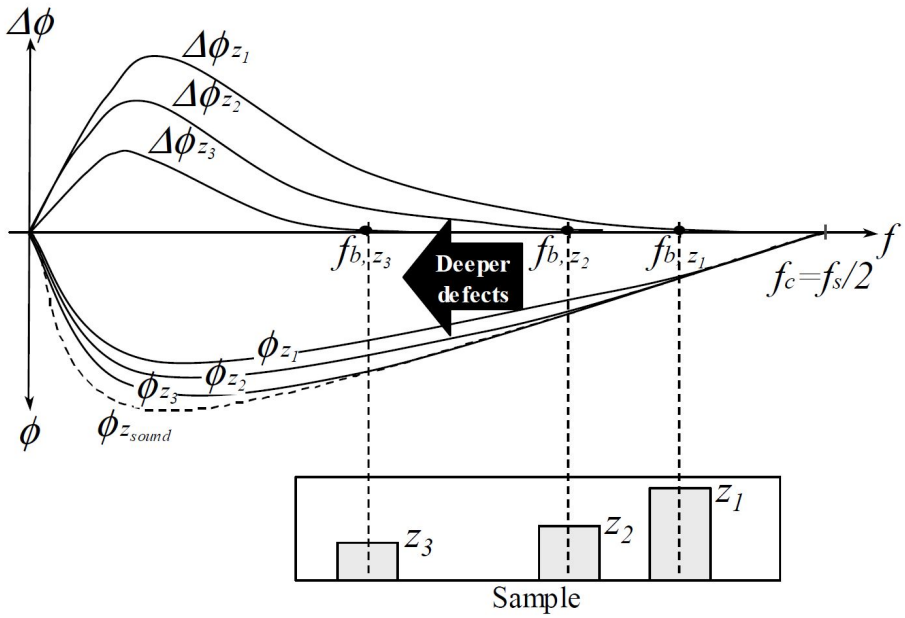

FIGURE 2.15 – Blind frequency relationship with defect depth [17].

Logarithmic Peak Second Derivative Method

In the Logarithmic Peak Second Derivative Method, it is proposed that the peak of the second derivative of the surface temperature on a logarithmic scale can be used to determine defect depth. The second derivative can be calculated directly from the temperature decay at each surface point and does not need a reference [33]. The first derivative of the measured temperature decay in equation (2.20) is calculated as :

$$\frac{d(ln\ T)}{d(ln\ t)} \ = \ \frac{t}{T}\ \frac{dT}{dt}, \tag{2.29}$$

and the second derivative is,

$$\frac{d^2(ln\ T)}{d(ln\ t)^2} \ = \ \frac{t}{T}\ \frac{dT}{dt} \ - \ \frac{t^2}{T^2}\ (\frac{dT}{dt})^2 \ + \ \frac{t^2}{T}\ \frac{d^2T}{dt^2}, \tag{2.30}$$

where, $\frac{dT}{dt} = -\frac{Q}{\rho CL}\ \frac{2\omega}{t}\ \sum_{n=1}^{\infty} n^2 e^{-n^2\omega}$ and $\frac{d^2T}{dt^2} = \frac{Q}{\rho CL}\ \frac{2\omega^2}{t^2}\ \sum_{n=1}^{\infty} n^4 e^{-n^2\omega}$. The temperature and logarithmic scale of temperature and first and second derivatives are plotted in figure 2.16. By solving equation (2.30), the peak second derivative is calculated as :

$$t_2 \ = \ \frac{\pi L^2}{\pi^2 \alpha}, \tag{2.31}$$

where, by compared to equation (2.25), it is observed that the second derivative peak time t_2 appears earlier than the peak slope time t_s, before it is affected by 3D conduction. So this method is more accurate than the temperature contrast methods described before. However, applying second order differentiation of the temperature leads to very noisy data. To solve it, Shepard et al. [33] use a polynomial function fitting of the temperature decay. In such case, fitting the curve on the exact location of the second derivative peak is very important [34].

Least Squares Fitting Method

The Least Squares Fitting Method is a method based on curve fitting which is less sensitive to noise [34]. Sun proposed to use a theoretical heat transfer model to fit the temporal thermography data at each surface point. He proposes a theoretical model for the time period $0 < t < t_b$ as :

$$T(t) \ \approx \ A[1 \ + \ 2\sum_{n=1}^{\infty} exp(-\frac{n^2\pi^2}{L^2}\ \alpha t)] \ - \ st, \tag{2.32}$$

where the slope s is determined by a linear fitting of the experimental data in the time period $t_a < t < t_b$. The time instants t_a and t_b which are illustrated in figure 2.16 are determined as :

$$t_a \ = \ \frac{L^2}{2\alpha},\ and,\ t_b \ = \ 3t_a, \tag{2.33}$$

where, the predicted thickness L is the defect depth if the surface point is on the defect area while, if the surface point is on the sound area without subsurface defect, L corresponds to the

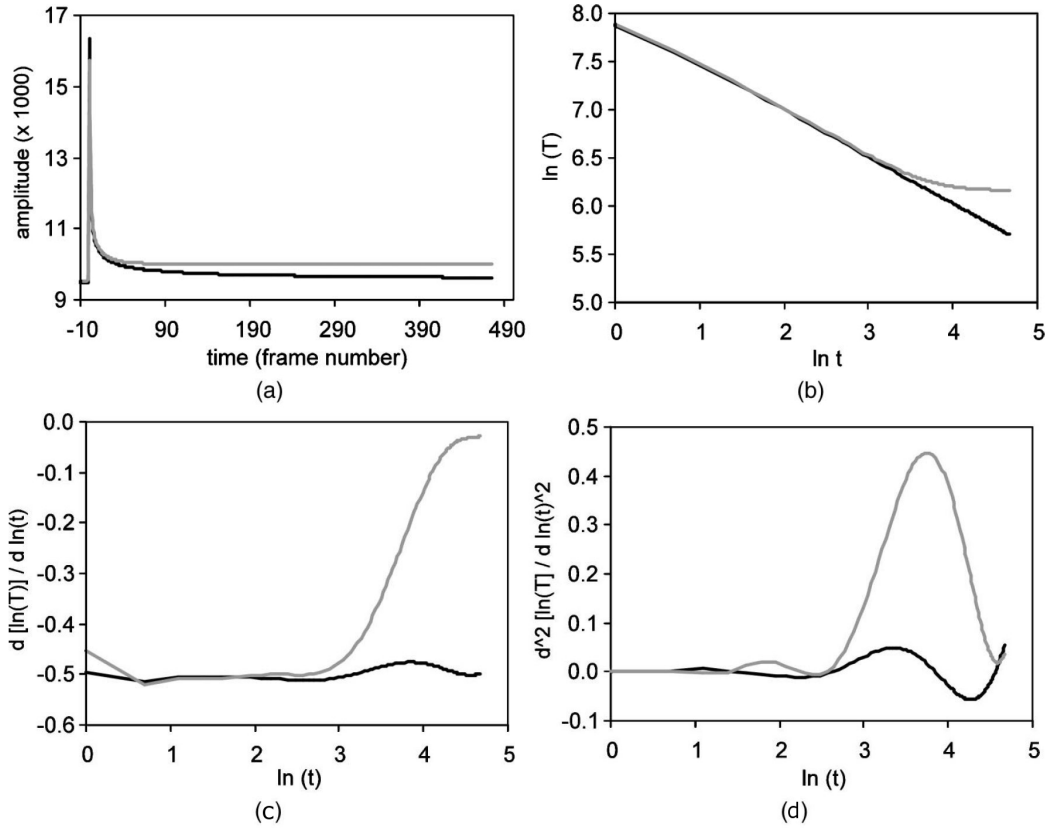

FIGURE 2.16 – Temperature curve and its first and second derivatives as functions of time on a logarithmic scale [33].

sample thickness. Recently Zeng et al. in [36] proposed a method to use the absolute peak slope time which is obtained by multiplying the original temperature decay with the square root of the corresponding time to predict the defect depth. They express the relationship between this time and defect depth as :

$$t_{APST} = \frac{L^2}{2\alpha}. \tag{2.34}$$

By comparing t_a in the equation (2.33) with t_{APST} in the equation (2.34), it is obvious that the absolute peak slope time is equal to t_a of the least squares fitting method.

Chapter 3

Description of the implemented approach for defect detection and depth estimation

Many methods have been used for NDT application in machine vision. Before processing the thermal images for defect detection, the sequence of images should be preprocessed to enhance their quality.

3.1 Image processing and data analysis

Because of imperfections in the acquisition system, such as limitations in the camera, the thermal images must be enhanced. Moreover, for better visualization of defects, the effect of noise should be reduced. In this way, the acquired infrared image sequences have been improved with some preprocessing steps which are discussed in the following.

3.1.1 Fixed Pattern Noise (FPN)

FPN (also called non-uniformity) is the spatial variation in pixel output values under uniform illumination due to device and interconnect parameter variations (mismatches) across the sensor.

This is a common problem in the focal plane arrays used as infrared detectors. The fixed pattern noise can be eliminated by capturing an image from a black body in a particular test configuration used for inspecting the test samples. This image is later subtracted from the infrared image sequence of the test sample to eliminate fixed pattern noise [26].

3.1.2 Bad pixels

A bad pixel is defined as an anomalous pixel in the image frame which has different behaviour from the rest of the pixel array. Bad pixels are either black or bright (white). These bad pixels do not provide any useful information [26], and numerous algorithms have been proposed to characterize and replace them. The most widely used algorithm is the nearest neighbourhood algorithm [18] where the signal of the bad pixel is replaced by the weighted average of its neighbouring pixels. Figure 3.1 presents some bad pixels of a thermal image at ambient temperature.

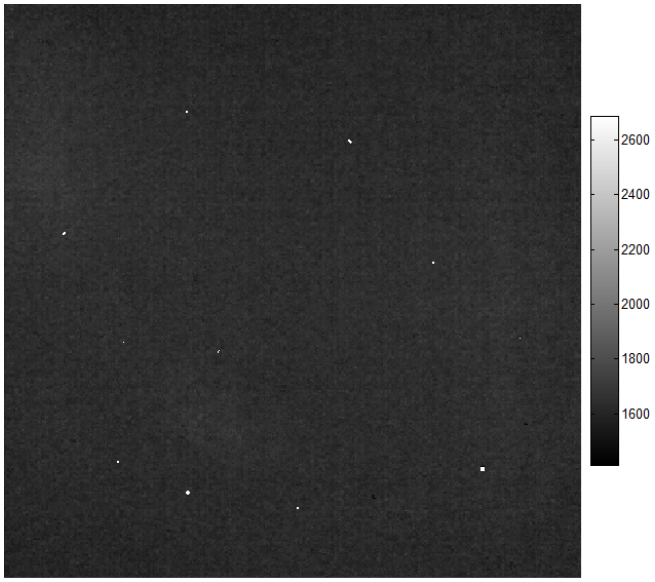

FIGURE 3.1 – Bad pixels in a thermal image.

3.1.3 Temperature Calibration

Temperature calibration is the procedure which consists of converting thermal units of IR camera into temperature, which is performed by a polynomial transformation function [15].

A reference heat source is selected whose temperature can be varied. We used a blackbody model Mikron M340 with a temperature range $-20.0°C$ to$150.0°C$. The IR camera captured these temperature variations as reference image sequences. The integration time of the camera has set to 1.5 ms. The reference images are averaged and a polynomial function is fitted in order to find the calibration curve. The temperature calibration curve is shown in figure 3.2. The obtained calibration can now be used for image acquisition.

3.1.4 Vignetting

Vignetting is a nonlinear effect of thermal images. Vignetting makes dark the image borders with respect to the center due to the limited exposure. A correction technique has been

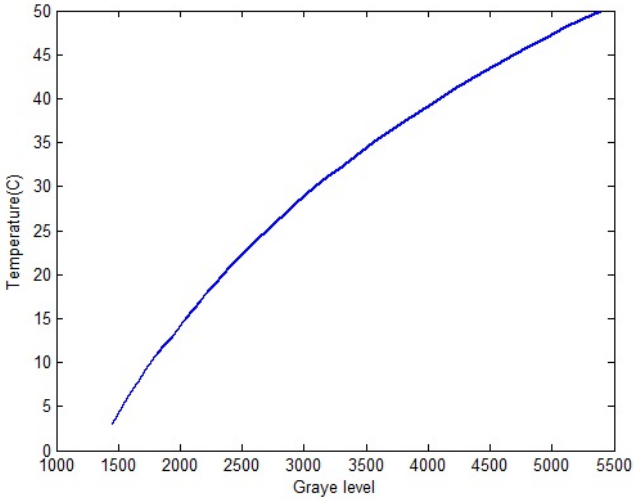

FIGURE 3.2 – The temperature calibration curve using blackbody.

proposed in [19], pp. 133.

3.1.5 Noise Filtering

Noise filtering is an important technique used on the acquired image sequences to improve the contrast. To modify the pixels, a mask or kernel is convolved with the image. Gaussian and Median filtering are common techniques. Gaussian filtering consist of applying a Gaussian kernel that is convolved to each point in the input array and produces the output array by replacing the pixel value by the result of the convolution.

The median filter passes through each pixel of the image and replaces its value with the median of its neighborhood. Robustness to outliers and preservation of the edges are the advantages of median filtering. Figure 3.3 (a) and (b) show the results before and after applying Gaussian and median filters.

3.1.6 Thermographic signal reconstruction

Thermographic signal reconstruction (TSR) [32] is an approach to increase the spatial and temporal resolution of image sequences. The author proposes to use a logarithmic scale on the temperature profiles in which the non-defective areas follow a linear decay while the defective areas diverge from this linear form. By considering the one-dimensional solution of the Fourier equation for the surface temperature of a semi-infinite sample stimulated by a Dirac delta function, the expression for the temperature T as a function of time t is :

$$T = \frac{Q}{e\sqrt{\pi t}}. \tag{3.1}$$

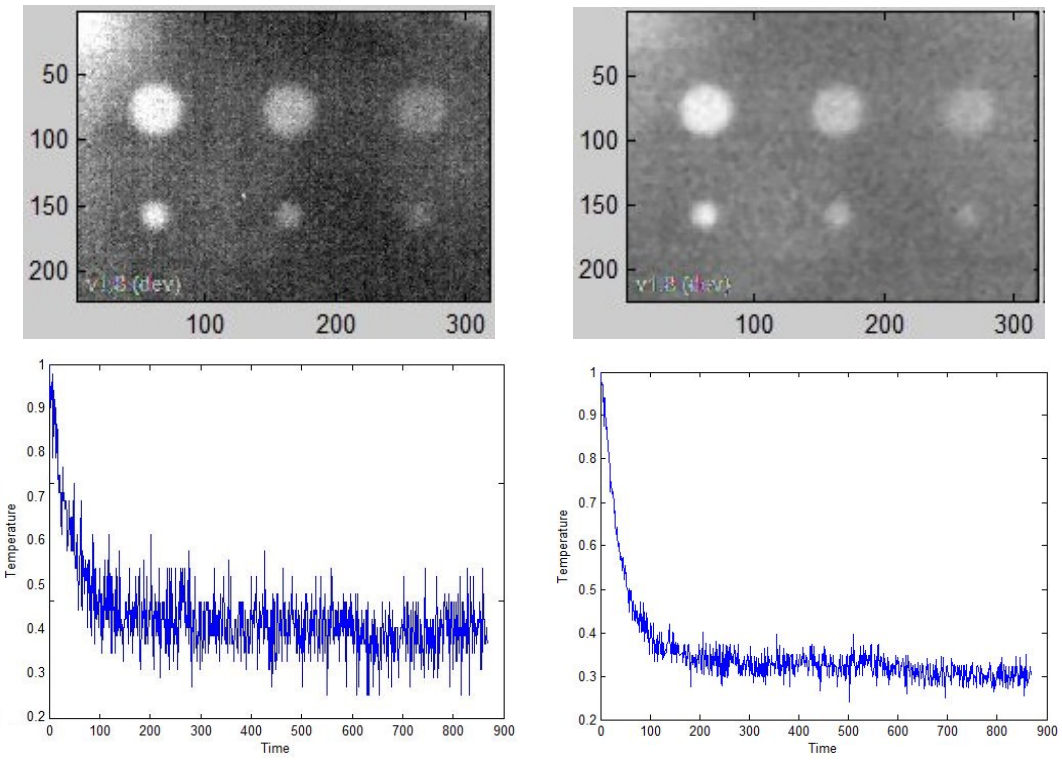

(a) (b)

FIGURE 3.3 – Aluminum specimen ; (a) raw thermogram after heat pulse (top) and temperature curve for a defect (bottom) ; (b) the thermogram using both Gaussian and median filtering (top) and temperature curve for the same defect (bottom).

The logarithmic form of equation 3.1 can be calculated as :

$$ln(T) = ln(\frac{Q}{e}) - \frac{1}{2}ln(\pi t), \tag{3.2}$$

where T is the temperature of the pixel or region of interest at time t, $Q(W/m^2)$ is the input energy per unit area and $e(Ws^{1/2}m^{-2}K^{-1})$ is the thermal effusivity. Equation 3.2 represents the "normal" behavior of a non-defective pixel as a straight-line decay on a logarithmic scale with slope $-1/2$. The offset term depends on the input energy (Q) and effusivity of the specimen (e). In practice, the relationship between temperature and time in experimental data for non-defective pixels is not projecting to linear because of a variety reasons such as poor camera calibration, reflection artifacts, etc. While the behavior of pixels corresponding to subsurface defects is far from this near-linear signature at a particular time.

The TSR technique is based on signal processing rather than image processing. Shepard proposes to use a low order polynomial function to approximate the logarithmic time dependence of a pixel which fits the thermographic data to a ρ-degree polynomial equation, where :

$$ln(T(t)) = a_0 + a_1 ln(t) + a_2 ln^2(t) + ... + a_\rho ln^\rho(t), \tag{3.3}$$

Figure 3.4 presents a temperature-time plot using a 5^{th} degree polynomial function for non-defect area and defect area. To avoid a "ringing" effect and obtain good fitting accuracy, ρ is usually set to 4 or 5. For example, the original data for a 5^{th}-degree polynomial can be modeled as :

$$T(t) = exp[a_0 + a_1 ln(t) + a_2 ln^2(t) + a_3 ln^3(t) + a_4 ln^4(t) + a_5 ln^5(t)]. \tag{3.4}$$

There are some advantages of using data modelled with equation 3.4 compared to raw thermal data such as : increase signal to noise, order of magnitude file size reduction, increased spatial resolution and the possibility of analytical processing by using the polynomial coefficients. In this way we propose to exploit the main advantage of TSR, which is significant noise reduction, in order to provide a considerable signal to noise improvement (chapter 4, section 4.2.1).

3.1.7 Principal component thermography

The Principal Component Thermography (PCT) is an image enhancement technique that is used to better detect subsurface defects and estimate their depth. PCT is mainly based on thermal contrast evaluation in time which is applied on the sequence of images [27]. The algorithm extracts the image features and reduces the undesirable signals by projecting original data onto a system of orthogonal components (known as Empirical Orthogonal Functions or EOF). By sorting the principal components in such way that the first EOF represents the most important characteristic variability of the data ; the second EOF contains the second

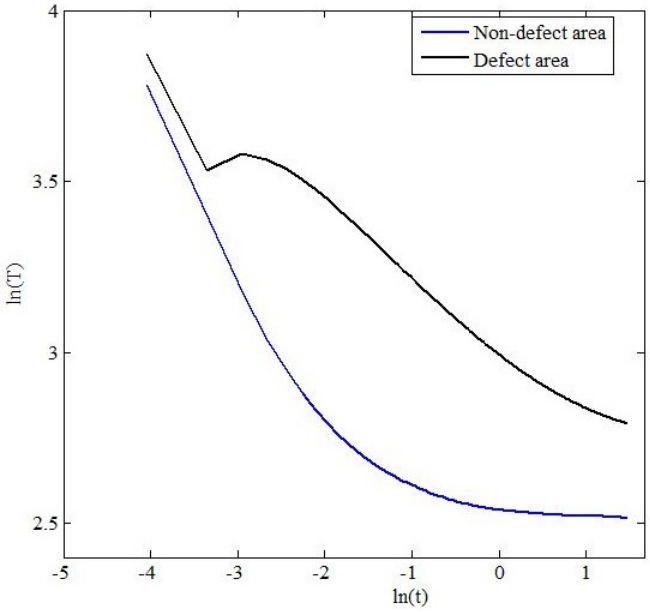

FIGURE 3.4 – Logarithmic temperature-time plot of a steel specimen.

most important variability, and so on. The original data can be adequately represented with only a few EOFs [13]. To minimize memory space and computation time, EOFs are usually obtained through singular value decomposition (SVD).

For example, an $M \times N$ matrix A ($M > N$) can be reduced by SVD as follows :

$$A = URV^T, \tag{3.5}$$

where U is $M \times N$ matrix, R is $N \times N$ matrix with singular values of matrix A in diagonal, V^T is the transpose of an $N \times N$ matrix. Let the time values correspond to columns and spatial values to rows in matrix A, so the columns of matrix U correspond to EOFs associated with data spatial values. The time values according to the coefficient in the principal component are presented by the rows of matrix V^T. As illustrated in figure 3.5, the thermal sequences can be comprised as two components : a spatially uniform transient decay and a spatially non uniform part which represents the thermal contrast. Gaussian noise affecting a signal-to-noise ratio (SNR) which is set to 10 was used with the data to have better measurements [27] :

$$\frac{\sigma_N}{C_{max}} = 0.1, \tag{3.6}$$

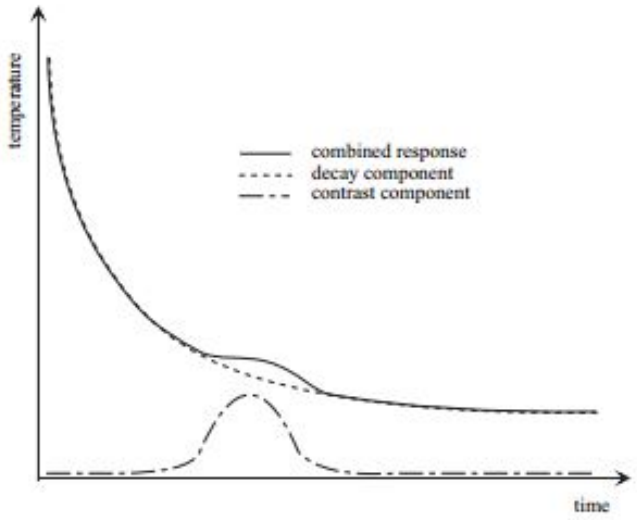

FIGURE 3.5 – Comparison of a thermal sequence's components [27].

where σ_N is the standard deviation of the noise and $C_{max} = max|T_{r=0,j} - T_{r=a,j}|$ is the peak spatial contrast in the frame sequence where $T_{r=0,j}$ is the temperature of pixel j, $T_{r=a,j}$ is the average temperature of the neighbourhood surrounding the pixel j. Figure 3.6 illustrates the response at peak contrast for an aluminum surface with a circular blind hole.

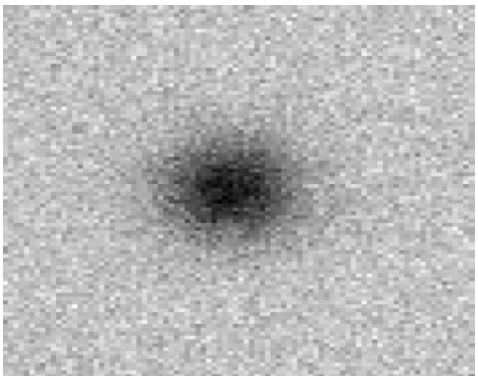

FIGURE 3.6 – Response at peak contrast [27].

Figure 3.7 illustrates a comparison of the distribution of peak contrast with the first four EOF's, to better figure out the PCT concept. The first EOF which corresponds to the largely homogeneous decay does not contain any significant information and it has a uniform shape, while the second EOF is strongly similar to the distribution of peak contrast and has a close relationship with the underlying structural flaw. In addition, the second EOF presents higher SNR in comparison to the peak contrast distribution.

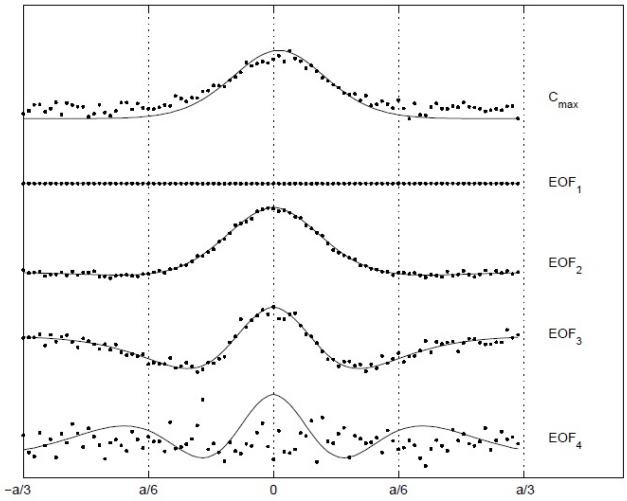

FIGURE 3.7 – Comparison of the distribution of peak contrast with the first four EOF's [27].

When the EOF levels increases the curve will have more extremums ; hence, the complexity of the shape will be increased. Increasing the EOF levels have a lower SNR and, therefore, the first EOFs in PCT have the most useful information except the first one.

PCT provides a framework for better observation of defect contrast and the characterisation of defect depth. This technique also improves signal-to-noise ratio compared to the raw data. The drawback of PCT is its extensive processing time and memory use [27].

3.1.8 Pulse Phase Thermography

Pulse Phase Thermography (PPT) is an image enhancement technique to generate better resolution of defect shape and depth estimation. Due to its reduced sensitivity to the optical and infrared properties of the material, it can detect the defects without knowing their position. The major idea of PPT is to extract and analyze the response of the specimen in the frequency domain. In other words, this technique uses the one-dimensional discrete Fourier transform (DFT) to transform the data from the time domain to frequency domain [20] :

$$F_n \;=\; \Delta t \sum_{k=0}^{N-1} T(k\Delta t) exp(\frac{-j2mk}{N}) = Re_n \;+\; jIm_n, \tag{3.7}$$

where j is the imaginary number, n designates the frequency increment ($n = 0, 1, \ldots N$), Δt is the sampling interval. Re and Im which are the real and the imaginary parts of the transform and are used to calculate the amplitude A and the phase ϕ of the Fourier component :

$$A_n \;=\; \sqrt{Re_n^2 \;+\; Im_n^2}\; and\; \phi_n \;=\; tan^{-1}(\frac{Im_n}{Re_n}). \tag{3.8}$$

Figure 3.8 presents results of applying equation 3.8 on each pixel of the thermogram sequence. Because of the anti-symmetric and redundancy in phase profile, only the positive part of the frequency spectra is considered.

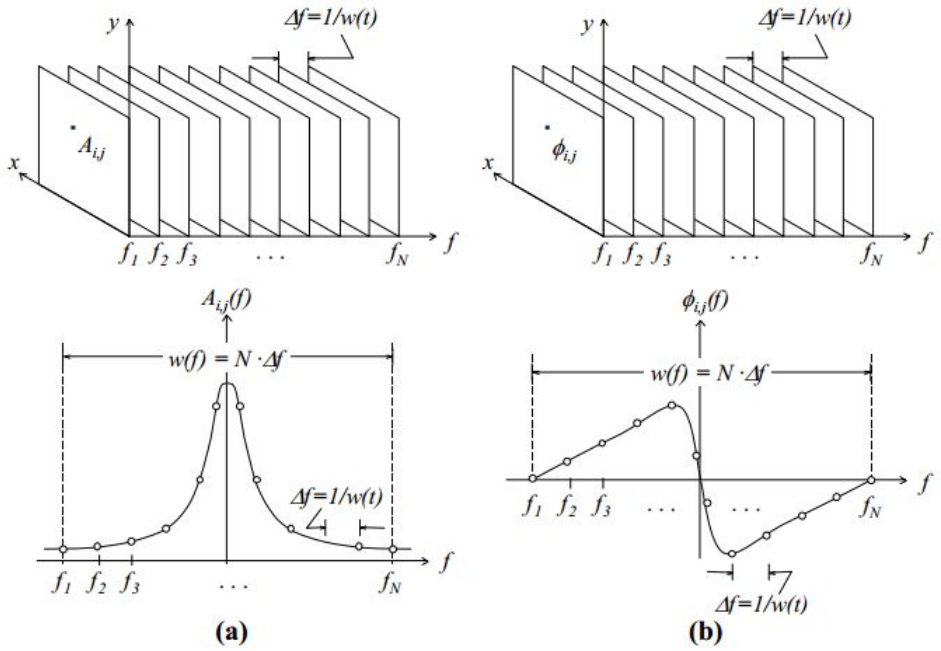

FIGURE 3.8 – (a) Amplitude A ; (b) phase ϕ of the transform (top) and their frequency spectra (bottom) for a non-defective pixel (i, j) [3].

Based on the observation on figure 3.8, low frequencies contain most of the energy while higher frequencies reveal a higher level of noise. Consequently only the first few frequencies are considered.

PPT provides better defect shape resolution compared to raw data since the phase profile is less sensitive to environmental reflections, emissivity variation, non-uniform heating and surface geometry and orientation.

As discussed before, due to heating imperfection, a well-known problem in active thermography is the heating noise which results as the recorded images showing some nonuniformity. Hence, noise filtering is an important pre-processing step to improve the contrast and achieve better estimation of size and depth of defects. Median and Gauss filters which are applied on image, and moving average filter which is applied on the time sequence, are useful filters to eliminate the noise in pulsed thermography data. Defect enhancement techniques can be also used to improve the inspection process, such as thermographic signal reconstruction (TSR), pulse phase thermography (PPT), and principal component thermography (PCT). We propose to use a combination of these powerful inspection approaches to enable the detection of both small and large defects, while compensate for the drawbacks of each method taken separately. Experimental results are provided in chapter 4.

Once thermal images have been preprocessed, all defects should be visible with good contrast and it is then possible to perform defect detection and depth estimation.

3.2 Defect detection

Automatic defect detection is an important approach in image segmentation. Several methods have been proposed for detecting the subsurface defect. Thresholding is a common segmentation technique in machine vision application because of the simplicity and speed. The objective of automatic thresholding is to select a threshold value from the histogram of the intensity of image in order to distinguish the defect area from the sound area. In the following the advantages and disadvantages of the defect detection methods which are mentioned in chapter 2 will be explained.

Otsu's threshold selection method [24] is simple and easy to implement and provides good results when the histogram of the image is close to a bimodal distribution. The drawback of this technique is that it fails when the diversity of object variance and background variance is large or when the histogram is unimodal or close to unimodal.

The Valley-emphasis method [23] which is a revised version of Otsu's method compensates for the drawback of Otsu's method by selecting optimal threshold values for both bimodal and unimodal distributions. This method is fast and easy to realize but it does not work when the variance of the object is significantly different from the variance of the background. This

occurs when the object is very small compared to the background.

The Active contour method [4] is based on techniques of curve evaluation instead of thresholding. Active contour is an energy minimizing paradigm which moves a curve towards its interior normal around the object. The object can be detected by stopping the evolving curve on its boundary. The major problem of this method is finding the contour to separate the object from the background, such that the intensity variation inside the contour becomes minimal and is maximal outside the contour. Moreover, the dependency of this method to different control parameters and degradation of target image due to noise presence can be mentioned as reasons for failure of the algorithm.

Despite the simplicity of Heriansyah's method [12], it is not able to extract the exact shape of defects since the algorithm is based on the local intensity operation in which the bright areas will be brighter and the dark areas are darker. The authors proposed to use a dilation operation to overcome the shrinking effect of edges. However, this method can segment both hot and cold defects on thermal images acquired from petrochemical plants, it fails when the temperature variation is small.

Based on our experimental results, we have used the Neighborhood Valley-emphasis method [7] to detect defects with different sizes. As discussed in chapter 2, this method which is a modification of the Valley-emphasis method improves the segmentation quality by taking into account the neighborhood information to also detect small objects. In chapter 4 the experimental results are provided and we will compare the performance of the Neighborhood Valley-emphasis method with other abovementioned defect detection methods.

According to our experiments, the result of Hamadani's method is more acceptable than the other approaches. However, it is not an automatic method and needs the user intervention. So, it can be considered as a ground truth technique. The experimental results on this technique are provided in the next chapter.

3.3 Depth estimation

As mentioned before, several approaches are proposed to estimate the depth of defects. In chapter 2, we investigated Peak Temperature Contrast, Peak Temperature Contrast Slope, Pulsed Phased Thermography, Logarithmic Peak Second Derivative, Least-Squares Fitting, and Absolute Peak Slope Time methods. According to the theoretical investigation presented in [34], the Peak Temperature Contrast approach is unable to detect the depth of defects. The Peak Temperature Contrast Slope approach is able to determine the accurate depth of the defects however it cannot be used to predict the depth of defects that are comparable to the thickness of the specimen. Moreover, the Logarithmic Peak Second Derivative technique provides the same detection accuracy as the Peak Temperature Contrast Slope approach [34].

Despite the accurate depth estimation achieved by the Least-Squares Fitting method for ceramic composite materials, it is not appropriate for high thermal conductivity materials, such as aluminum and steel specimens.

The major idea of the Pulsed Phased Thermography algorithm is to extract and analyze the response of the specimen in the frequency domain in order to detect the depth. Since, low frequencies contain most of the energy and higher frequencies reveal a higher level of noise, only the first few frequencies are considered in this approach. However, the defects at the frequencies higher than the blind frequency are not detectable so the shallow defects cannot be predicted well [16].

The Absolute Peak Slope Time approach [36] does not need a reference for depth prediction and provides good results for high thermal conductivity materials. We propose to use this algorithm to automatically estimate the depth. This method is relatively simple to implement. Zeng et al. in [36] demonstrated that the square of the defect depth has a linear relation with the absolute peak slope time (t_{APST}) which is obtained by multiplying the temperature curve with the square root of the corresponding time.

When there is any subsurface defect, equation 3.1 can be written [36] :

$$\Delta T(t) \;=\; \frac{Q}{e\sqrt{\pi t}}[1 \;+\; 2\sum_{n=1}^{\infty} exp(\frac{-n^2L^2}{\alpha t})], \tag{3.9}$$

where L is the defect depth and $\alpha(m^2/s)$ is the thermal diffusivity. In order to obtain a specific characteristic time without a reference curve, both side of the equation 3.9 are firstly multiplied with $\sqrt{t}$ and a new time-dependent function can be defined as [36] :

$$f(t) \;=\; \Delta T(t).\sqrt(t) \;=\; \frac{Q}{e\sqrt{\pi}}[1 \;+\; 2\sum_{n=1}^{\infty} exp(\frac{-n^2L^2}{\alpha t})]. \tag{3.10}$$

Figure 3.9 illustrates the temperature curve T and f curve of an aluminum sample. As can be observed from this figure, the temperature curve does not have a peak, while multiplying the temperature curve with $\sqrt{t}$ provides a peak slope time for f curve. In the following, the first derivative of equation 3.10 can be calculated as :

$$f'(t) \;=\; \frac{2Q}{e\sqrt{\pi}} \sum_{n=1}^{\infty} exp(\frac{-n^2L^2}{\alpha t}).\frac{n^2L^2}{\alpha t^2}. \tag{3.11}$$

For the same aluminum sample, the f' curve, the derivative of the f curve, is presented in figure 3.10. The figure shows the result of solving equation 3.11 for L for simulated curves and for actual results on captured video from the sample. As it is shown in this figure, there is a peak for each defect. In order to find the absolute peaks on the f' curves, we need to find

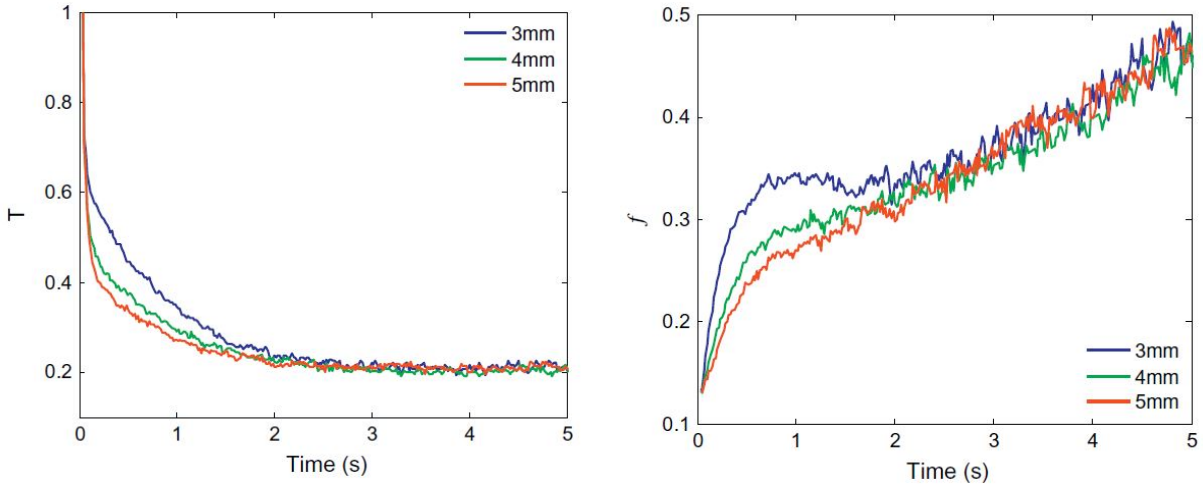

(a) (b)

FIGURE 3.9 – (a) The temperature curve, (b) The f curve of aluminum sample [36].

derivative of the f' and then find where it is equal to zero. f'' is presented as follows :

$$f''(t) = \frac{2Q}{e\sqrt{\pi}} \sum_{n=1}^{\infty} exp(\frac{-n^2L^2}{\alpha t}).\frac{n^2L^2}{\alpha t^3}.(\frac{n^2L^2}{\alpha t} - 2). \tag{3.12}$$

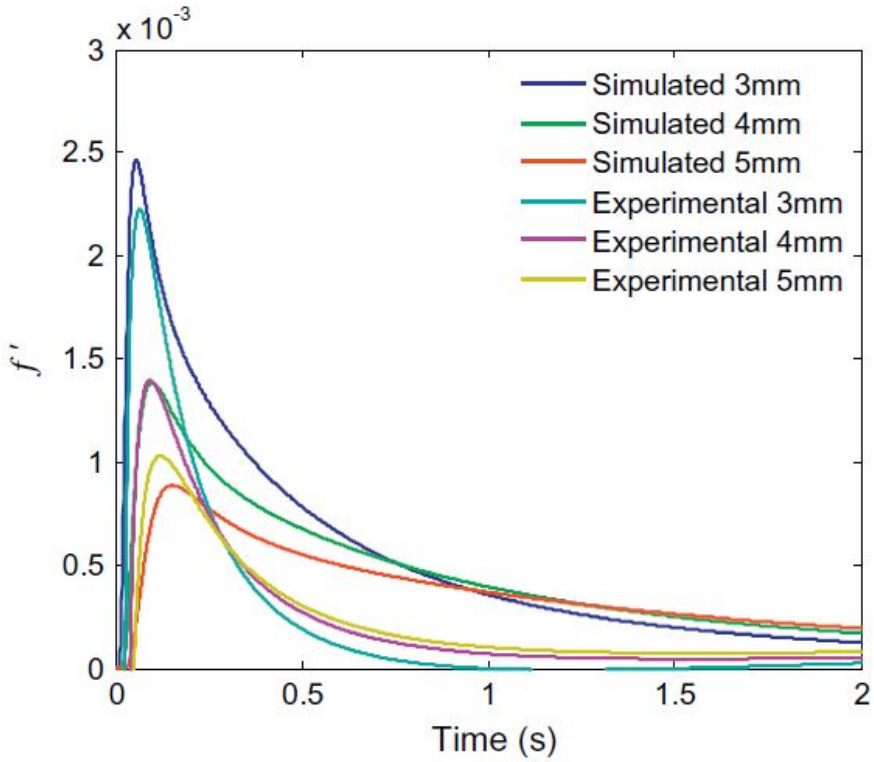

FIGURE 3.10 – The experimental and simulated f' curves of aluminum sample [36].

Therefore, the absolute peak slope time (t_{APST}) can be obtained by setting the equation 3.12 to zero [36] :

$$t_{APST} = \frac{L^2}{2\alpha}. \tag{3.13}$$

As can be observed, the peak values decrease when the depth of the defect increases and, according to equation 3.13, the absolute peak slope time has a linear relationship with the square of the defect depth.

Since this method is simple, fast and does not need a temperature reference, it can be easily automated. We used this method for estimating the depth of defects. The experimental results are provided in chapter 4.

Chapter 4

Experimental results and discussion

In this chapter, we present the experimental results on defect detection and depth estimation results.

4.1 Pulsed thermography setup

Data acquisition and processing in pulse thermography consists of four components : an energy source, the sample of tested material, an infrared camera and a data acquisition and control computer. As presented in figure 4.1, the specimen (1) is stimulated with a thermal pulse (2), the IR camera (3) records the temporal evolution of the thermal map of the surface and the recorded sequences are processed by the control system. In all experiments presented in this chapter, the optical simulation is applied using two Balcar FX 60 flashes with a pulse duration of 5 ms and producing energy equal to 6.4 kJ per flash. Infrared images are acquired using a Phoenix camera, which produces thermal images of 640×512 pixels and the camera's integration time is set to 1.5 ms. The FLIR Phoenix camera operates in 3 to 5 µm wavelength range with the noise equivalent temperature difference (NETD) as 25 mK.

Windowing capability, snapshot integration, variable integration times, high frame rate and automatic gain control are other features that contribute to improve camera performance. The quick guide of the Phoenix camera which is presented in appendix B illustrates a guideline for starting to work with the FLIR systems Phoenix camera with Rtools software. This software is used to acquire, process, analyze, and save the obtained sequences on the PC, as well as to select the acquisition settings (e.g. time of acquisition, storage type), display options (e.g. colour palette, display rate) and file name. We have implemented the inspection, segmentation and depth estimation approaches using Matlab 8.0.0.783.The Matlab program was ran on a PC with the following specifications : (R) Core(TM) i7, 3.20 GHz, and 16GB of RAM.

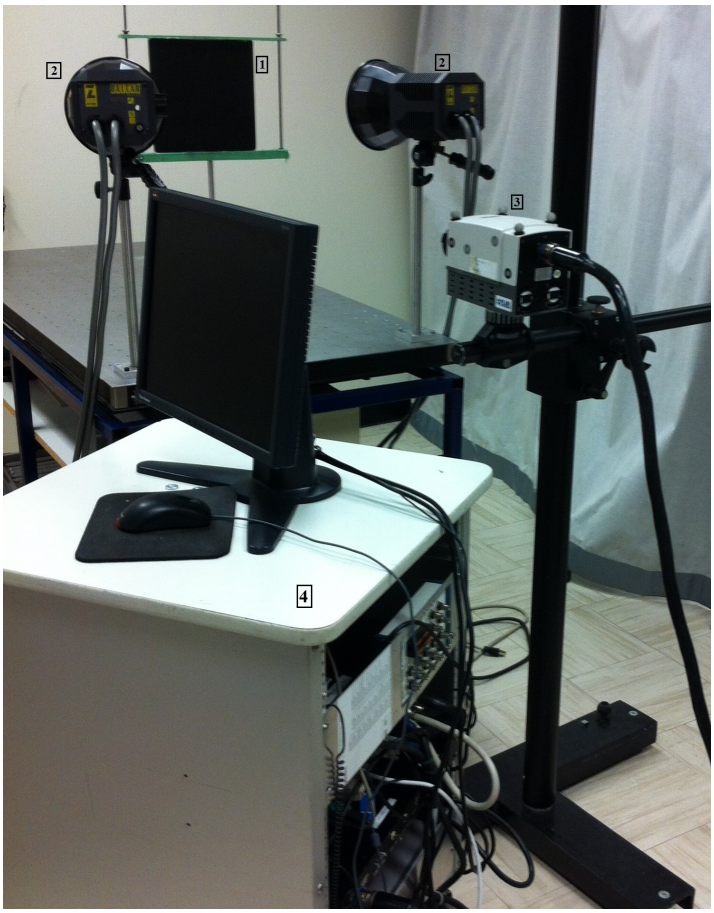

FIGURE 4.1 – The experimental setup ; (1) Sample of tested material, (2) the energy source (two flash lamps), (3) the infrared camera and, (4) the control system.

4.2 Data analysis

In the experiments, the IR camera captured a cold image before shooting the flashes. At this time, there is no difference between the temperature of sound area and the temperature of defect area. This image can be used to be subtracted from the thermogram sequence in order to reduce or eliminate the non-uniformity or fixed pattern noise (see FPN, section 3.1.1 in chapter 3). After shooting the flashes, a short time interval "saturated time" occurs. Depending on the sampling frequency, the saturated time for low conductivity materials is greater than for high conductivity materials.

Figure 4.2 illustrates the thermograms sequence for a single pixel after saturated time for an aluminum specimen with 1 mm defect depth. Once the heat pulse has reached the surface of the specimen the temperature profiles of the defect area and the sound area decrease with the same ratio. However, the temperature curve of the defect area behaves differently when the heat pulse moves through the specimen and reaches the defect. This different behavior is due to the difference in thermal effusivity between the specimen and the air. The thermal

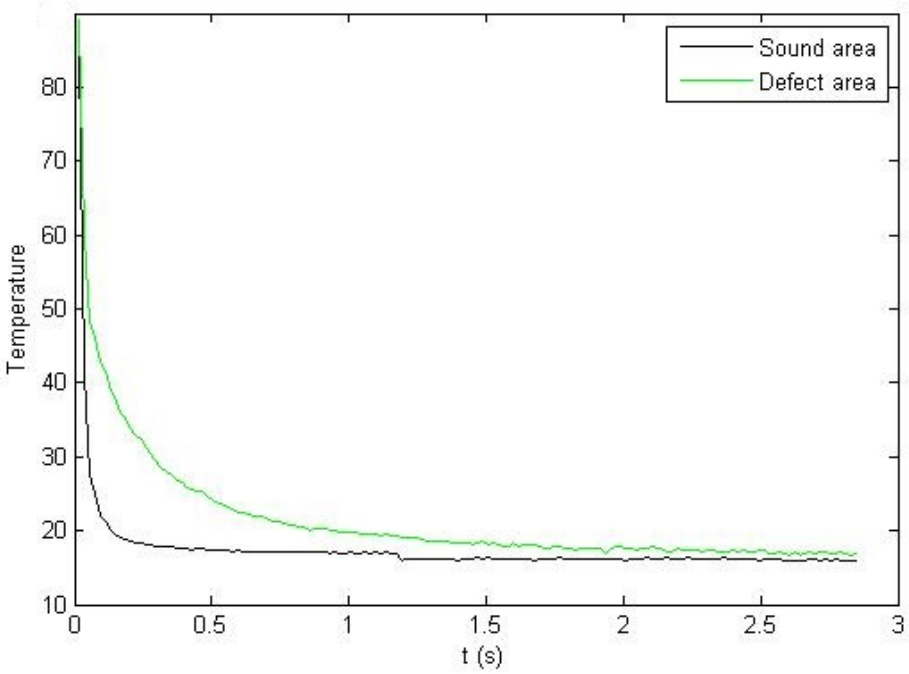

FIGURE 4.2 – Thermograms sequence after saturated time (sound area and defect area) for specimen ALU016 with 1 mm defect depth.

effusivity of the aluminum is greater than air effusivity ($e_{Aluminum} = 24047\ Ws^{1/2}/m^2K^1$ and $e_{air} = 5\ Ws^{1/2}/m^2K^1$, on the other hand, the heat pulse in the defect area faces with lower effusivity (air).

Therefore, according to equation 3.1, the temperature at the defect area becomes greater than the temperature at sound area. This behavior can be observed clearly in the temperature profile in figure 4.2. The temperature difference between the defect area and the sound area has a relation with the depth of the defect. Consequently, shallow defects appear earlier than deeper defects. Since the heat pulse travels less through the specimen to reach the defect when the defect is shallow. On the contrary, the heat pulse needs more time to propagate through the specimen and reach the defect for deeper defects.

As mentioned before, the preprocessing step is a very important step in pulsed thermography. The problems related to the acquisition procedure such as FPN and bad pixels are solved by the methods explained in chapter 3. Also, to improve the contrast of the target images a Gaussian filter with standard deviation 0.5 was applied to the images of sequences.

Generally, a filtering preprocessing step is necessary to suppress noise. Median filtering is a common technique to improve the contrast of images. It is a nonlinear filtering technique which attempts to remove the noise while preserving the edges. Morphological filters are also nonlinear filters for image enhancement. Opening and closing are two important operators,

which are both derived from the fundamental operations of erosion and dilation. The basic effect of an opening is similar to erosion in that it tends to remove some of the foreground (bright) pixels from the edges of regions. However, closing is similar to dilation in that it tends to enlarge the boundaries of foreground (bright) regions in an image.

We applied two denoising techniques, i.e. median and opening-closing, on the tested materials. The results of these filtering methods for ALU016, PLEXI006 and ACIER002 specimens (see Appendix A) are presented in figure 4.3. The window size of the median filter was set to 5×5 pixels and a disk-shaped structuring element with radius 2 was considered in the opening-closing operation.

As we can observe, nonlinear filtering approaches improve the visualization of defects. However, the results of median filtering are more acceptable than opening-closing. Due to the erosion and dilation operations, the original shape of defects cannot be preserved, so it is preferable to use median filtering as the denoising step.

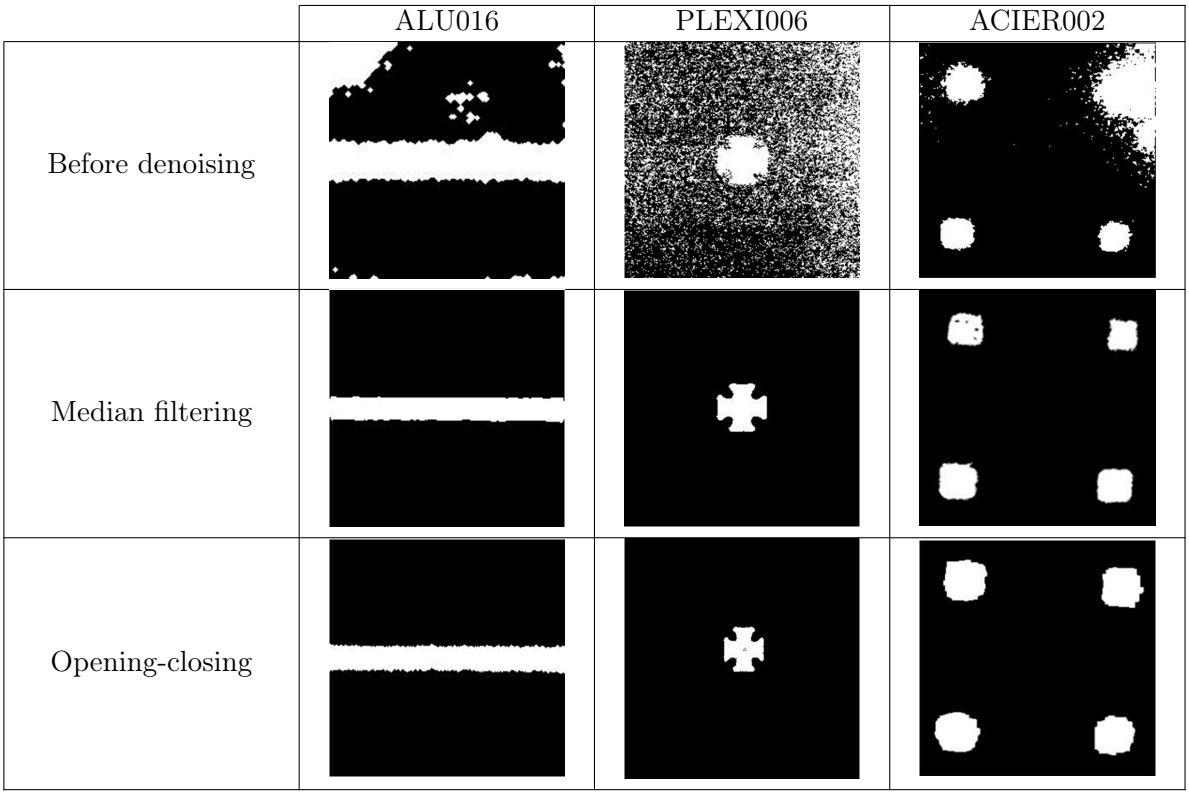

FIGURE 4.3 – Comparative results of image denoising methods for aluminum (ALU016), plexiglas (PLEXI006) and steel (ACIER002) specimens. Hamadani's method is used to segment the thermograms.

4.2.1 Thermographic signal reconstruction

As mentioned in section 3.1.6, Thermographic signal reconstruction (TSR) [32] is a signal processing approach which increases the spatial and temporal resolution of image sequences. Generally, a logarithmic scale of temperature profiles is used in which the non-defective areas show a linear behavior while defective areas diverge from this linear form. The algorithm fits a p-degree polynomial equation to the thermographic data to approximate the logarithmic time dependence of a pixel by a low order polynomial function.

Figure 4.4 illustrates a 3- and 5-degree polynomial equation of PLEXI006 and ACIER002 specimens. As we can observe, the main advantage of TSR is to reduce the noise significantly and increase the signal to noise ratio. Moreover, the 3-degree estimation provides a large error in initial values, the primary value being at time zero ; the obtained curves in figure 4.4, (c)-(d), are far from the real ones in the same figure, part (a) and (b). So it cannot describe the data as well as the 5-degree polynomial approximation which is presented in part (e) and (f). Normally, in order to have a good fitting accuracy and to avoid a ringing effect, p can be set to 4 or 5.

In addition, TSR can considerably reduce data storage requirements since to reconstruct the thermal profiles for each pixel, only the coefficients of the polynomial function are needed. For example, a thermogram sequence of ACIER002 consists of 600 frames of 640×512 pixels. According to equation 3.4 of chapter 3, the temperature profile can be modeled by the six coefficients of a 5-degree polynomial of TSR, which reduces the original thermogram to $640 \times 512 \times 6$. Therefore, we used TSR as a denoising approach in our experiments.

4.2.2 Principal component thermography

A better distinction between the defect and the sound area can be achieved by PCT. By projecting the original data onto the empirical orthogonal functions (EOF), image features can be extracted and undesirable signals can be reduced. Figure 4.5 represents the first four EOFs of ALU016 and ACIER002.

By comparing this figure with figure 3.8 of chapter 3, we can conclude that the first EOF contains no significant information, while the third next EOFs provide more useful information of the structural flaws. So, we can represent the original data with the first few EOFs.

4.2.3 Pulse phase thermography

As theoretically discussed in Section 3.1.8 of chapter 3, a better resolution of defect shapes can be obtained using PPT. Figure 4.6 presents the phase thermogram of ALU1983 at frequencies 0.27, 0.55 and 0.83 Hz. We can observe that low frequencies contain most of the energy while higher frequencies reveal a higher level of noise, so only the first few frequencies can be considered.

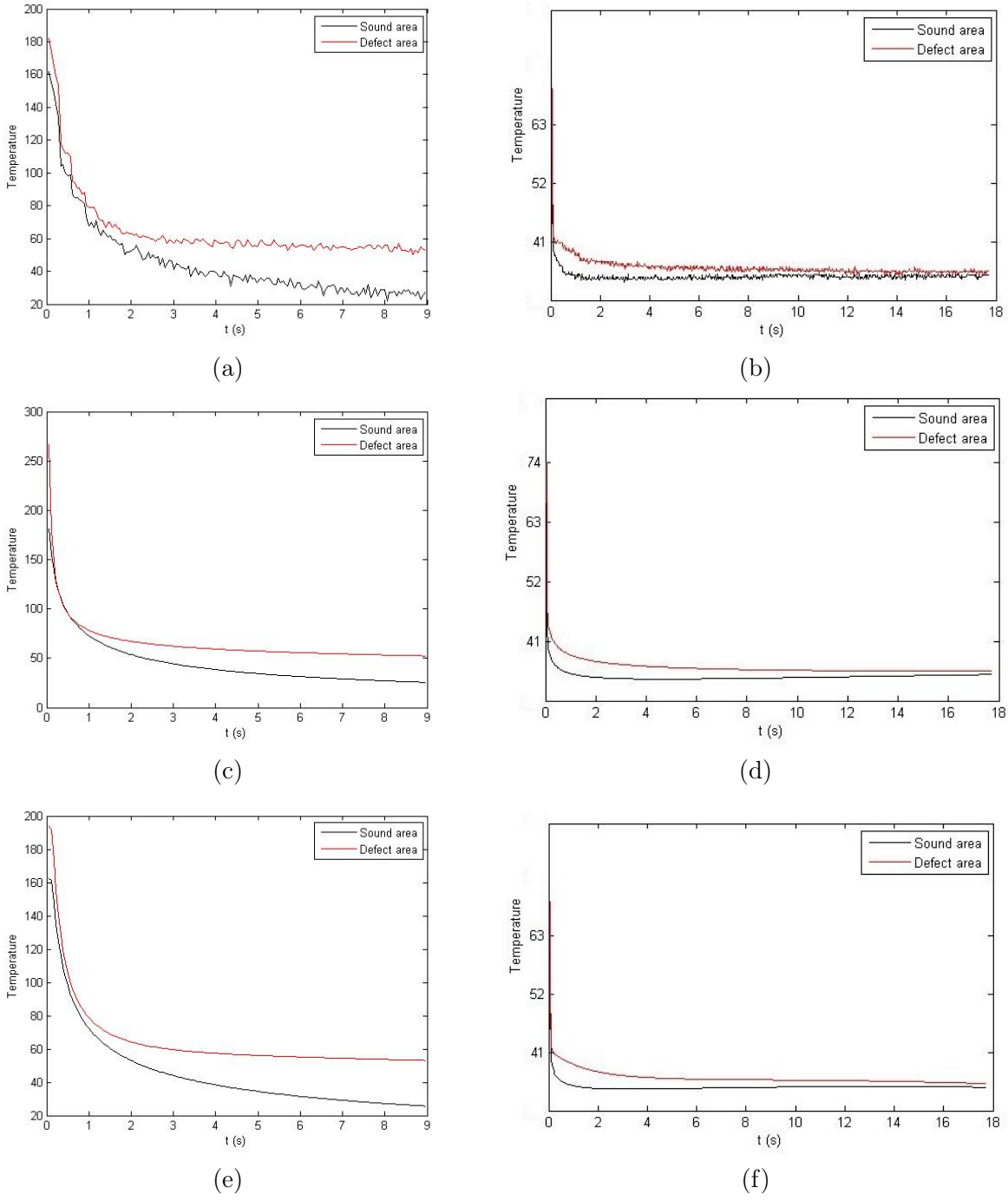

FIGURE 4.4 – Curve temperature profile of defect and sound areas for (a) PLEXI006, (b) ACIER002, (c)-(d) TSR with 3-degree polynomial, (e)-(f) TSR with 5-degree polynomial.

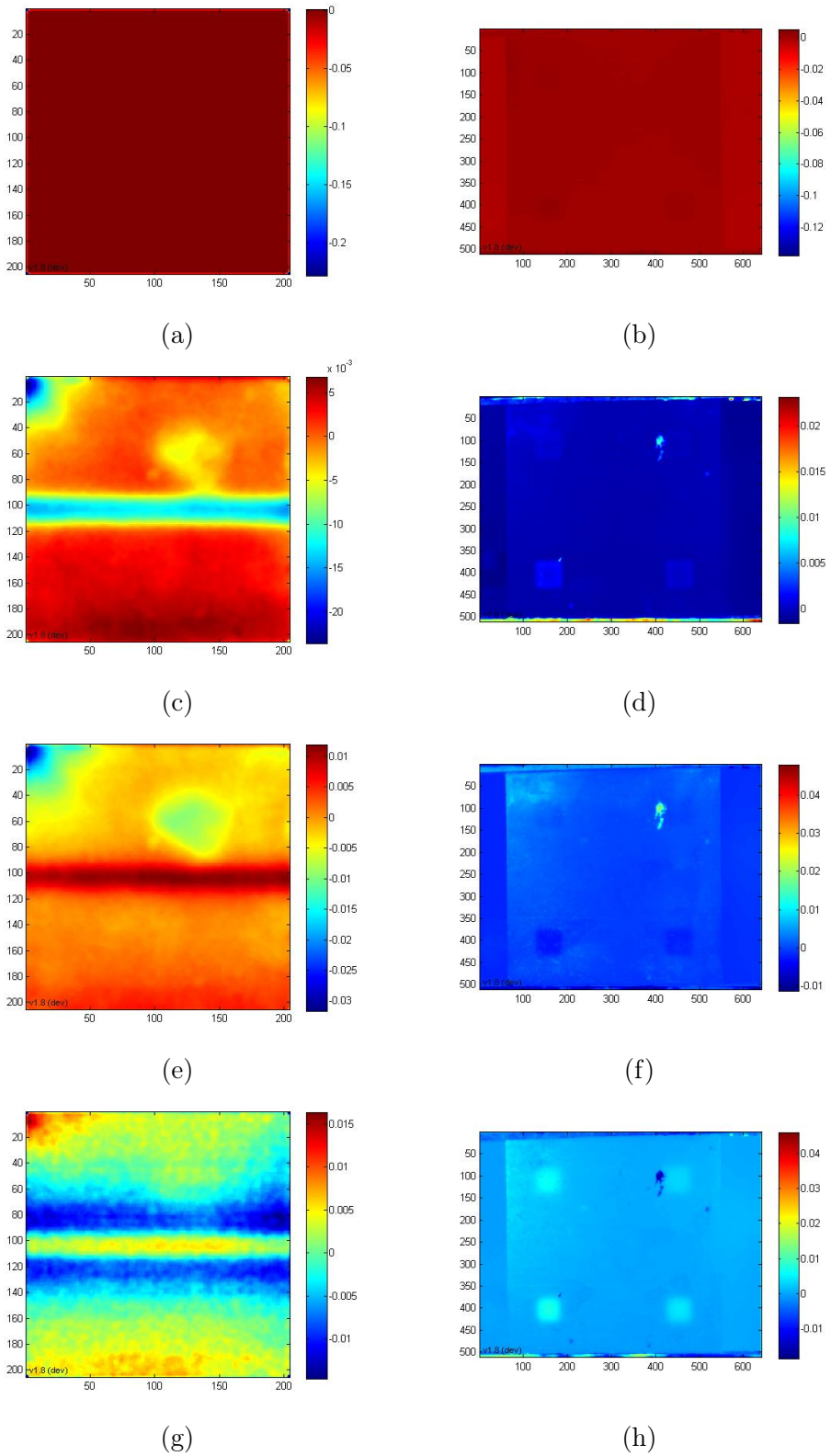

FIGURE 4.5 – The thermograms corresponding to the first four EOF of PCT for ALU016 and ACIER002.

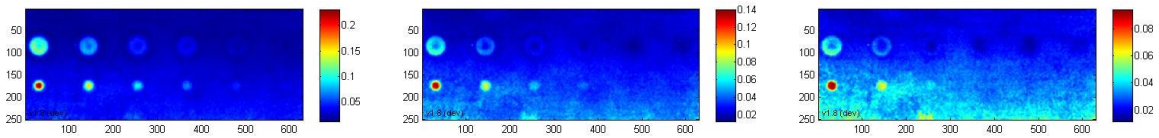

(a) (b) (c)

FIGURE 4.6 – The first three frequencies of the phase thermograms on the specimen ALU1983 : (a) frequency = 0.27 Hz, (b) frequency = 0.55 Hz, (c) frequency = 0.83 Hz.

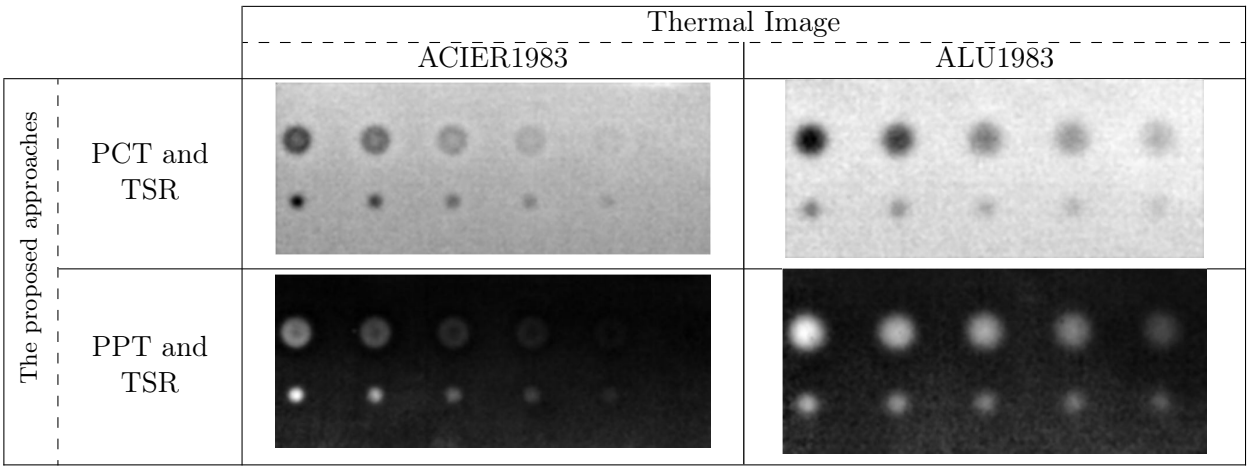

FIGURE 4.7 – Detecting different size of defects.

4.2.4 Combination of TSR with PPT and PCT techniques

Based on the results of the above experiments, we propose to use a combination of TSR with PPT and PCT approaches to detect both small and large defects. We used the TSR approach to suppress noise in the time domain. A polynomial function of degree 5 is fitted on the temperature profiles. The PPT and PCT approaches are implemented as the inspection methods in the next step. Taking the advantages of these algorithms for detecting defects and using TSR for denoising in addition to detection, provide the opportunity to compensate the drawbacks of each technique and produce good results.

Figure 4.7 illustrates the results of combining TSR with PPC and PCT methods for ALU1983 and ACIER1983 (see Appendix A). We can observe that small defects are best detected by PPT and TSR, while larger defects are better detected by PCT and TSR. Overall, the results of PPT and TSR are superior since they detect more defects and estimate sizes close to the value of the real life specimen. So, it is suggested to the user to select the appropriate approach based on the inspection application.

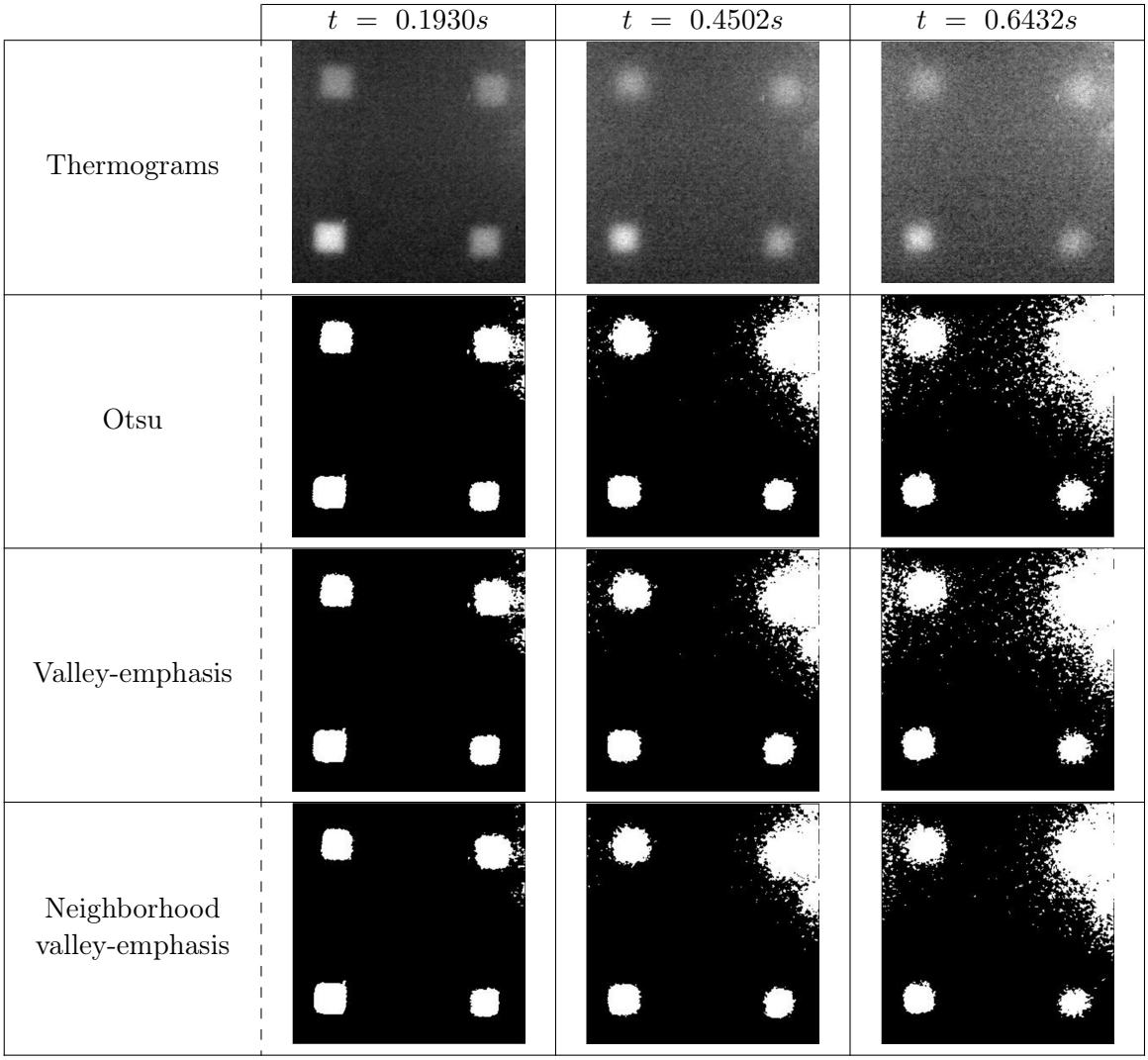

FIGURE 4.8 – Detection results of Otsu [24], Valley-emphasis [23], and Neighborhood valley-emphasis [7] for ACIER002 specimen.

4.3 Defect detection

In the previous sections, the quality of acquired thermograms is improved through the use of denoising and enhancement approaches. In order to compare the enhanced images, we applied several segmentation techniques : Otsu's method [24], valley-emphasis approach [23], neighborhood valley-emphasis technique [7], Heriansyah's method [12], active contour algorithm [4] and a thermal segmentation approach, Hamadani's method [10]. Figure 4.8 and 4.9 illustrate the results of these segmentation methods at three time intervals 0.1930, 0.4502, 0.6432 (s) for ACIER002 specimen.

As we can observe, Heriansyah's method [12] is unable to extract the exact shape of defects. It fails because of the small temperature variation of our specimen. Moreover, the active contour

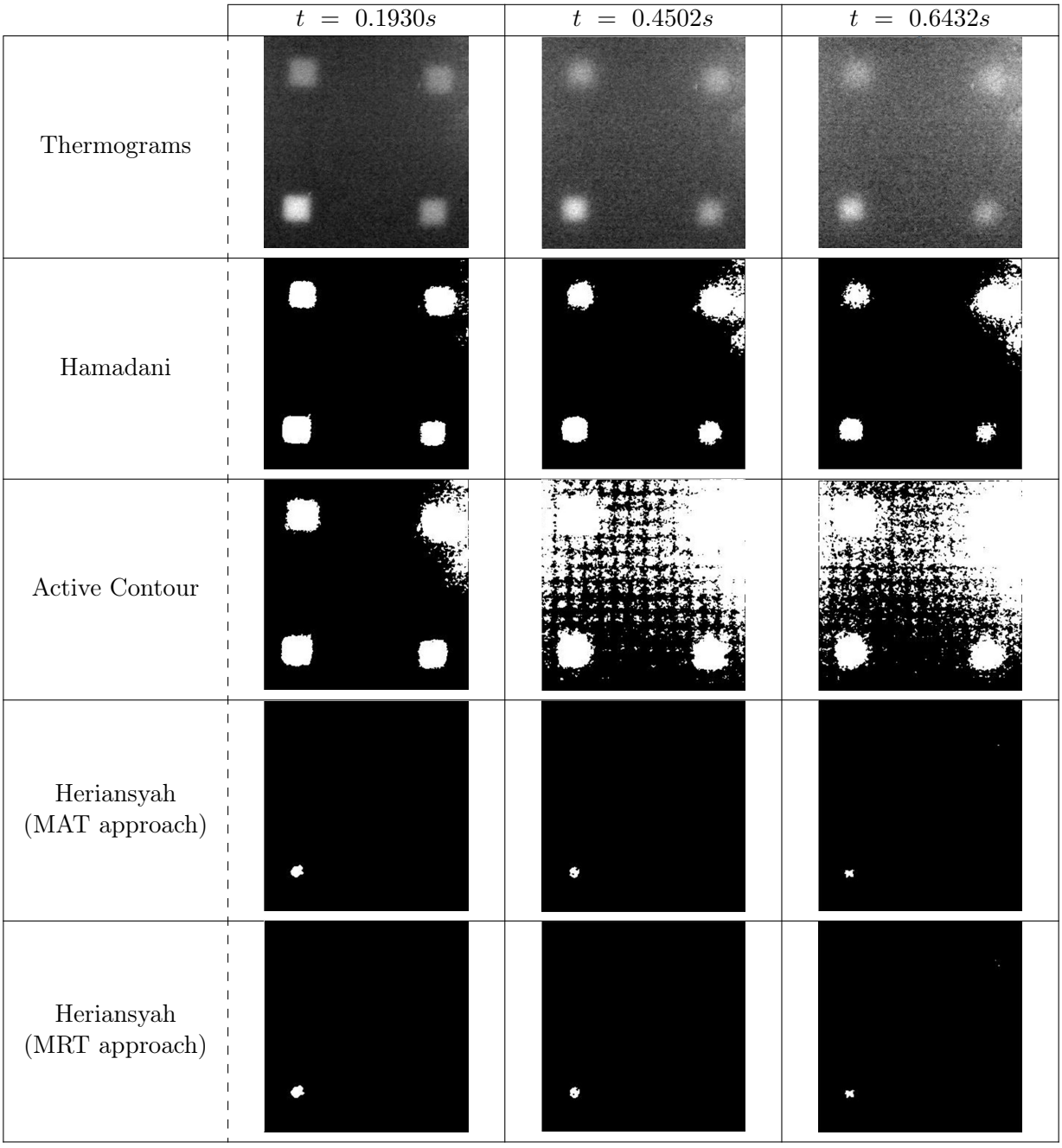

FIGURE 4.9 – Detection results of Hamadani [10], Active contour [4], and Heriansyah [12] for ACIER002 specimen.

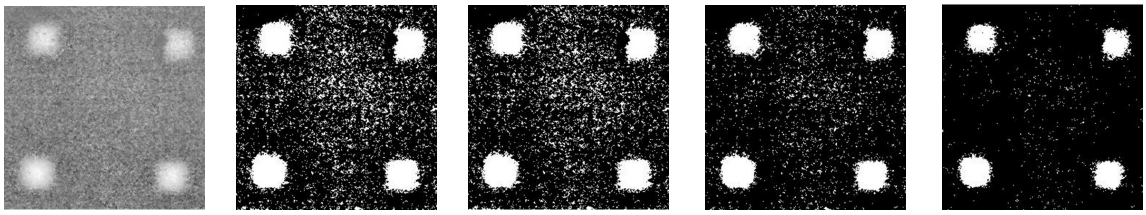

Thermal image | Otsu's method [24] | Valley-emphasis method [23] | Neighborhood valley -emphasis method [7] | Hamadani's method [10]

FIGURE 4.10 – Performance comparison of defect detection methods for ACIER002 specimen.

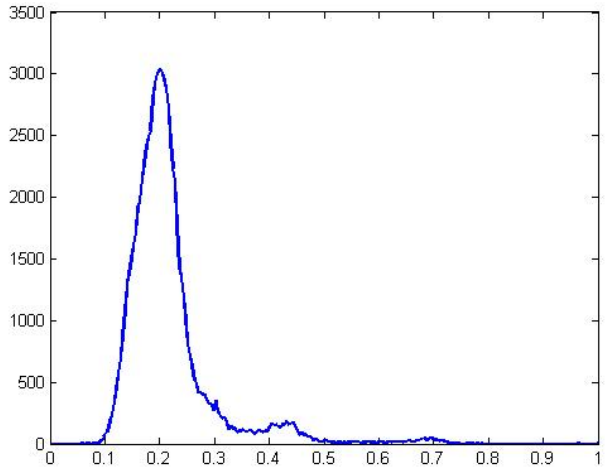

FIGURE 4.11 – Histogram of thermal image of figure 4.10.

method [4] is highly sensitive to noise which is observable from Figure 4.9. As time increases, the effect of noise is more visible, hence the algorithm cannot provide an acceptable result for time interval 0.6432 (s). Therefore, we do not use these two methods in the following experiments due to their drawbacks.

Figure 4.10 illustrates the results of detection approaches presented in [24], [23], [7] and [10] . As we can observe form this figure, the result of Hamadani's method [10] is more acceptable than the other approaches mainly because it is not an automatic method and it benefits from user intervention. The neighborhood valley-emphasis method ranks second. It uses neighborhood information to improve segmentation quality. The result of the valley-emphasis technique is similar to Otsu's method since the image histogram has a bimodal shape (figure 4.11) and valley-emphasis cannot provide a visible improvement (refer to chapter 2 for more details).

According to our experiments, Hamadani's method [10] provides more satisfactory results since it benefits from user intervention. Accordingly, we used it as a non-automatic approach which can be considered as a ground truth technique for our experiments. In addition, the neighborhood valley-emphasis algorithm can be used as an automatic detection method to

evaluate detection results.

Based on the previous segmentation results, we find out that combining TSR with PPT or PCT produces more satisfactory results yielding an acceptable detection for both segmentation methods [7; 10]. For a quantitative comparison, we computed the mean square error value (equation 4.1) between the original images of the samples and the segmented ones :

$$MSE = \frac{1}{M \times N} \sum_{j=1}^{N} \sum_{i=1}^{M} (I_{i,j} - S_{i,j})^2, \tag{4.1}$$

where, $I_{i,j}$ and $S_{i,j}$ are the i, j^{th} element of the original and segmented images, respectively. M and N are the height and width of the image, respectively.

Figure 4.12 illustrates more results for ACIER002, ALU016 and PLEXI006 specimens. It is obvious that the methods with lower values of MSE provide better detection of defects. Additionally, the low MSE values of the combination of TSR with PPT and PCT, our proposed approach, demonstrate the effectiveness of the detection for different kinds of material. More results are presented in figure 4.13 showing the detection of defects with different sizes. We can observe that small defects are best detected by PPT and TSR, while large defects are better detected by PCT and TSR. Overall, the results of PPT and TSR are superior since they detect more defects and estimate sizes closer to the ground-truth data. So, it is suggested to the user to select the appropriate approach based on the inspection application since a single technique does not work well on all types of defects.

This section presented an image processing method for detecting the defects of thermal images following a pulsed thermography test. Various experiments demonstrated significant improvements of defect detection. We used median filtering as the pre-processing denoising step to eliminate the reflection noise and increase the quality of thermal images. A combination of inspection techniques PPT, PCT and TSR is proposed to improve the distinction between defect and sound areas. Visual and quantitative comparisons support the effectiveness of the proposed approach in detecting small defects as well as larger ones.

4.4 Depth estimation

With the approaches presented in the previous section, we were able to detect the defects. Now, we need to estimate their depths. As mentioned in section 2.2 of chapter 2, several depth detection methods are proposed in the literature. We explained the advantages and disadvantages of these methods in section 3.3 of chapter 3 and we decided to use the Absolute peak slope time method [36] which is fast and accurate enough from needs. In this section, the experimental results are presented for detecting defect depth using a pulsed phase thermography method [20; 17; 3] which needs a reference point from a sound area and is really sensitive to

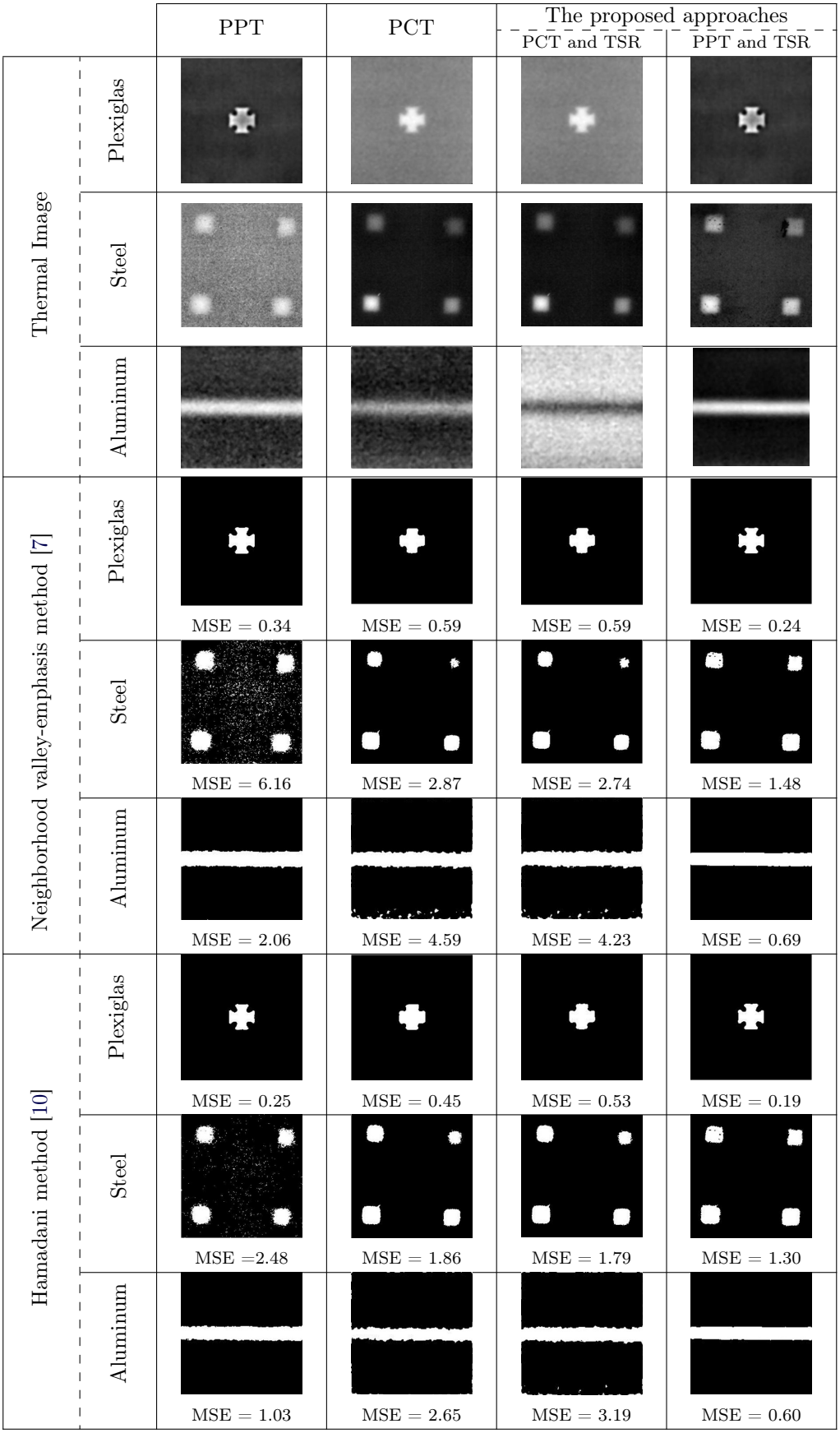

FIGURE 4.12 – Results obtained by the proposed approach in comparison with the ones obtained by [7; 10].

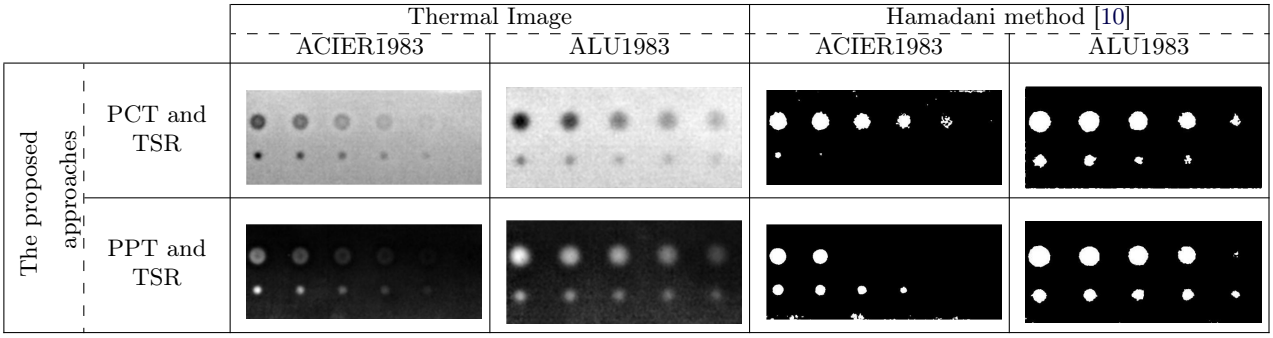

FIGURE 4.13 – Detecting different size of defects.

the sampling frequency. In addition, we also experimented with the Absolute peak slope time method. The results of both approaches are illustrated for high conductivity materials.

4.4.1 Pulsed phase thermography-based depth estimation

As mentioned in section 2.2 of chapter 2, pulsed phase thermography-based depth estimation transforms the thermogram from the time domain to the frequency domain using Discrete Fourier Transform (DFT). We applied this method on steel (ACIER002) and aluminum (ALU208) specimens (refer to Appendix A).

Steel

Figure 4.14 shows the phase profile of the steel specimen (ACIER002) which is obtained by applying the DFT on its corresponding thermogram with sampling rate 70 Hz in 7.14 seconds. The number of images that are recorded is equal to 500. According to the principle of DFT, only half of the frequency range is useful since the other half of the frequency range contains redundant information. This figure illustrates that depth of defects have a strong relationship with the blind frequency.

The blind frequency can be determined when the phase contrast equals zero. Figure 4.15 presents the phase contrast profile of this specimen. It is obvious that deeper defects are visible at lower frequency and shallow defects are detected at a higher frequency. Depth of defects can be calculated from equation $z = C_1\ \mu\ +\ C_2$ [14], in which thermal diffusion length μ is given as $\mu\ =\ (\frac{\alpha}{\pi f_b})^{1/2}$. C_1 and C_2 are constants such that $1.5 < C_1 < 2$. Therefore, the problem of depth estimation consists of finding the f_b of phase contrast.

Figure 4.16 presents the phase image corresponding to the blind frequencies of four defects of ACIER002. As we can observe, all defects are visible in the first thermograph, which is the phasegram at the blind frequency for the deepest defect. By increasing the frequency, deeper defects vanish one by one until only the shallowest defect can be detected on the last thermograph.

Actual depth(mm)	2.5	2	1.5	1
Blind frequency f_b (Hz)	1.35	2.43	10.53	17.1
Thermal diffusion length $\mu(\times 10^{-3})$	0.9951	0.7417	0.3563	0.2796

TABLE 4.1 – Defects depth and blind frequencies of defects for ACIER002.

With finding the blind frequency, f_b, we will calculate the thermal diffusion length, μ. The estimated blind frequencies and their corresponding thermal diffusion lengths are provided in table 4.1 for all the defects. Since we know the actual depths, we calculate two constants C_1 and C_2 in order to find the equation of the linear fit. We acquired $z = 1.97\mu + 0.000555$ for this specimen. Figure 4.17 shows the desired linear fit, blue line, and our obtained results, black squares.

Aluminum

We repeated the pulsed phase thermography method on aluminum plate (ALU208) with sampling rate 58 Hz in 10.29 seconds. The number of images that are recorded is equal to 600. Figures 4.18 and 4.19 present the phase and phase contrast profiles for six defects respectively with depth of 2 ,3 ,4 ,5 ,6 and 8 mm. The 5 and 8 mm defects did not provide enough contrast and their corresponding data produces a large error on the linear fit which is shown on figure 4.20 (b).

The estimation of the blind frequency f_b and the thermal diffusion length μ for 6 defects are presented in table 4.2. So as mentioned before, using the known depths we calculated two constants C_1 and C_2 and then we obtained $z = 1.55\mu$. Figure 4.20 (a) shows the phasegram

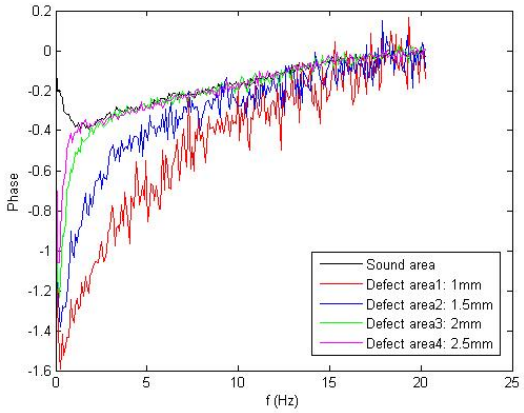

FIGURE 4.14 – Phase profile for ACIER002 with sampling rate 70 Hz and total number of 500 images in 7.14 seconds.

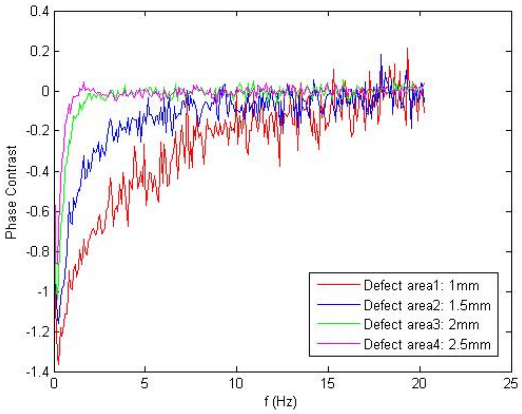

FIGURE 4.15 – Phase contrast profile for ACIER002 with sampling rate 70 Hz and total number of 500 images in 7.14 seconds.

Actual depth(mm)	8	6	5	4	3	2
Blind frequency f_b (Hz)	1.457	2.136	1.068	3.787	6.506	11.75
Thermal diffusion length $\mu(\times 10^{-3})$	4.2884	3.5418	5.0089	2.6600	2.0294	1.5101

TABLE 4.2 – Defects depth and blind frequencies of defects for ALU208 specimen.

at blind frequency 1.457 Hz.

The results illustrate that the depth estimation method based on pulsed phase thermography provides an acceptable result but it fails for the defects at frequencies higher than the blind frequency. However, the major disadvantage of this method is that it needs a reference point on a sound area in order to estimate the defects depth. For this reason it cannot be used as an automatic method.

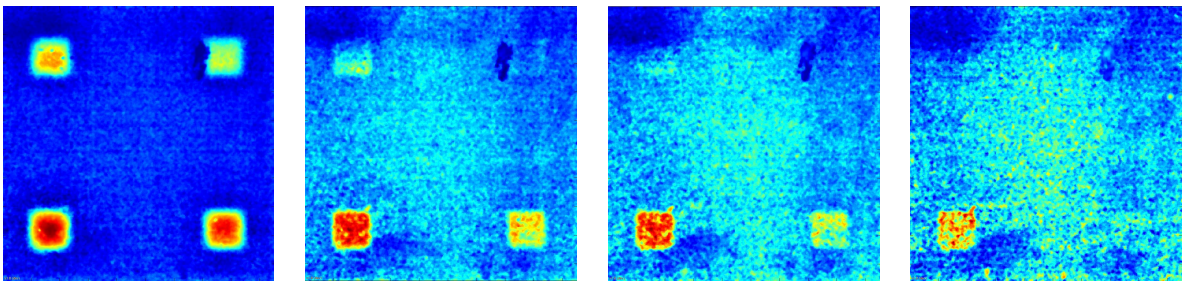

$f_b = 1.35\ Hz$ $f_b = 2.43\ Hz$ $f_b = 10.53\ Hz$ $f_b = 17.1\ Hz$

FIGURE 4.16 – Phasegrams for the blind frequencies corresponding to the 4 different depths of the defects.

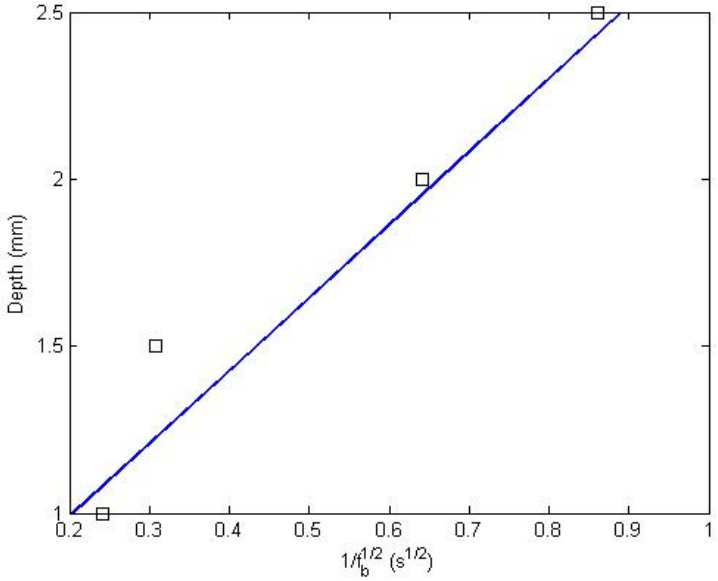

FIGURE 4.17 – Depth vs frequency linear fit for steel plate with sampling rate 70 Hz.

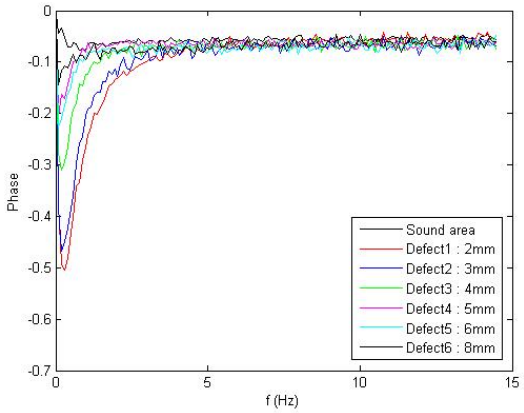

FIGURE 4.18 – Phase profile for ALU208 with sampling rate 58 Hz and total number of 600 images in 10.29 seconds.

4.4.2 Absolute peak slope time method results

As mentioned in section 3.3 of chapter 3, the Absolute peak slope time method uses a characteristic time to estimate the depth of defects which is obtained by finding the peak value of a function's first derivative ; this function is obtained by multiplying the temperature decay with the square root of the corresponding time. We tested this method on steel (ACIER002) and on aluminum (ALU208) specimens (refer to Appendix A). The results are presented in the following :

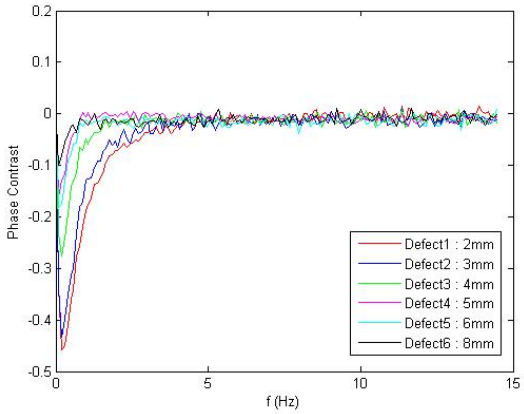

FIGURE 4.19 – Phase contrast profile for ALU208 with sampling rate 58 Hz and total number of 600 images in 10.29 seconds.

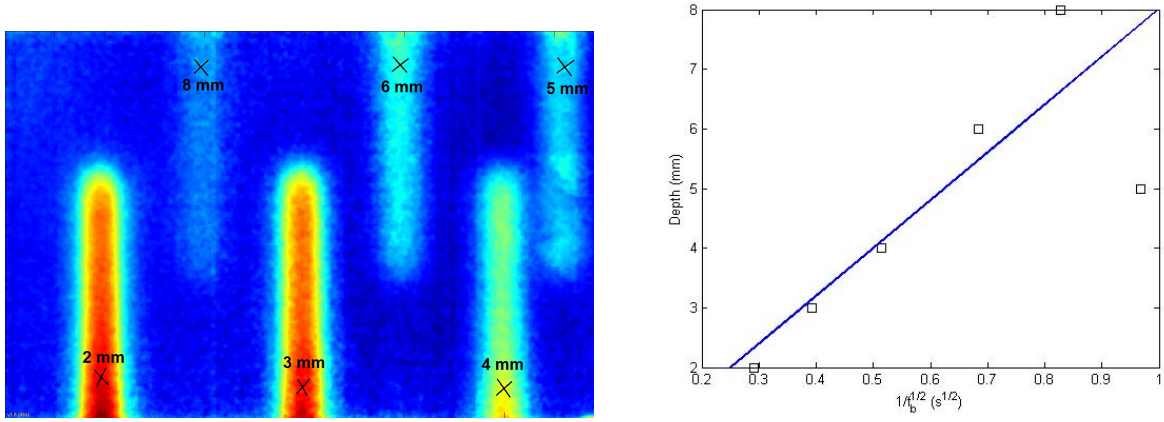

(a) (b)

FIGURE 4.20 – ALU208 with sampling rate 58 Hz (a) Defects' depths and location, and (b) Depth vs frequency linear fit.

Steel

The temperature decay of the specimen ACIER002 with four defects are presented in figure 4.21. For this reason, 500 images are recorded in 11.11 seconds with the sampling rate of 45 Hz .In order to find a characteristic time, the temperature curves on figure 4.21 are multiplied by the square root of the corresponding times, before this multiplication a median filter and the TSR method are applied on raw data. Figure 4.22 illustrates the new curves (called f functions).

As can be observed, the temperature curves do not have a peak slope. However, f curves have a segment of high curvature. Therefore, the first derivative of f curves is used to obtain the absolute peak slope times which is shown in figure 4.23. By obtaining the absolute peak slope

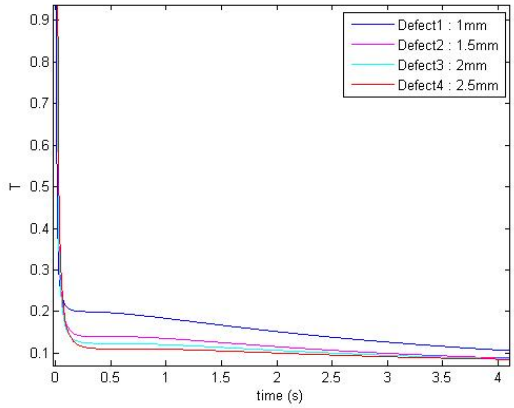

FIGURE 4.21 – Temperature curves of steel plate (ACIER002) with sampling rate 45 Hz and total number of 500 images in 11.11 seconds.

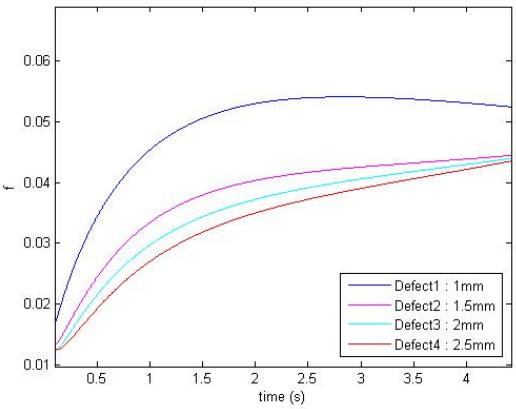

FIGURE 4.22 – The f curves of steel plate.

time, the defect depth can be calculated from $t_A PST = \frac{L^2}{2\alpha}$ (equation 3.13 in chapter3).

The absolute peak slope time versus the square defect depth is shown in figure 4.24.

Aluminum

We applied the Absolute peak slope time method on the specimen ALU208, 300 images are recorded in 3.4 seconds with the sampling rate of 88 Hz The processing steps are similar to the ones used for the steel plate of the previous experiment. The f curves for six defects are obtained from the temperature decay. The absolute peak slope times corresponding to the defects are identified from the first derivative of the f curves. Figures 4.25 and 4.26 shown the f curves and the f' curves of the aluminum specimen.

The results of the measured depths from equation (3.13) are provided in figure 4.27.

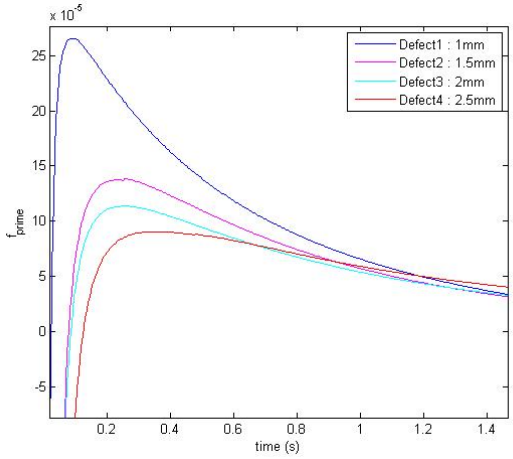

FIGURE 4.23 – The f' curves of steel plate.

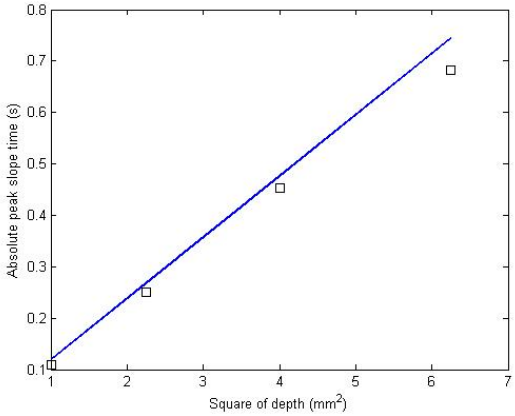

FIGURE 4.24 – Absolute peak slope time versus square depth of ACIER002.

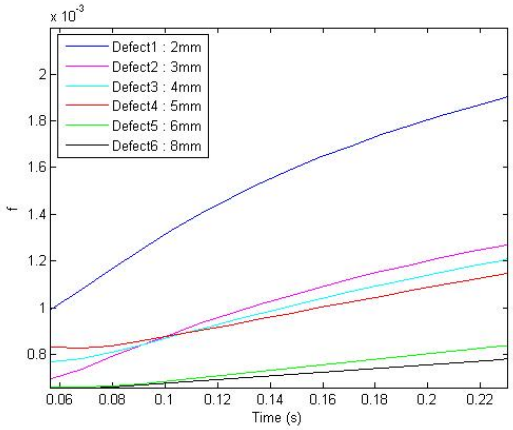

FIGURE 4.25 – The f curves of aluminum plate.

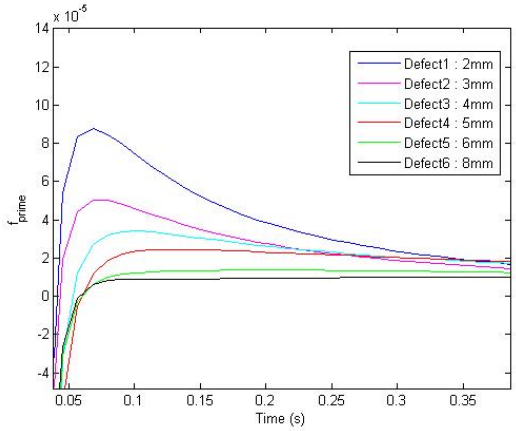

FIGURE 4.26 – The f' curves of aluminum plate.

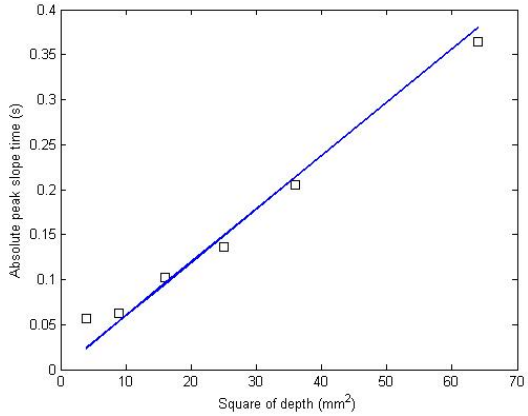

FIGURE 4.27 – The absolute peak slope time against square of the depth of the specimen ALU208.

According to figures 4.24 and 4.26, we can observe that the peak value decreases with an increasing depth of the defect. The accuracy of the algorithm is thus better with defects of larger sizes or with a better sampling rate and spatial resolution of the infrared camera. Therefore, for specimens for which the thermal diffusivity is known (it is the case for the materials of interest in this project : steel and aluminum), equation 3.13 can be used to estimate defect depth. However for specimens for which this parameter is unknown the linear relation between the characteristic time and square depth can be used to estimate defect depth [36].

Conclusion

Modern computer vision technology makes it possible to inspect the surface of objects. Non-Destructive Testing (NDT) is used to examine components of different materials without changing or destroying their structure. NDT is important to guarantee safe operation of system components as well as reducing direct and indirect costs. Therefore, it is essential to monitor the growth of defects such as cracks or corrosion, and estimate their location and depth as accurately as possible.

NDT is attractive for a large number of applications, such as civil engineering, petrochemical and power generation industries, and transportation productions.

Using Infrared Thermography (IRT) in NDT enables us to observe the temperature differences of thermograms acquired by infrared cameras and to detect the subsurface features. Our task in this project has focused on performing NDT for detecting subsurface defects and estimating their location and depth. Subsequently, this infrared information can be used to map undersurface defects on the 3D model of a specimen built with 3D sensors. We presented this application of mapping NDT on 3D models in a paper to appear in QIRT conference 2014 (Quantitative InfraRed Thermography).

- Soldan, S., Ouellet, D., Hedayati Vahid, P., Bendada, H., Laurendeau, D., "Mapping Non-Destructive Testing Data on the 3D Geometry of Objects with Complex Shapes", *12th International Conference on Quantitative InfraRed Thermography (QIRT), Bordeaux, France, 7-11 July 2014.*

In this thesis two challenges were addressed : localizing the defects and estimating their depth. We investigated different methods to solve these problems.

Because of imperfections in the acquisition system, such as limitations of the camera, the thermal images must be enhanced. In order to detect the defects better, the effect of noise must be reduced. In this way, the acquired infrared image sequences have been improved with preprocessing steps, such as denoising and enhancement. We submitted a poster in ISEM2013 (International Symposium on Applied Electromagnetics and Mechanics) to discuss the effect of denoising methods on infrared images (see reference below).

Defect enhancement techniques such as thermographic signal reconstruction (TSR), pulse

phase thermography (PPT), and principal component thermography (PCT) can be also used to improve the inspection process. In a paper to appear in QIRT conference 2014 (Quantitative InfraRed Thermography), we propose to use a combination of these powerful inspection approaches to enable the detection of both small and large defects, while compensate for the drawbacks of each method taken separately.

- Hedayati Vahid, P., Hesabi, S., Maldague, X., "The Effect of Pre-processing Techniques in Detecting Defects of Thermal Images", *16th International Symposium on Applied Electromagnetics and Mechanics (ISEM), Québec, PQ, Canada, July 31-Aug. 2, 2013.*
- Hedayati Vahid, P., Hesabi, S., Laurendeau, D., Maldague, X., "A Defect Detection Approach in Thermal Images", *12th International Conference on Quantitative InfraRed Thermography (QIRT), Bordeaux, France, 7-11 July 2014.*

Once thermal images have been preprocessed, all defects should be visible with good contrast and it is then possible to perform defect detection and depth estimation. Two types of defect detection methods were investigated : nondedicated and dedicated algorithms. Among the nondedicated algorithm, which refer to approaches which were not specifically designed for thermal images, the neighborhood valley-emphasis approach provides satisfactory results for our specimens. In the class of dedicated methods, which were specifically designed for thermal applications, Hamadani's method gives acceptable results. The comparative experiments of different defect detection methods were illustrated in the paper "A Defect Detection Approach in Thermal Images", QIRT 2014.

Once the location of defects is found, their depths must be estimated. We have investigated different thermography methods for depth estimation : Peak Temperature Contrast, Peak Temperature Contrast Slope, Pulsed Phased Thermography, Logarithmic Peak Second Derivative, Least-Squares Fitting, and Absolute Peak Slope Time methods. Two of these methods were tested experimentally : Pulsed Phased Thermography and Absolute Peak Slope Time methods. Based on our experimental results, we conclude that the absolute peak slope time is an appropriate automatic approach to estimate the depth of defects.

More research remains to be done on defect detection and depth estimation of non-planes specimens and objects with complex shapes. Moreover, increasing the accuracy of depth prediction as much as possible opens challenging area for the future work. Detecting different kind of defects, such as cracks and corrosion, as well as defects of small size needs more investigation.

Appendix A

Appendix A : Plate Specifications

In order to increase the absorption of the heat energy and signal-to-noise rate, the surface of the specimens is painted in black. The black painting increases the surface emissivity of the specimen and also decreases the reflections from the environment.

The variable z presents defects' depths which illustrates the distance between specimen surface and defect surface. In the following the schematic illustration of our test specimens are presented.

A.1 ACIER002

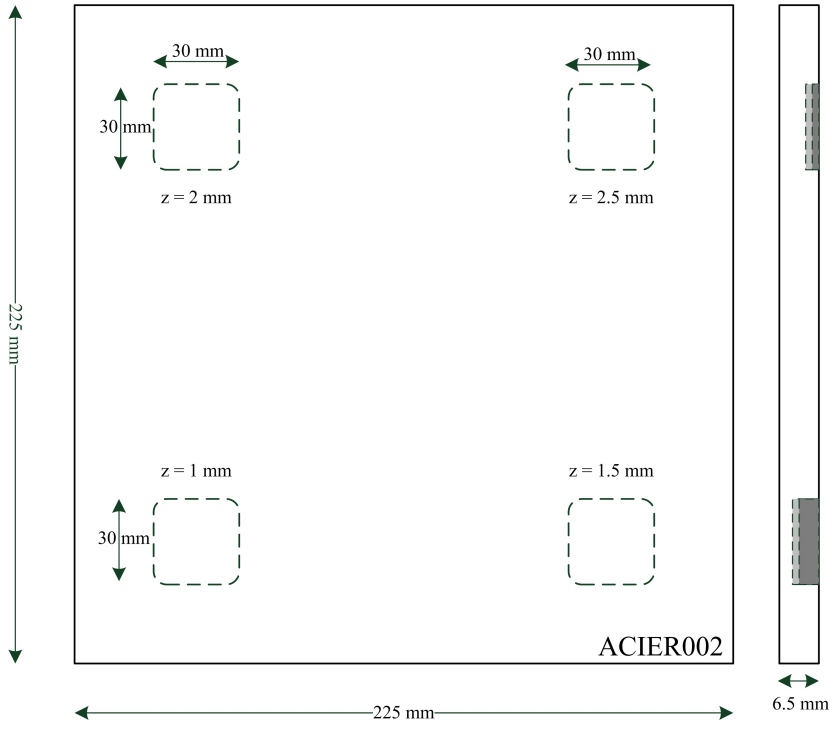

A.2 ACIER1983

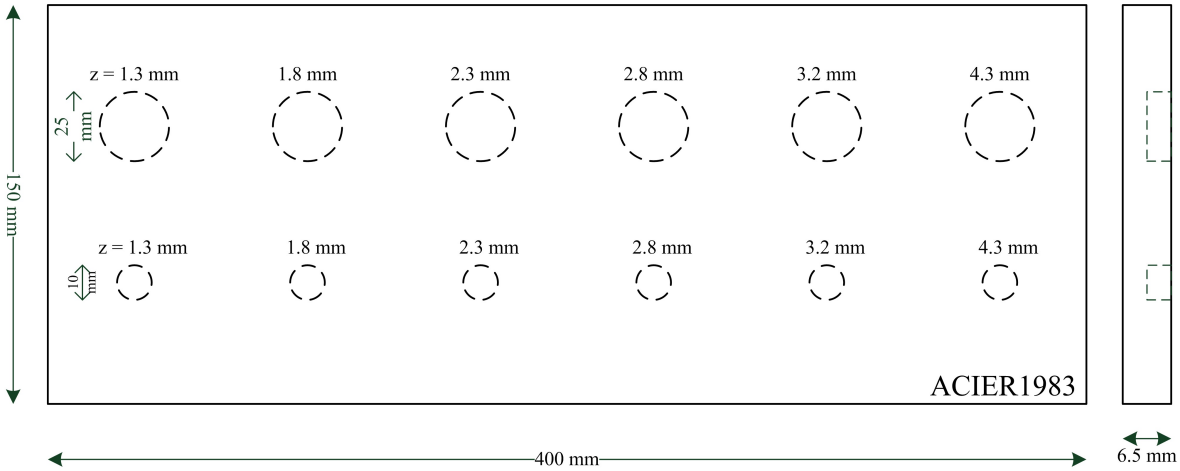

A.3 ALU016

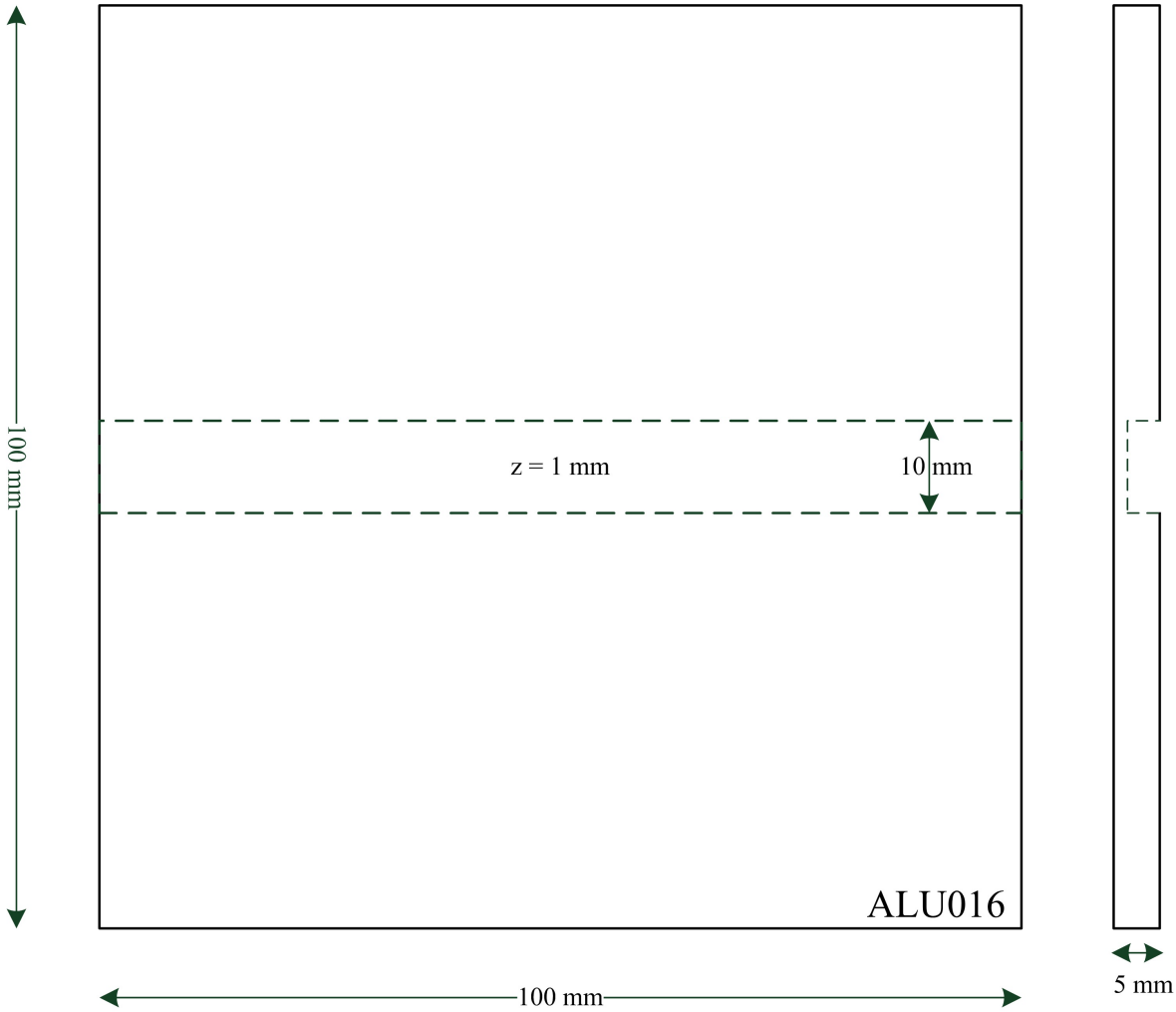

A.4 ALU1983

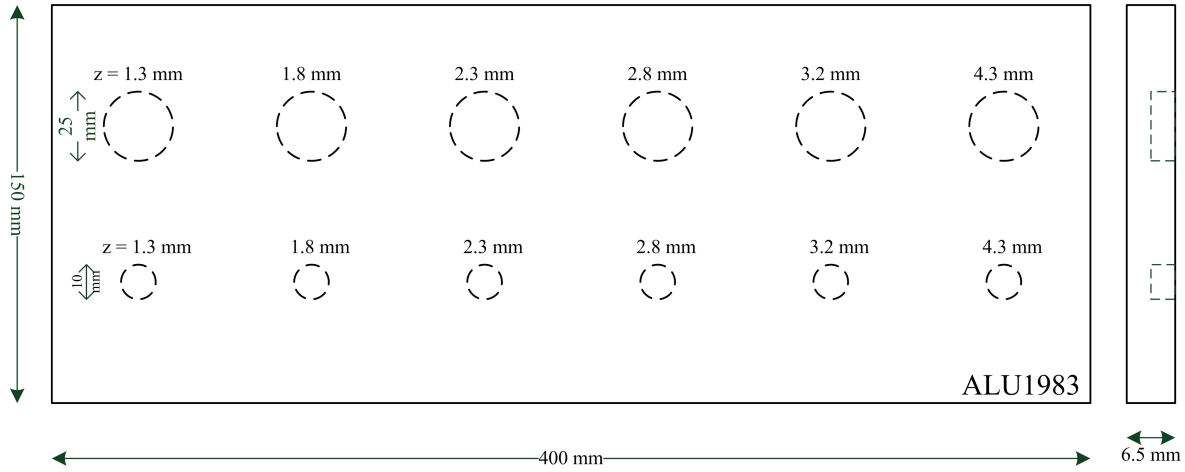

A.5 ALU208

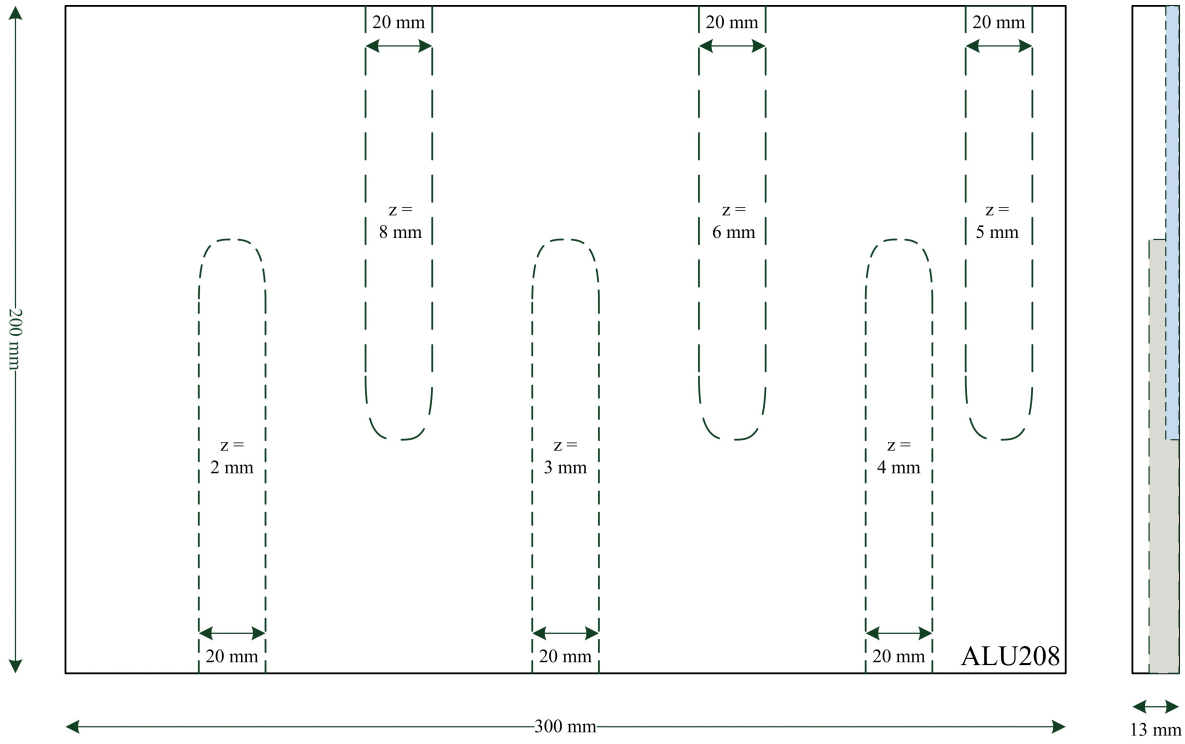

A.6 PLEXI006

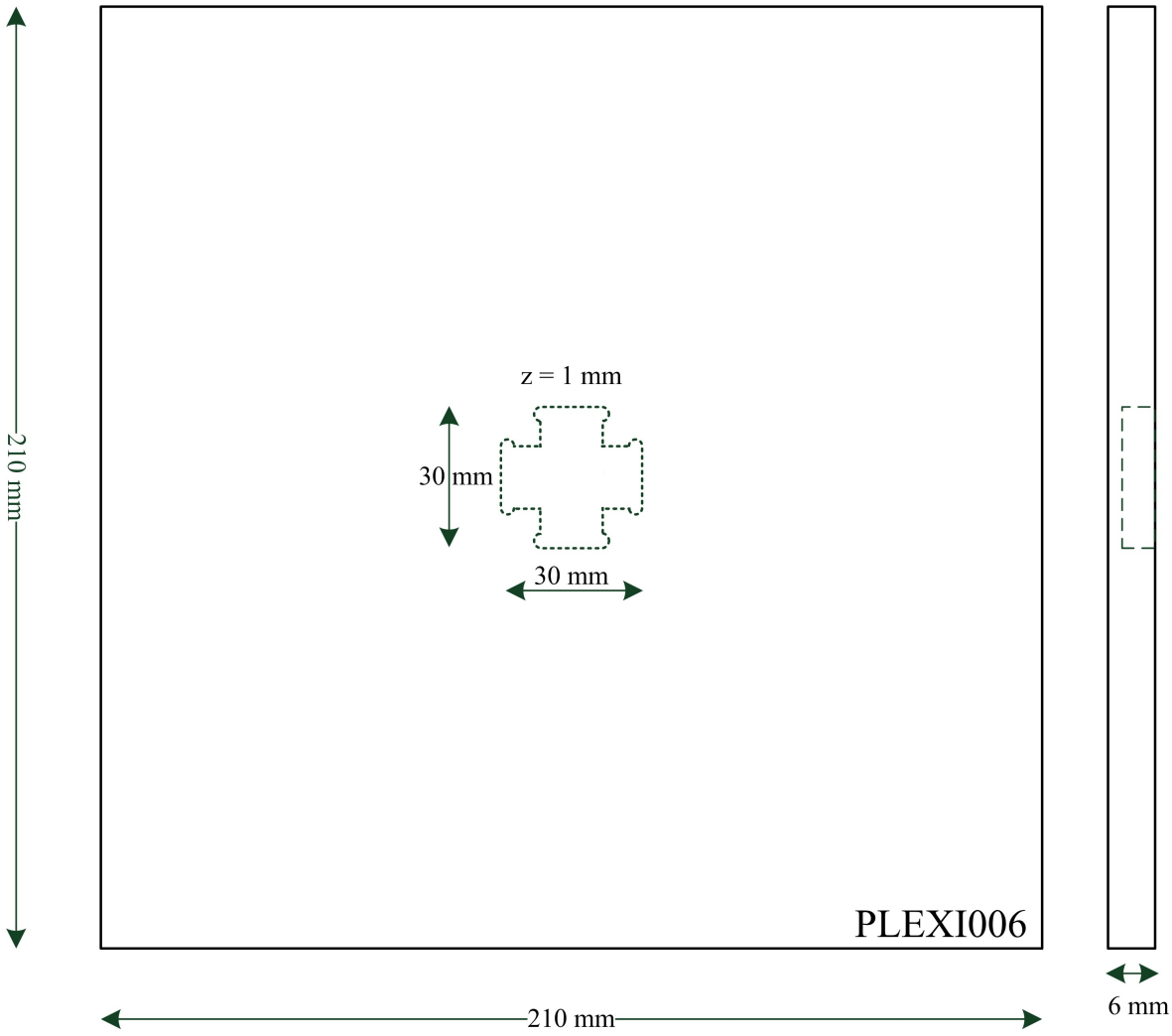

Appendix B

Appendix B : Phoenix camera quick start manual

Phoenix Camera System User's Guide

This manual is meant as a guideline for starting to work with the FLIR systems Phoenix camera with the RDAS A/D digitizer and the Rtool software kit.

SETUP

1. Switch on the camera using the switch on the right side of the digitizer. It will take the camera app. 10min to cool down before ready for use.

2. Log on the computer connected to the digitizer.

3. Open the file : c :\program files\rtools\rtools.reg (i.e.with UltraEdit)
   enter the line : "Windows Registry Editor Version 5.00" on top of the file.
   Execute the registry file to update the registry keys for PHOENIX.

4. **Start the PHOENIX software** :

   - If the "Communication Parameters" window pops up, set the "Comm Port" drop-down menu on "COMM 2" and click on the "Baud Rate Search" button. Notice that this window may have some delay.
     Now the test result should be "Digitizer". "Close" the window.

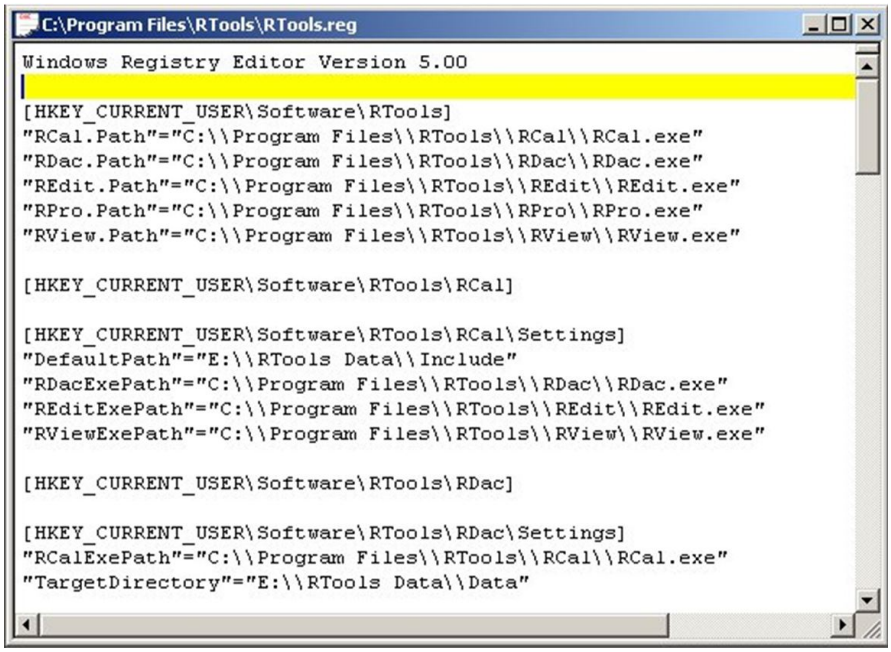

FIGURE B.1 – Editor rtools.reg

- Check "Auto Refresh Enable" for watching the camera cool down process. The final temperature is between 77K and 80 K.
  !!! do not change any further settings while cool down not yet finished!!!

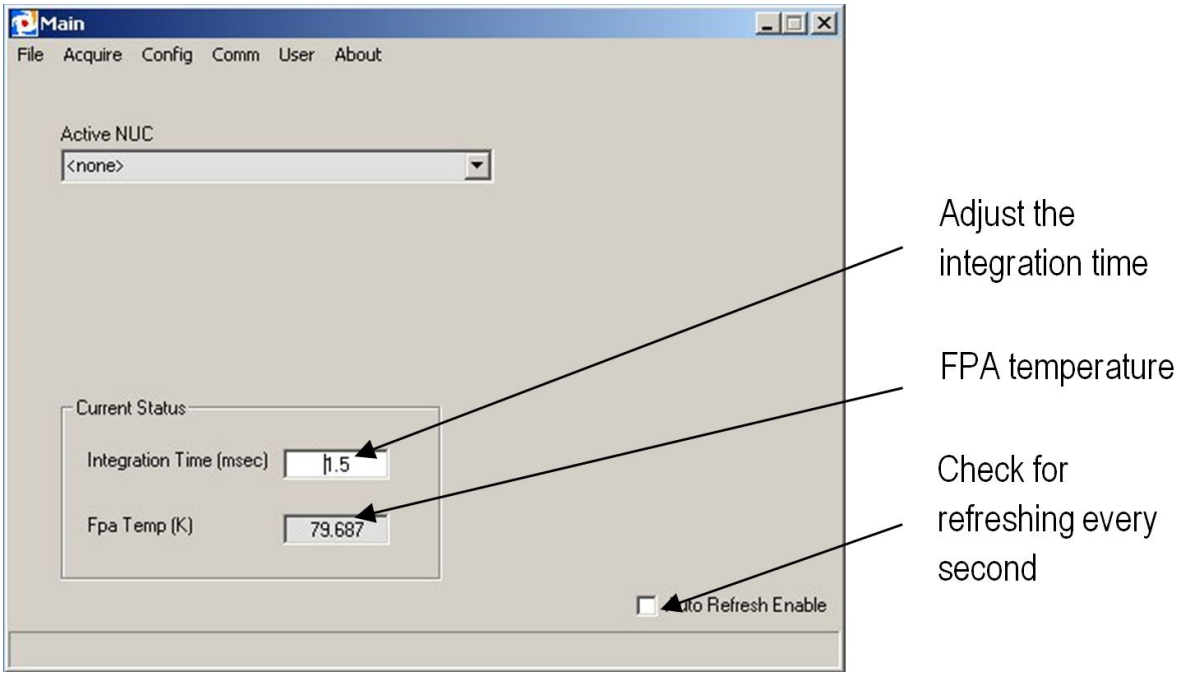

FIGURE B.2 – Phoenix main window

- Set a reasonable value in the “Integration Time” window after cool down.
  The default value is 1.5msec

– **Start the RDac software**

- On the first execution, it will ask you for some options :
  “Select a Include File” : the default file is D :\Rtools Data\Include\default.inc.
  “Select a Camera Controller Module” : D :\Program Files\RTools\RDac\Phoenix.exe.
  “Select a Configuration File” : C :\program files\RTools\RDac\Phoenix 640x512.dcf
  for full window mode.

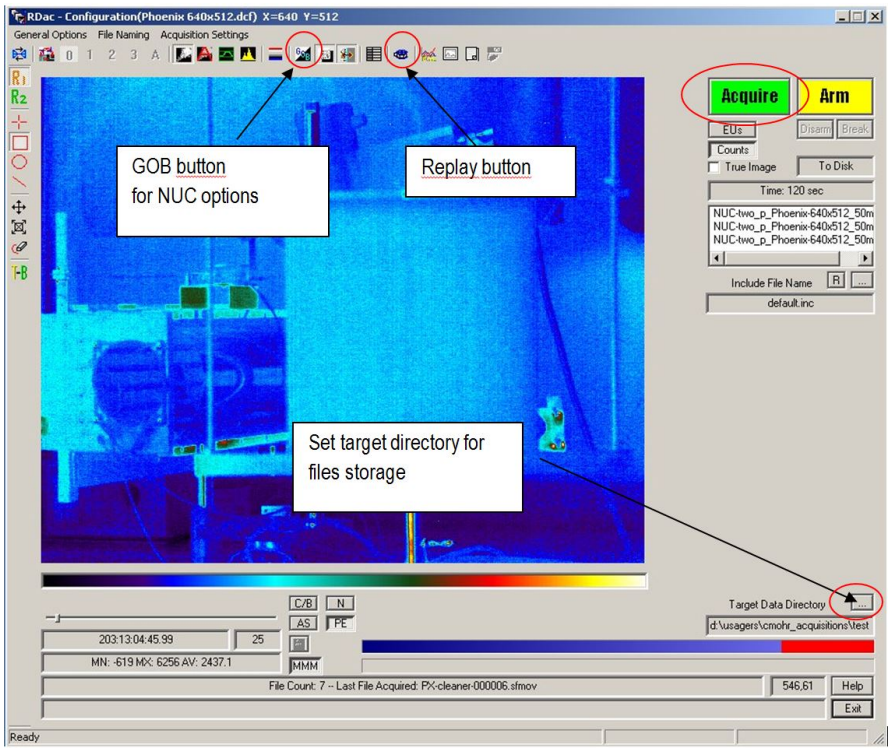

FIGURE B.3 – RDac main window

- Select an existing NUC or do a two point NUC
  to do this, click on the “GOB” button in the top middle of the RDac window.
  A dialog will appear with several options, see the full manual for all options.

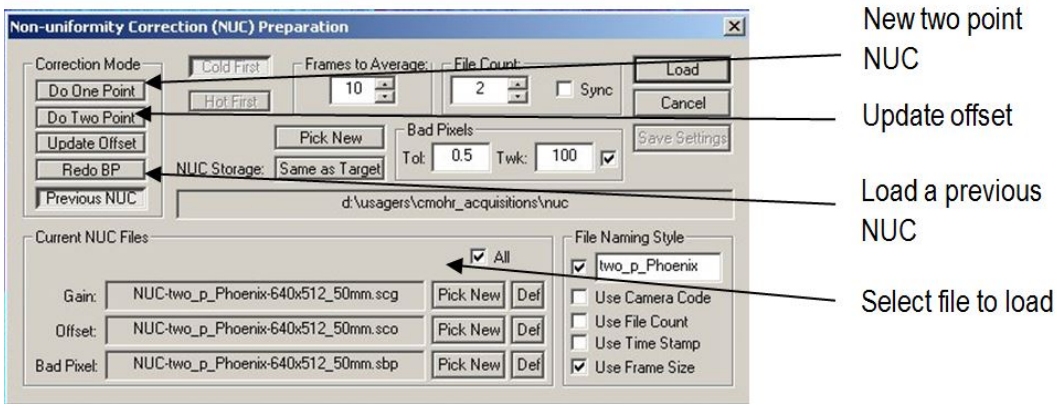

FIGURE B.4 – RDac NUC window

– Press the “Previous NUC ”-button to restore NUC files with “Pick new”
For files, check D :\Usagers\Phoenix ;
Press “Load” to load NUC settings.

– Press the “Update Offset” button to update the offset (recommended after any restart of the camera system), press “Next”, set up a uniform source, press “Acquire” and “Accept”.

– Press the “Do Two Point” button to get a new NUC (recommended after changing the lens or changing the integration time or NUC files older than app. 3 month)
Select a storage folder for the NUC Data with the NUC storage “Pick New” button.
Press “Next”, set up a cold uniform source, press “Acquire” and “Accept”,
set up hot source, press “Acquire” and “Accept” again.
The temperature difference between the two sources should be at least 30K.

– **Turn the lens to focus on your target :**

- Now there should be visible a clear image of the target without any stripes or bad pixels, if you experience any lens blur, correct the NUC offset after focusing the lens.

- To get color to your image, go to the “General Options”– >“Properties” menu in the RDac main window and choose a user palette to use.

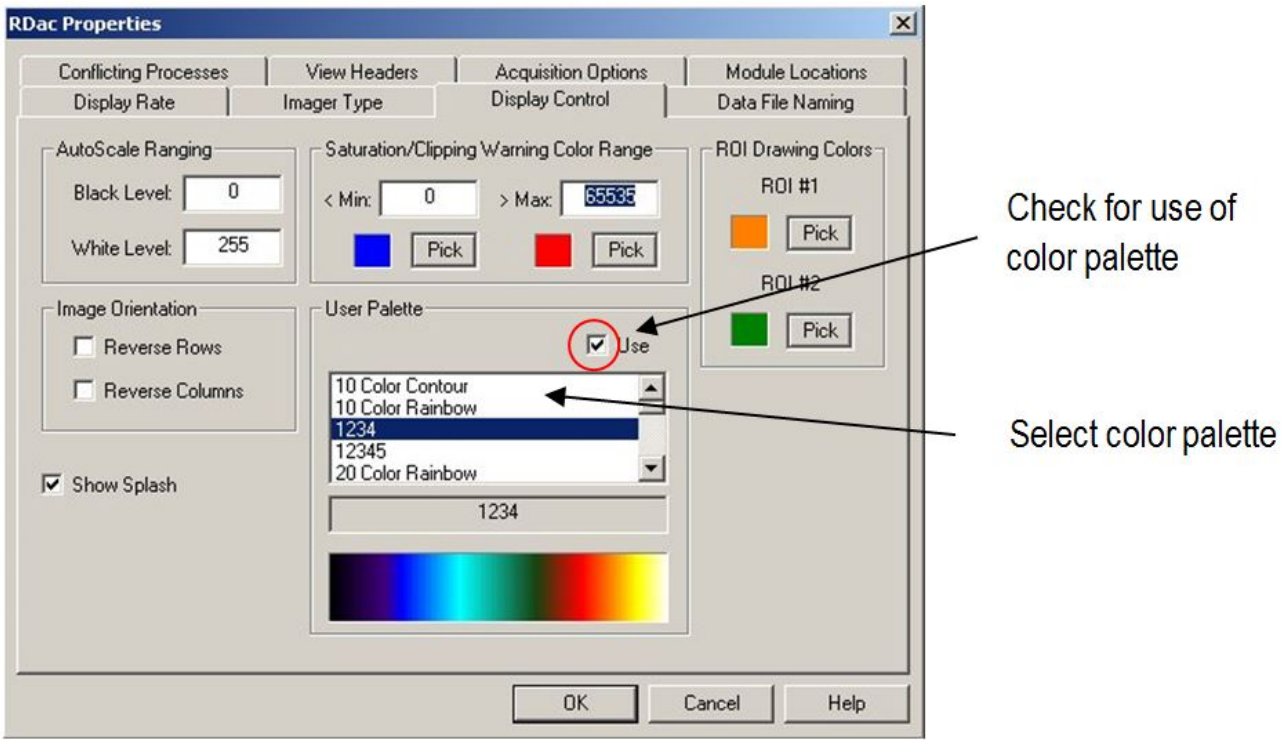

FIGURE B.5 – Rdac Properties window

ACQUISITION

1. Check the "File Naming" menu in the RDac main window for proper file naming.

2. Set the "Target Data Directory" in the lower right part of the RDac main window to the desired directory to store your acquisitions.

3. Check the "Acquisition Settings" menu in the RDac main window for proper settings. To work at maximum frame rate, check the "to Memory" radio button. With the "to Disk" option, the recorded frame rate is affected by the hard disk speed and the further writing options.

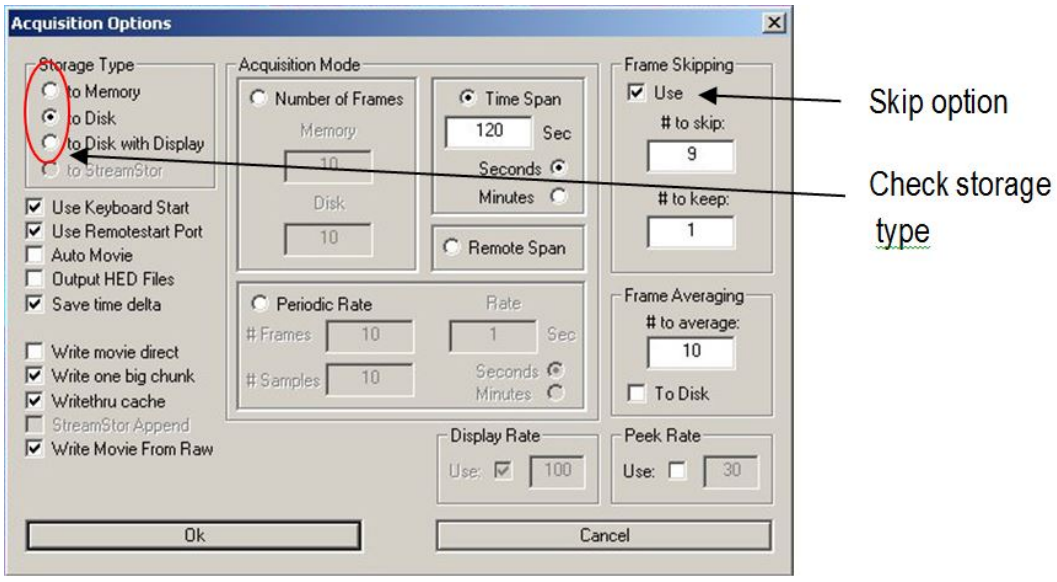

FIGURE B.6 – RDac Acquisition options window

4. Check http://www.indigosystems.com/CServices/phoenix_calc.html for a frame rate calculator to calculate the app. frame rate of the camera in free mode for your settings.
5. Set the number of frames or, with the "to Disk" option, alternatively the time span to record.
   Periodic rate means a bunch of "# Frames" images at full speed every "Rate" seconds; this is repeated for the number of samples specified.
6. Check the frame skipping option for getting a slower effective frame rate by skipping images.
7. With all settings done, press the "Acquire" button to start recording of images in a .sfmov or .sfimg file. Use the replay button in RDac or the RView software for seeing your results. See the RView manual for use of this software.

TROUBLESHOOTING

1. If the RDac main window is not responding, the camera or the frame grabber may be in a deadlock state.
   - Shut down the camera for more then 10 sec.
     Notice that there might be a short period for cool down necessary in order to get stable conditions.
   - Shut down the camera and then the computer. Restart the computer and then the camera.

– On the start-up of the PHOENIX software there might be an error message about a “factory.ini” file, but this doesn’t affect the function.
It disappears after saving your personal settings.

– It takes the Phoenix software about 10 sec. to communicate with the camera on the first start-up ; this is normal, since all options are being checked.

Bibliography

[1] Raymond J Archacki Jr, Harry I Ringermacher et William A Veronesi : Nondestructive testing : transient depth thermography, janvier 27 1998. US Patent 5,711,603.

[2] SG Burnay, TL Williams et CH Jones : *Applications of thermal imaging*. A. Hilger in Bristol, Philadelphia, 1988.

[3] Clemente Ibarra Castanedo : *Quantitative subsurface defect evaluation by pulsed phase thermography : depth retrieval with the phase*. Thèse de doctorat, Université Laval, 2005.

[4] Tony F Chan et Luminita A Vese : Active contours without edges. *Image processing, IEEE transactions on*, 10(2):266–277, 2001.

[5] Krzysztof Chrzanowski : Review of infrared systems. Rapport technique AW321/2005, Inframet, Kwirynow, Poland, 2005.

[6] C Deemer, JG Sun, WA Ellingson, S Short et IL60115 DeKalb : Front-flash thermal imaging characterization of continuous fiber ceramic composites. *1999.*, 1999.

[7] Jiu-Lun Fan et Bo Lei : A modified valley-emphasis method for automatic thresholding. *Pattern Recognition Letters*, 33(6):703–708, 2012.

[8] Lawrence D Favro, Xiaoyan Han, Pao-Kuang Kuo et Robert L Thomas : Imaging the early time behavior of reflected thermal wave pulses. *In SPIE's 1995 Symposium on OE/Aerospace Sensing and Dual Use Photonics*, pages 162–166. International Society for Optics and Photonics, 1995.

[9] LD Favro, HJ Jin, YX Wang, T Ahmed, X Wang, PK Kuo et RL Thomas : Ir thermal wave tomographic studies of structural composites. *In Review of Progress in Quantitative Nondestructive Evaluation*, pages 447–451. Springer, 1992.

[10] Naser A Hamadani : Automatic target cueing in ir imagery. *Air Force Interim Report*, 1, 1981.

[11] Xiaoyan Han, LD Favro, PK Kuo et RL Thomas : Early-time pulse-echo thermal wave imaging. *In Review of progress in quantitative nondestructive evaluation*, pages 519–524. Springer, 1996.

[12] Rudi Heriansyah et SAR Abu-Bakar : Defect detection in thermal image for nondestructive evaluation of petrochemical equipments. *NDT & E International*, 42(8):729–740, 2009.

[13] Clemente Ibarra-Castanedo, Nicolas P Avdelidis, Marc Grenier, Xavier Maldague et Abdelhakim Bendada : Active thermography signal processing techniques for defect detection and characterization on composite materials. *In SPIE Defense, Security, and Sensing*, pages 76610O–76610O. International Society for Optics and Photonics, 2010.

[14] Clemente Ibarra-Castanedo, Abdelhakim Bendada et Xavier Maldague : Thermographic image processing for ndt. *In IV Conferencia Panamericana de END*, 2007.

[15] Clemente Ibarra-Castanedo, Daniel Gonzalez, Matthieu Klein, Mariacristina Pilla, Steve Vallerand et Xavier Maldague : Infrared image processing and data analysis. *Infrared physics & technology*, 46(1):75–83, 2004.

[16] Clemente Ibarra-Castanedo et Xavier Maldague : Pulsed phase thermography reviewed. *Quantitative Infrared Thermography Journal*, 1(1):47–70, 2004.

[17] Clemente Ibarra-Castanedo et Xavier P Maldague : Defect depth retrieval from pulsed phase thermographic data on plexiglas and aluminum samples. *In Defense and Security*, pages 348–356. International Society for Optics and Photonics, 2004.

[18] Wilhelm Isoz, Thomas Svensson et Ingmar Renhorn : Nonuniformity correction of infrared focal plane arrays. *In Defense and Security*, pages 949–960. International Society for Optics and Photonics, 2005.

[19] Xavier Maldague : Theory and practice of infrared technology for nondestructive testing. 2001.

[20] Xavier Maldague et Sergio Marinetti : Pulse phase infrared thermography. *Journal of Applied Physics*, 79(5):2694–2698, 1996.

[21] Xavier PV Maldague : *Nondestructive evaluation of materials by infrared thermography*. Springer, 1993.

[22] Xavier PV Maldague et PO Moore : Nondestructive testing handbook, vol. 3 : Infrared and thermal testing. *American Society for Nondestructive Testing*, 2001.

[23] Hui-Fuang Ng : Automatic thresholding for defect detection. *Pattern recognition letters*, 27(14):1644–1649, 2006.

[24] Nobuyuki Otsu : A threshold selection method from gray-level histograms. *IEEE Transactions on Systems Man Cybernet SMC*, 1(9):62–66, 1979.

[25] WJ Parker, RJ Jenkins, CP Bulter et GL Abbott : Flash method of determining thermal diffusivity, heat capacity, and thermal conductivity. *Journal of Applied Physics*, 32:1679–1684, 1961.

[26] Rohit Parvataneni : *Principal component thermography for steady thermal perturbation scenarios*. Thèse de doctorat, Clemson University, 2009.

[27] Nik Rajic : Principal component thermography for flaw contrast enhancement and flaw depth characterisation in composite structures. *Composite Structures*, 58(4):521–528, 2002.

[28] A Rogalski : Infrared detectors, electrocomponent science monographs. *Gordon and Breach Science Publishers, Amsterdam*, 2000.

[29] A Rogalski : History of infrared detectors. *Opto-Electronics Review*, 20(3):279–308, 2012.

[30] A Rogalski et K Chrzanowski : Infrared devices and techniques. *Optoelectronics Review*, (2):111–136, 2002.

[31] Antonio Rogalski : *Infrared detectors*. CRC Press, 2010.

[32] Steven M Shepard : Advances in pulsed thermography. *In Aerospace/Defense Sensing, Simulation, and Controls*, pages 511–515. International Society for Optics and Photonics, 2001.

[33] Steven M Shepard, James R Lhota, Bruce A Rubadeux, David Wang et Tasdiq Ahmed : Reconstruction and enhancement of active thermographic image sequences. *Optical Engineering*, 42(5):1337–1342, 2003.

[34] JG Sun : Analysis of pulsed thermography methods for defect depth prediction. *Journal of Heat Transfer*, 128(4):329–338, 2006.

[35] V Vavilov, T Ahmed, J Jin, R.L. Thomas et L.D. Favro : Experimental thermal tomography of solids by using the flash one-side heating. *Sov. J. NDT*, 12, 1990.

[36] Zhi Zeng, Jing Zhou, Ning Tao, Lichun Feng et Cunlin Zhang : Absolute peak slope time based thickness measurement using pulsed thermography. *Infrared Physics & Technology*, 55(2):200–204, 2012.